NASA Contractor Report 4051

Some Features of Surface Pressure Fluctuations in Turbulent Boundary Layers With Zero and Favorable Pressure Gradients

B. E. McGrath and R. L. Simpson
Virginia Polytechnic Institute and State University
Blacksburg, Virginia

Prepared for
Langley Research Center
under Grant NAG1-446

National Aeronautics
and Space Administration

**Scientific and Technical
Information Branch**

1987

NASA Contractor Report 4051

Some Features of Surface Pressure Fluctuations in Turbulent Boundary Layers With Zero and Favorable Pressure Gradients

B. E. McGrath and R. L. Simpson

GRANT NAG1-446
MARCH 1987

NASA

SUMMARY

Various researchers are interested in the structure of the surface pressure fluctuations for the development and use of noise prediction techniques for helicopter and turbomachinery rotors. This study, conducted in the Virginia Tech low speed boundary layer wind tunnel, covered the effects of zero and favorable streamwise pressure gradient flows on the surface pressure fluctuation spectra, coherence and convective wave speeds in turbulent boundary layers for momentum Reynolds numbers from 3000 to 18,800. The acceleration parameter, K is near 2×10^{-7} for the favorable pressure gradient flow. Small pinhole condenser microphones were used to obtain the surface pressure fluctuation data for all test cases. The longitudinal and lateral coherence functions and the convective wave speeds were obtained for both streamwise pressure gradient flows.

The results presented are for the surface pressure fluctuation spectra nondimensionalized by different groupings of the outer and inner boundary layer variables. The grouping using the outer variables, U_e, τ_w and δ_1 collapse the spectra for the low to middle range of frequencies for most test cases. The grouping using the inner variables, U_τ and ν, collapse the spectra for the middle to high range of frequencies for all test cases. The

value of p'/τ_w was near 3.8 and 2.8 for the smallest values of d^+ in the zero and favorable pressure gradient flows, respectively.

The spectral data was corrected using the correction developed by G.M. Corcos, but the pinhole correction developed by Bull and Thomas was not used in the data reduction process. However, some discussion is included on the effects of the pinhole correction for the results of this study.

The coherence exhibits a decay that is not exponential in some cases, but the Corcos similarity parameters $\omega\Delta x/U_c$ and $\omega\Delta z/U_c$ collapse the data for all test cases. The ratio of U_c/U_e increases with $\omega\delta_1/U_e$ up to $\omega\delta_1/U_e$ on the order of unity, where U_c/U_e becomes nearly constant. This was observed in the present results for both streamwise pressure gradient flows.

The experimental results presented show good agreement with previous research.

TABLE OF CONTENTS

LIST OF ILLUSTRATIONS

LIST OF TABLES

LIST OF SYMBOLS

c ..... speed of sound, m/s

C_f ..... skin friction coefficient

d ..... diameter of microphone, m

d^+ ..... nondimensional diameter, dU_τ/ν

G_{xx} ..... the power spectrum at position x

G_{zz} ..... the power spectrum at position z

G_{zx} ..... the cross power spectrum between position z and position x

H ..... shape factor, δ_1/θ

I_n ..... normalized quadrature of the cross spectrum for frequency n

k ..... wavenumber, ω/U_c

K ..... acceleration parameter for nonzero streamwise pressure gradient flows, $(\nu/U_e^2)(dU_e/dx)$

K_1, K_3 ..... exponential decay constants for longitudinal and lateral directions

n ..... frequency, Hz

P ..... instantaneous pressure, Pa

P_o, p ..... mean and fluctuating wall pressures, Pa

p' ..... rms wall pressure fluctuation, Pa

q_e ..... local free stream dynamic pressure, Pa

r ..... transducer radius, m

R_n ..... normalized co-spectrum of the cross spectrum for frequency n

Re ..... Reynolds number

Re_{δ_1} ..... displacement thickness Reynolds number

Re_θ ..... momentum thickness Reynolds number

U_c ..... convective wave speed, m/s

U_e ..... local free stream velocity, m/s

U_i ..... mean velocities in i directions, m/s

u_i ..... fluctuating velocities in the i direction, m/s

U_τ ..... friction velocity, m/s

$-\overline{uv}$ ..... kinematic Reynolds shear stress, $(m/s)^2$

V_i ..... instantaneous velocity in the i directions, m/s

V ..... volume, m^3

x,y,z ..... streamwise, normal to wall, spanwise positions, m

$\Delta x, \Delta y, \Delta z$ ..... spatial separations in the respective directions, m

GREEK SYMBOLS

α ..... ratio of streamwise length scale to length scales in other directions

γ^2 ..... coherence function, $\gamma^2 = |G_{zx}|^2 / G_{xx} G_{zz}$

γ ..... square root of the coherence function

δ ..... boundary layer thickness

δ_1 ..... boundary layer displacement thickness

θ ..... boundary layer momentum thickness

μ ..... coefficient of viscosity, kg/m.sec

ν ..... kinematic viscosity, m^2/sec

ρ ..... density, kg/m^3

ϕ ..... phase angle, $\omega\Delta x/U_c$ and $\omega\Delta z/U_c$

$\Phi(\omega)$ ..... power spectrum of fluctuating pressure as a function of ω, where $\overline{p^2}=\int_{-\infty}^{+\infty} \Phi(\omega)d\omega$

$\Phi(k)$ ..... power spectrum of fluctuating pressure as a function of k, where $\overline{p^2}=\int_{-\infty}^{+\infty} \Phi(k)dk$

ω ..... radial frequency, $2\pi n$ radians

SUBSCRIPTS

a ..... acoustic contribution to fluctuating pressure

t ..... turbulent contribution to fluctuating pressure

n ..... frequency, Hz

1,2 ..... microphone unit or position number

1.0 INTRODUCTION

The study of surface pressure fluctuations in a turbulent boundary layer flow has been of interest to researchers for many years. Surface pressure fluctuations that occur in turbulent flow are noise sources. Helicopter and turbomachinery rotors, aircraft and ships are examples of practical devices whose surface turbulent boundary layers generate pressure fluctuations that contribute to the generation of noise. Designers and researchers are most interested in methods for predicting and reducing flow noise due to pressure fluctuations. Brooks and Schlinker (1982) give a review on the recent progress in rotor noise research.

The problem faced by many researchers and designers is the lack of detailed information on the relationship between the turbulent flow field and the resulting pressure fluctuations. A recent effort by Brooks and Hodgson (1981) shows the development of a noise prediction method for turbulent boundary layer flow. Brooks and Hodgson used a NACA 0012 airfoil in their experimental study to relate the turbulent flow field to the surface pressure spectra, cross spectra and convective wave speeds. Thus, the prediction method uses a statistical model of the turbulent boundary layer pressure field and empirical relations of the convective wave speeds. Using this information the cross

spectra of the flow field are predicted and the resultant rms pressure fluctuation can be calculated, therefore giving an overall estimate of the resultant noise. These recent studies have given some direction to researchers and designers interested in the study of flow noise due to pressure fluctuations.

The experiments performed in Virginia Tech's boundary layer wind tunnel are an effort to obtain detailed velocity and surface pressure experimental data for two zero and one favorable streamwise pressure gradient turbulent boundary layers. Some previous research on these types of flow has been conducted by Bradshaw (1967), Willmarth (1975), Schloemer (1967), Blake (1970), Bull (1967) and others that are included in the list of references.

The wind tunnel and the test flows are discussed in section 3. A flat plate 8 meters in length and 0.9 meters in width was used in the present experiments. A cross section of the wind tunnel test section is shown in Figure 1. Zero pressure gradient flows between Re_θ of 3300 to 18,800 were examined. The favorable pressure gradient flow permitted examination of the streamwise flow properties between Re_θ of 3000 to 9000. The favorable pressure gradient flow work is an effort to provide information where little has been previously provided. The fluid dynamic properties of these flows were obtained using a hot-wire anemometer. The surface pressure spectra and convective wave speeds were

measured using miniature pinhole condenser microphones mounted flush with the surface as discussed in section 4.1. Two sets of microphones were located at each x-location and separated in the spanwise direction by approximately one-third of a meter. Because streamwise acoustical and unsteady waves are the same at both spanwise locations at any instant, the spectrum of the difference of these time-varying signals is related only to the turbulent surface pressure spectrum, as discussed in section 4.2 below. This setup permitted measurement of turbulence generated pressure spectral data in a tunnel that is not acoustically quiet. This method of data acquisition provides an advantage over previous work because no additional work was needed to quiet the flow to measure the pressure fluctuations due only to the flow field fluctuations.

The results that are presented in section 5 are the power spectra of the surface pressure fluctuations, rms pressure values, some flow field properties, convective wave speeds and the square root of the coherence in the streamwise and spanwise directions. The results of previous work are compared in section 6 to the results obtained in this study. Some development of the relationships among the flow field, pressure spectra, coherence spectral magnitude and convective wave speeds is also included.

2.0 THEORETICAL FORMULATION AND PREVIOUS WORK

2.1 FORMULATION

Consider an incompressible turbulent flow, which is the case for the present experiments. The Navier-Stokes equations define the relationship between the fluctuating pressures and fluctuating velocities. In vector form the equation is written as follows.

$$\partial\overline{V}/\partial t+\overline{V}\cdot\nabla\overline{V}+\nabla P/\rho = \nu\nabla^2\overline{V} \qquad (1)$$

$\overline{V}$ is the velocity vector, ρ is the density, ν is the kinematic viscosity and P is the pressure. For incompressible flow ρ is constant and we also assume that ν is constant. Taking the divergence of each term in the equation above and making use of the continuity equation

$$\nabla\cdot\overline{V} = 0 \qquad (2)$$

we obtain

$$\partial^2 P/\partial x_i^2 = -\rho q \qquad (3)$$

where q is given by the following

$$q = \partial^2 V_i V_j / \partial x_i \partial x_j . \qquad (4)$$

For turbulent flow we can define the velocity vector as

$$V_i(\overline{x},t) = U_i(\overline{x}) + u_i(\overline{x},t) \qquad (5)$$

and the pressure as

$$P(\overline{x},t) = P_o(\overline{x}) + p(\overline{x},t) . \qquad (6)$$

Now placing these terms into equation (3) and rearranging we obtain Poisson's differential equations for the pressure fluctuations,

$$\partial^2 p / \partial x_i^2 = -2\rho (\partial U_i / \partial x_j)(\partial u_j / \partial x_i) - \rho \partial^2 (u_i u_j - \overline{u_i u_j}) / \partial x_i \partial x_j . \qquad (7)$$

U_i and u_i are the mean and fluctuating velocities in the x_i direction. The first term of the RHS of this equation represents the turbulence-mean shear interaction and the second term represents the turbulence-turbulence interaction. To obtain a solution to equation (7) for surface pressure fluctuations, we integrate the equation for a wall-bounded flow. Neglecting the contribution of the

surface integrals, then the fluctuating pressure at some point $\overline{X}$ on the wall is given by

$$p(\overline{x}) = \rho/2\pi \int_{Y>0} q(\overline{x}_s) dV(\overline{x}_s)/|\overline{x}-\overline{x}_s| \qquad (8)$$

where the volume integration is at all positions $\overline{X}_s$ over the entire half-space containing the flow. This equation shows that the surface pressure fluctuations are produced from sources in a large region of the flow, but contributions from various sources drop off rapidly with increasing distance from the point $\overline{X}$ under consideration.

Several attempts have been made to obtain the surface pressure field theoretically from equation (8), but Willmarth (1975) has pointed out that such efforts suffer from the lack of accurate information about the fluctuating velocity field in the turbulent boundary layer flow. Thus, such efforts need confirmation by experimental data and this experimental investigation is an effort to provide data to bridge that gap. Some earlier research that deals with the theoretical and experimental aspects of surface pressure fluctuations are discussed in the following sections.

2.2 CALCULATIONS OF PANTON AND LINEBARGER

Panton and Linebarger (1974) developed a numerical solution for the wall pressure spectra in two-dimensional

turbulent boundary layers. Their solution were for zero and adverse pressure gradient equilibrium boundary layers. The results seem to describe the essential features observed in experiments. They used Coles' laws of the wall and wake for the mean velocity profiles. A scale-anisotropic model of the spatial correlations of v was used together with the assumption that v is proportional to $\sqrt{-\overline{uv}}$. Only the turbulence-mean shear interaction term in equation (7) was modeled since the turbulence-turbulence interaction contributes a small portion to the mean-square value in such flows.

Their spectral results show larger contributions at higher Re for $k\delta<20$, than for some of the previous experimental studies. Contributions at these low frequencies are due to the outer region velocity and turbulence structure and depend on the pressure gradient. An overlap region between the low frequency outer-flow-dominated part and the high frequency near-wall viscous-sublayer-dominated part of the spectrum varies with k^{-1} as observed by Bradshaw (1967). Their calculation results are approximated by

$$kF(k)/\tau_w^2 \approx 1.73\alpha^{0.9}, \quad \text{for } k\nu/U_\tau<0.06. \qquad (9)$$

Here α is the ratio of the streamwise length scale to length scales in other directions, which influences the spatial

correlation of v. For higher frequencies, the spectral variation is given by

$$kF(k)/\tau_w^2 \approx 0.0173(k\nu/U_\tau)^{-2}, \quad \text{for } k\nu/U_\tau \geq 0.1. \qquad (10)$$

Both of these equations are independent of Re and are scaled on the wall shear stress.

Because the low frequency part of the spectrum is Re dependent, the mean square pressure fluctuation increases with Re. The equation

$$p'^2/\tau_w^2 = 0.52\alpha^{0.9}(\ln|U_\tau\delta/\nu| + 9.24) \qquad (11)$$

fits Panton and Linebarger's calculations for a zero pressure gradient with α=1,2 and 3 with Coles' wake parameter Π=0.6 where

$$U_\tau\delta/\nu = K(U_e\delta_1/\nu - 65)/(1+\Pi) \qquad (12)$$

Figure 2 shows the results from equations (11) and (12). Panton and Linebarger show that p'/τ_w varies between 2.9 and 3.1 for $4000 \leq Re_\theta \leq 40{,}000$.

Panton and Linebarger also include some calculations of the convective wave speeds for zero pressure gradient flows. Their results show that the wave speed decreases with increasing n or k and increases with increasing Re. The

calculations don't include the cross spectral density or coherence functions. Therefore, comparisons here are restricted to the surface pressure spectra and wave speeds for zero pressure gradient flows.

2.3 SOME PREVIOUS EXPERIMENTAL SURFACE PRESSURE FLUCTUATION STUDIES

Researchers have studied pressure fluctuations in different streamwise pressure gradient flows using different pressure transducers of various sizes. Thus far most studies have been in fair agreement with one another. Corcos (1963) revealed that there is attenuation of the pressure fluctuations at frequencies where the wavelength is of the same order of magnitude or smaller than the diameter, 2r, of the pressure transducer diaphragm. When the length scales of the pressure fluctuations are small, there is an averaging of the amplitudes over the surface of the transducer. Thus, some attenuation occurs at the higher frequencies. Corcos (1963,1967) proposed that a correction be applied to the spectra as a function of $\omega r/U_c$, where U_c is the convective wave speed. The correction amplifies the spectrum by as much as 3 dB for the higher frequencies. Most researchers agree that the attenuation occurs at high frequencies and one must use the correction proposed by Corcos to correct the spectral results as was done here, Schewe (1982) indicated that the

Corcos correction is not large enough when $\omega r/U_c > 4.0$. However, Schewe did not suggest how much larger the correction should be.

Bull and Thomas (1976) performed a study in zero pressure gradient flows using two different transducer mountings. One was a pinhole piezoelectric transducer with the diaphragm recessed from the surface and the other was a piezoelectric transducer mounted flush with the surface. The pinhole transducer caused a small discontinuity on the surface while the flush mounted piezoelectric transducer kept the surface smooth and continuous. The results from Bull and Thomas (1976) show that there is a large difference between transducers. The study then indicated that there was an increase in spectral density for the pinhole transducer for nondimensional frequencies of $0.1 \leq \omega\nu/U_\tau^2 \leq 2.0$. At these frequencies, the wavelengths of the surface pressure fluctuations are on the order of and smaller than the pinhole. The ratio of spectral densities $\phi(\omega)_p/\phi(\omega)_x$ can be as large as 3.5 to 4.0, where the subscript p denotes the pinhole results and the subscript x denotes the flush surface results. Bull and Thomas contend that there is a rather large effect due to interaction of the turbulent boundary layer with the small pinhole. This effect is referred to here as the Bull and Thomas effect. A correction for the spectrum was provided in their paper. However, the correction was not accounted for in the results shown here.

Little explanation of the effect due to the pinhole was provided by Bull and Thomas and was not found elsewhere in the literature.

2.3.1 ZERO PRESSURE GRADIENT

Table 1 gives an overview of earlier experiments performed in zero pressure gradient flows. Various ranges of Re_θ and transducer size were used. The transducer size is perhaps the most important consideration one must look at before comparing works. Figure 3 shows the rms pressure fluctuation nondimensionalized on q_e versus d^+, where d^+ is the nondimensional transducer diameter. The diameter is nondimensionalized on the inner variables, showing some importance on the turbulence-mean shear interaction. The plot shows a decrease in p'/q_e with increasing d^+, where at a certain point p'/q_e becomes constant regardless of d^+. As mentioned previously the resolution of the high frequencies is important, thus the microphone diameter needs to be small to reduce the value of d^+. To reduce the value of d^+ some researchers have used very small sensing diameters, obtained by using a pinhole atop the transducer diaphragm. Blake (1970) and Dinkelacker and Langeheineken (1982) used a pinhole type microphone. Others have used flush mounted piezoelectric or condenser microphones.

Now with the consideration of the size effect, we can make some observations about previous experiments. Figure 2 shows rms pressure nondimensionalized on the wall shear stress. This parameter also shows the turbulence-mean shear interaction which is the dominant feature in wall bounded flows. From the figure p'/τ_w varies between 1.8 and 3.8. Blake (1970) shows that p'/τ_w is approximately 3.6. Blake used pinhole microphones, but as shown in Figure 3 the agreement with other researchers who did not use pinhole microphones is very good. Panton and Linebarger's calculation show p'/τ_w between 2.9 and 3.1.

Most other researchers are below Panton and Linebarger's calculations. Bull and Thomas (1976) show p'/τ_w to be near 2.8, however, as seen in Figure 3 their values of d^+ are nearly the same for Blake (1970) but Bull and Thomas used flush mounted piezoelectric transducers. Schloemer had a fairly large value of d^+, and gives the lowest values of p'/τ_w=1.63. As discussed in Lim (1971), values of p'/τ_w are predicted to range anywhere from 2.56 to 6. However, in a personal conversation with Lim (1971), Hodgson estimates that $p'/\tau_w>4$. Under these considerations, one is led to believe that the larger values of p'/τ_w and p'/q_∞ are correct for smaller d^+.

Table 1 also gives the spectral level for various researchers at a value of the nondimensional frequency, $\omega\delta_1/U_e$=1.0. We see that the spectral level is -51±1.5 dB,

where $dB=10\log_{10}|\phi(\omega)U_e/q_e^2\delta_1|$. This value sets the spectral level because at $\omega\delta_1/U_e=1$ the spectrum is not influenced by the high frequency resolution limitations or the uncertainty of the lowest frequencies. The agreement here is very good. Spectral trends for $\omega\delta_1/U_e\geq1.0$ show that for most experiments the spectrum varies like n^{-1},especially in flows at larger Re_θ values. The spectra tend to drop off much faster above $\omega\delta_1/U_e>5$, where the spectrum varies between n^{-4} and n^{-6}. Figure 4 shows the mean spectral data for several researchers. Fairly uniform trends are seen in the previous works and are nearly independent of transducer type, but are dependent on transducer size.

Cross spectral measurements in zero pressure gradient flows were obtained by Schloemer (1967), Bull (1967), Blake (1970), and Corcos (1964). Corcos (1963) and Brooks and Hodgson (1981) propose that the cross spectrum in either the lateral or longitudinal direction decay exponentially with the phase angle, ϕ, as shown in the equation

$$G_{zx} = \Phi(\omega)\exp(-K_3\omega\Delta z/U_c-K_1\omega\Delta x/U_c+ik\Delta x). \quad (13)$$

In this equation K_1 and K_3 are the decay constants for the cross spectrum and the square root of the coherence, γ. Equation (13) also indicates that $\gamma\propto e^{-K\phi}$

For two different Re_θ, Brooks and Hodgson show that $K_1=0.19$ and 0.14 for $\Delta x/\delta>3$ and $K_3=0.62$ and 0.58,

respectively. For $\Delta x/\delta_1<3$, K_1 was a stronger function of $\Delta x/\delta_1$, with K_1 values as large as 0.23. Although Brooks and Hodgson's study was on a weak adverse pressure gradient flow, the approximately exponential decay is present for both the zero and favorable pressure gradients as well. In the zero pressure gradient case, Bull (1967) and Blake (1970) show good agreement with $K_1 \approx 0.1$ and $K_3 \approx 0.54$ for $\Delta x/\delta_1>3$, for smaller $\Delta x/\delta_1$, Bull found K_1 to be as large as 0.15. These past experiments show that for longitudinal spacings the decay of the cross spectra is small. This says that the pressure fluctuations convecting downstream remain coherent for large distances.

The square root of the coherence in the lateral direction decays much faster than for the longitudinal decay as observed in all previous work. As seen in Table 1 for $\Delta x/\delta_1>3$, the values of K_3 are at least 5 times greater than K_1. This indicates that the pressure fluctuations are not as coherent over the spanwise direction as in the streamwise direction.

Also, the convection velcities at which these fluctuations travel increase with increasing frequency and at high frequencies remain nearly constant at a value between 70 and 80 percent of the free-stream velocity, as shown by Schloemer (1967), Blake (1970), Bull (1967). Schloemer's data show that there is an apparent increase in convection velocity with increased transducer spacing.

2.3.2 FAVORABLE PRESSURE GRADIENT

There are fewer studies of surface pressure fluctuations in accelerating flows than for zero pressure gradient flows. Schloemer (1967), Burton (1973) and Schewe (1983) have performed the bulk of the work for favorable pressure gradient flows and a summary of the results is given in Table 2. As discussed previously, the transducer resolution and size is even more important in accelerating flows because the viscous region is much smaller than in the zero or adverse pressure gradient. This means that for small transducers, the nondimensional diameter, d^+ is larger for the same transducer in a zero or adverse pressure gradient flow. Therefore, one must closely examine the data for resolution and transducer size. None of these previous researchers have used a pinhole transducer in a favorable pressure gradient flow. Figure 3 shows that, for the favorable pressure gradient case as well, the value of p'/q_e increases with decreasing d^+. This is not surprising since from previous discussion we know that the resolution increases with decreasing transducer diaphragm size. The data for the favorable pressure gradient flow follows a similar trend as seen for the zero pressure gradient case. Figure 5 shows p'/τ_w verses displacement thickness Reynolds number. Burton (1973) shows p'/τ_w is near 2 for several Reynolds numbers, but the value of d^+ is relatively large. Schloemer (1967)

gives p'/τ_w near 1 and has a very large d^+. Schewe (1982) gives values of p'/τ_w between 2.48 and 1.2 for various d^+. Schewe's and Schloemer's data for the larger d^+ suffer from poor transducer resolution and we can conclude that the data for the smaller d^+ are more correct. Bull's (1967) slightly accelerating flow shows p'/τ_w to be 2.1 to 2.8 for relatively large d^+. Burton's, Schloemer's, and Schewe's data agree well for similar values of d^+, adding more confidence to the fact that Schewe's smallest d^+ gives the most reasonable value.

Comparing the spectral levels at $\omega\delta_1/U_e=1$, we see that $10\log_{10}|\phi(\omega)\ U_e/q_e^2\delta_1|$ is approximately -49±2.5 dB. The spectral level for the favorable pressure gradient flow is slightly higher than for the zero pressure gradient flow. The region of n^{-1}, spectral variation seems to be present for most of the previous work, however, the region spans over a smaller variation of $\omega\delta_1/U_e$ than for the zero pressure gradient flow. At the higher frequencies, the spectral level varies much like the zero pressure gradient, but the frequency at which the drop off occurs is lower than for the zero pressure gradient flow. Thus, there is not as much energy at the highest frequencies in the favorable pressure gradient flow. Figure 4 shows a plot of the mean spectra from several researchers.

Cross spectral measurements in accelerating flows were performed by Burton and Schloemer. The square root of the

coherence shows an approximately exponential decay in both longitudinal and lateral directions. The longitudinal decay is given by the constant K_1 and we see that both Burton and Schloemer show $K_1 \approx 0.1$ for $\Delta x/\delta_1 \geq 3$ or so. This is a slightly slower streamwise decay as compared to the zero pressure gradient case. The decay for the lateral direction is given by $K_3 \approx 0.4$ which is again a slower decay compared to the zero pressure gradient flow. The reason for the slower decay is the fact that in an accelerating flow the flow is self-similar and more coherent over much greater streamwise and spanwise directions. This leads to the pressure fluctuations being coherent for longer distances in both directions.

The convection velocities of these fluctuations are shown to increase with increasing frequency and become nearly constant at higher frequencies. When the convection velocity becomes constant, it remains at a value between 50 to 60 percent of the free stream velocity. Burton and Schloemer both show this trend. The constant value of the convection velocity is about 10 percent lower in a favorable pressure gradient flow than a zero pressure gradient flow. Schloemer also shows that the wave speeds are a function of the transducer spacing, and Brooks and Hodgson show this for an adverse pressure gradient. Physically, this trend is hard to believe since the spacing can have no direct effect on the flow. However, we can say that the more coherent large-scale

structures contribute more to the apparent convection speed at increasing spacing, which tends to make the convection velocity appear to be a function of the transducer spacing.

3.0 DESCRIPTION OF THE WIND TUNNEL AND TEST FLOWS

3.1 WIND TUNNEL

The wind tunnel used at Virginia Tech is the same facility used in previous work at Southern Methodist University (Simpson, et al., 1981; Shiloh et al., 1981; and Simpson et al., 1983). The mainstream flow of the blown open-circuit wind tunnel is introduced into the test section after passing through an air filter, air chiller, blower, fixed-setting flow damper, a plenum, seven screens for removal of some free stream turbulence and finally through a four to one contraction ratio nozzle to accelerate the flow to test speed and to remove additional free-stream turbulence intensity.

Figure 1 is a side view of the eight meter long and 0.91 meter wide test section. The side walls are made of plate float glass, while the upper wall is plexiglas. The zero and favorable pressure gradient flows are obtained by placing sections of plywood inside the test section and supporting the 'false upper wall' from above. The supports allowed for adjustments to the wall to obtain the desired contour. Figure 1 shows the wall contour for both flows. The solid and dashed lines are the contours for the zero and favorable streamwise pressure gradients, respectively. The corner gaps

between the false wall and glass side walls were covered with a flexible polyurethane plastic sheet for preventing flow leakage at these corners. The boundary layer along the test section was turbulent. In order to insure turbulent flow, a 6 mm forward facing step at the leading edge of the test wall for the test section was used to trip the boundary layer.

3.2 TEST FLOWS

Measurements of test flow velocities were obtained by Ahn (1986) using a single channel hot-wire anemometer. For all measurements the temperature was 25±0.5 °C and $\nu=1.56\times10^{-5}$ m^2/s. Two different zero pressure gradient flows were used to obtain data. In both of these flows the flow accelerated for the first 1.6 m of the test section. All measurements of the zero pressure gradient flows were obtained at downstream streamwise stations (Table 3). The higher speed flow for the zero pressure gradient was used to obtain data at high values of Re_θ. Both flows are not exactly zero pressure gradient flow since the free-stream velocity is nearly constant but has a ±0.3 m/s variation. Table 4 shows that the acceleration parameter $K=(\nu/U_e^2)dU_e/dx$ is about 2×10^{-7} over most of the measured length of the favorable pressure gradient flow.

Tables 3 and 4 give the boundary layer properties for all test flows derived from measured velocity profiles. For

the zero pressure gradient flows, the boundary layer profiles were measured at several streamwise locations. For the streamwise locations where hot-wire measurements were not obtained we can linearly interpolate to get the desired boundary layer quantities. In the favorable pressure gradient case it is not as simple to obtain these values. We must use a momentum integral technique to calculate the boundary layer properties at x-locations not measured with the hot-wire. The equation used to calculate the boundary layer properties is the following,

$$\theta(x)^{5/4}U_e(x)^{4.11}/\nu^{1/4} - \theta(x_o)^{5/4}U_e(x_o)^{4.11}/\nu^{1/4} = 0.016\int_{x_o}^{x} U_e^{3.86}dx. \qquad (14)$$

This equation is derived from the momentum integral equation, the Ludwieg-Tillmann skin friction equation, and an assumed constant shape factor, H=1.29 (Kays and Crawford, 1980). The skin friction coefficient was obtained from the slope of the semi-logarithmic velocity profile region in clauser plots, which is very close to the skin friction coefficient calculated from the Ludwieg-Tillmann equation (Ahn,1986)

$$C_f = (0.246x10^{-0.678H})(U_e\theta/\nu)^{-0.268}. \qquad (15)$$

Results for $\sqrt{C_f/2}=U_\tau/U_e$ from the Ludwieg-Tillmann equation are presented in the tables.

For the zero pressure gradient cases, the boundary layer properties agree with previous studies and give us confidence that the boundary layers are normal two-dimensional boundary layers (Ahn,1986). The trends show that δ and δ_1 increase nearly proportional to $x^{0.8}$ while the skin friction coefficient decreases nearly proportional to $x^{-0.2}$

For the favorable pressure gradient case, the boundary layer properties also indicate a good two-dimensional turbulent boundary layer. The trends also show an increase in δ and δ_1 with increasing x, up to a point where the streamwise pressure gradient causes δ and δ_1 to decrease with increasing x. This streamwise variation of δ_1 is also predicted by equation (14) and is discussed in more length by Ahn (1986). The skin friction coefficient shows a decrease and then an increase with x. Re_θ, U_τ and τ_w all show an increase in increasing x. The internal self-consistency of the data provides additional confidence in the quality of this experimental flow (Ahn, 1986).

U^+ versus y^+ velocity profiles near the wall are in good agreement with earlier studies. The semi-logarithmic velocity profile region is well-defined and ranges from y^+ of 30 to 1000 for increasing Reynolds numbers. The data collapse along the Coles equation for the semi-logarithmic region. The wake region is well defined beginning at the point where the velocity profile breaks away from the semi-logarithmic region. Also, there are some data points

in the viscous sublayer, which indicates that we do have flow over a smooth plate. The spectra of the velocity fluctuations has also been obtained and are presented by Ahn (1986).

4.0 INSTRUMENTATION AND EXPERIMENTAL TECHNIQUES

4.1 INSTRUMENTATION

4.1.1 MICROPHONES

The surface pressure fluctuations and cross spectra are measured using small condenser microphones mounted flush to the test section floor. The microphones used are manufactured by Knowles Electronics, Inc. Two different orifice size microphones were used to obtain the data. Model BT-1755 has a relatively large orifice of 1.4 mm in diameter and model BT-1753 has a smaller orifice 0.51 mm in diameter. Both models can be classified as pinhole type microphones for use in these measurements, and are shown in Figure 6. These microphones are used because of their sensitivity, relatively small size and relatively flat response curve over the low frequency range of interest. Figure 7 shows the sensitivity as a function of frequency. From this figure we see that the response is nearly constant at low frequencies from 125 Hz up to approximately 3 kHz. The response peaks near 5 kHz and then decreases with increasing frequency. Also shown are the differences in response at higher frequencies for the two models. The previous experiments done in this wind tunnel by Simpson *et al.* (1983) used Sennheiser MKH-110 13 mm

diaphragm diameter microphones that were calibrated by the manufacturer. For the present experiments a Sennheiser microphone was used as a base standard microphone for a comparison calibration with the Knowles microphones. Figure 7 shows the manufacturer's response curve for the Sennheiser microphone. The Sennheiser sensitivity is nearly constant between 50 Hz up to 2 kHz.

The Knowles BT-1755 has a rather large orifice for surface pressure measurements. In an effort to reduce inflow and outflow through the pinhole opening, which may be related to the Bull and Thomas effect, these orifices are covered with a small screen as seen in Figure 6. The screen is made by Endevco, Inc. and is used on their models of miniature pressure transducers. Use of these screens did not affect the overall response of the Knowles microphones, but helped provide surface continuity. This can be stated as a result of calibrations performed with and without the screens in place.

4.1.2 MICROPHONE HOUSING UNIT

A unit housing the microphones was designed and used for the measurements. A schematic of the housing unit is shown in Figure 8. The unit houses three microphones, two BT-1755 and one BT-1753. The housing unit containing the microphones was mounted flush with the surface of the flat plate test

surface and supported from the floor beneath the wind tunnel. The diameter of the unit is 25.4 mm, which is smaller than the hole in the test surface, which is 28.6 mm in diameter. The purpose for this is to prevent vibration from the tunnel contaminating the spectral measurements. The gap left in between is covered with 0.003 cm thick cellophane tape which provides continuity of the surface and yet prevents transmission of vibration to the housing unit. Application of the tape does not contribute to the surface roughness because the thickness of the tape is much smaller than the viscous sublayer.

The housing unit can also be used for cross spectral measurements. One of the BT-1755 microphones is mounted so it can traverse some distance with respect to the other BT-1755 microphone. Using this feature, we can obtain cross spectral data for both the streamwise and spanwise spacings. When obtaining the cross spectral data, the line between centers of the microphones must be aligned parallel or perpendicular to the flow for measurement of the respective cross spectrum. The housing units were used in pairs at each streamwise location, with the same model microphone in each unit used in pairs for measurement of the power spectrum.

4.1.3 CALIBRATION

The Knowles microphones were calibrated using two separate techniques. First a comparison method using a Sennheiser model MKH-110 as a reference microphone, calibrated by the manufacturer, was used for calibration in the frequency range from 4 kHz to 10 kHz and sound pressure levels (SPL) between 60 dB to 119 dB. The response curve for the Sennheiser microphone is shown in Figure 7. A second method using a GenRad model 1986 Omnical Sound Level Calibrator was employed for the frequency range from 125 Hz to 4 kHz. Use of both methods gave a small region of overlap around 4 kHz. Results from both methods gave agreement within 1.5 dB in the overlap region.

The comparison calibration method was performed in a semi-anechoic 1.22 m cubed chamber built by the author. The chamber is constructed of plywood and is lined on the inside with three inch thick acoustic-wave absorbing foam (Sonex "anechoic wedges") that absorbs all energy above 500 Hz. The best results for these calibrations were obtained during hours when the low frequency noise and vibrations from the surroundings were smallest and did not interfere with the calibration. The Sennheiser and Knowles microphones were placed inside of the chamber along with a sound source, a Radio Shack Realistic Super Tweeter, catalog no. 40-1380. A

function generator produced a sinusoidal signal that was fed to an amplifier and then to the speaker.

The low frequency calibation using the GenRad also generated a certain frequency sound at discrete but known SPL. Knowing the SPL and measuring the output voltage one can simply calculate the sensitivity of the microphone in mV/Pa as a function of frequency. Using these calibration method the Knowles microphones showed a response nearly independent of SPL.

The overall calibration of the Knowles microphones showed good agreement within ±1.5 dB of the manufacturer's specifications for all microphones and models used in these experiments. The manufacturer's response curves were used in the data reduction as shown in Figure 7. Simplification of the signal processing was possible since each Knowles microphone of a given model had the same frequency response curve within 1.5 dB.

4.1.4 OTHER INSTRUMENTATION

Additional equipment was used for the power supply, data acquisition, data reduction and plotting. A Hewlett Packard model 6213A power supply was used for the microphones power source. A four channel Data 6000 model 611 and model 681 disk drive by Data Precision was used for acquisition and storage of data. Also a TSI model 1015C correlator was used to add

and subtract the time-varying output signals from the microphones before processing in the data acquisition system. The surface pressure measurements were monitored on a Princeton Applied Research model 4512 FFT Real Time Spectrum Analyzer to insure that data were acquired from well-behaved signals. The data reduction was performed using an IBM PC and IBM 370. The results were plotted using a Hewlett Packard 7475A plotter and Versatec plotter.

4.2 EXPERIMENTAL TECHNIQUES

The measurement of the surface pressure spectra was obtained using the model microphone pairs on the two housing units widely separated in the spanwise direction. The microphone pair of model BT-1755 on each unit was used to measure the cross spectra for both the spanwise and streamwise spatial separations. Through manipulation of the output signals we can obtain a single surface pressure spectrum of only the pressure fluctuations due to the turbulent flow field. This single spectrum does not contain any apparent influence of the acoustic disturbances and flow unsteadiness generated by the blower. This measurement technique was previously used successfully in the experiments performed by Simpson et al. (1983).

4.2.1 DATA ACQUISITION AND SIGNAL PROCESSING

Acoustic waves and flow unsteadiness generated by the tunnel are present and must be accounted for. The acoustic waves and flow unsteadiness are assumed to be the same at a given streamwise location at any instant in time because the tunnel test section acts like a wave-guide. The turbulent spectrum produced by the flow was the same across the test section at a given streamwise location because the mean flow and mean square turbulence structure was two-dimensional in nature across the center of the flow. The acoustic and turbulent signals are uncorrelated since the turbulent pressure fluctuations were generated in a volume local to a measurement position while the inviscid acoustic and unsteady fluctuations were generated far upstream. Equations (7) and (8) show that the turbulence produced is due to the local velocity field. This observation allows us to decompose the surface pressure fluctuations into acoustic and turbulent terms. The two housing units shown in Figure 8 were spaced one-third of a meter apart in the spanwise direction. This distance is greater than 4.5 δ in the spanwise direction for the thickest boundary layer examined. Therefore, the turbulent pressure signals produced were uncorrelated, yet were statistically the same since the mean flow was 2-D in structure. The decomposition of the time-varying pressure fluctuation signals for a given frequency n, is written as

$$p_{1n} = p_{1an} + p_{1tn} \qquad (16a)$$

$$p_{2n} = p_{2an} + p_{2tn} \qquad (16b)$$

The subscripts a and t designate the acoustic and turbulent pressure fluctuations, and the subscripts 1 and 2 denote the two microphone housing units. Subtracting p_{2n} from p_{1n} we can obtain the mean square value of the turbulent-flow produced pressure fluctuation as a function of frequency, n

$$\overline{p_{1tn}^2} = \overline{(p_{1n}-p_{2n})^2}/2. \qquad (17)$$

This term is the contribution of the turbulent term to the spectrum. The above equation is true because the following conditions exist for the test flows.

$$\overline{p_{1tn}^2} = \overline{p_{2tn}^2}$$

(mean 2-D flow)

$$\overline{p_{1an}p_{1tn}} = \overline{p_{2an}p_{2tn}} = \overline{p_{1an}p_{2tn}} = \overline{p_{2an}p_{1tn}} = 0$$

(uncorrelated turbulent and acoustic contributions)

$$\overline{p_{1tn}p_{2tn}} = 0$$

(uncorrelated turbulent contribution)

$$p_{1an} = p_{2an}$$

(same acoustic signals)

Using the same conditions above, addition of the signals gives the acoustic contribution as a function of frequency for the acoustic spectrum

$$\overline{p_{1an}^2} = \overline{(p_{1n}+p_{2n})^2}/4 - \overline{p_{1tn}^2}/2. \quad (18)$$

The proper turbulent spectrum is obtained using equation (17) for frequencies below c/w, where w is the width of the test section. The longitudinal, vertical and spanwise acoustic contributions that are the same at the two microphone units are eliminated using this equation at the same streamwise location. However, anti-symmetric spanwise acoustic contributions near the frequency c/w and higher harmonics are added to the spectrum. The turbulent contributions for these frequencies are obtained using the following equation

$$\overline{p_{1tn}^2} = \overline{(p_{1n}+p_{2n})^2}/2. \quad (19)$$

No anti-symmetric spanwise acoustic contributions were observed in these experiments. This led to great simplification in data reduction for the present experiments.

The convective wave speeds and the coherence signals were measured using a like microphone pair, Knowles model BT-1755, on one unit but spaced some small distance apart in either the streamwise or spanwise directions. The wave speed or celerity as a function of n is given by the following equation

$$U_{cn} = 2\pi n\Delta x/\phi_n \qquad (20)$$

where

$$\tan\phi_n = I_n/R_n \qquad (21)$$

and

$$\gamma^2(\Delta x,n) = R_n^2+I_n^2. \qquad (22)$$

Here R_n is the normalized co-spectrum of the two signals while I_n is the normalized quadrature; the power spectra of the two signals were used in this normalization. A similar equation can be written for the spanwise direction. Because the acoustic contributions at two different streamwise locations are coherent but time delayed, they can be

accounted for from the measured acoustic spectra. They make negligible contributions to the co-spectrum and quadrature for the experiments reported here.

The signals from each microphone were input into the TSI correlator where addition and subtraction of the time dependent signals were performed. The response of all microphone pairs were nearly identical, therefore the condition that allows us to use equation (17) holds true for all measurements. Data acquisition was performed by the Data 6000 on the output signals of the correlator. The Data 6000 performs a FFT on 0.1 seconds of data for the sum and difference of the two microphone signals. The respective power spectra or cross spectra for 100 successive 0.1 seconds records were averaged to obtain the resultant power spectra or cross spectra, respectively. The raw data were stored on a diskette for additional reduction.

4.2.2 UNCERTAINTY ESTIMATION

The measurement error in the velocity data obtained by the hot-wire anemometer were within ±1 percent uncertainty for the mean velocity and about ±4 percent uncertainty for the rms velocity (Ahn, 1986). The experimental uncertainty for the pressure fluctuations was within ±1.5 dB in spectral level including effects of finite bandwidth and finite record length (Bendat and Piersol, 1971). The uncertainty increases

at the lowest and highest frequencies in the range of interest. The coherence was as much as ±10 percent uncertain for $0.2<\phi<20$ but at the lowest and highest values of the phase angle, ϕ, the coherence data were more uncertain, by ±0.1. As pointed out on pp. 193-196 of Bendat and Piersol (1971), this uncertainty can be expected for the record lengths used here and for the frequencies with the lowest coherence. Some relatively small uncertainty in the cross spectral data was introduced because of a slight phase difference between microphones which is approximately ±5.5°. Thus, the wave speed data are about ±10 percent uncertain because of the uncertainties in the cross-spectral data.

5.0 EXPERIMENTAL RESULTS

5.1 SURFACE PRESSURE SPECTRA

The results presented are for two different streamwise pressure gradient flows, two with a zero pressure gradient and one with a favorable pressure gradient. For both flows both Knowles BT-1753 and BT-1755 microphones were used. Results vary between the different microphone models. This is reasonable because previous discussion has pointed out the variation in previous results due to different sensing diameters of the transducers. The spectral data presented here are mainly for the results obtained using the smaller orifice microphone, model BT-1753. However, spectral data for the model BT-1755 are presented only for the zero pressure gradient case to illustrate the differences in the results. The Corcos size resolution correction was applied to the data presented here. The spectral data are nondimensionalized to facilitate the task of presentation and comparison. The spectral density are nondimensionalized using the inner wall variables and different combinations of the outer boundary layer variables. Each nondimensional grouping helps display different characteristics of the pressure spectra.

5.1.1 ZERO PRESSURE GRADIENT FLOW RESULTS

First, the results of the zero pressure gradient flow experiments are plotted in Figures 9 through 15. Figure 9 shows the spectra for all momentum Reynolds numbers nondimensionalized on the outer region variables U_e, δ_1, and the wall shear stress τ_w. The plot shows that this grouping of variables does not collapse the spectra very well. The region that does collapse well is where the spectra varies like n^{-1} for $1.28 \leq \omega\delta_1/U_e \leq 6$ and only for the momentum Reynolds number greater than 5000. The spectral data also collapse for $0.1 \leq \omega\delta_1/U_e \leq 1.0$ and vary like $n^{-0.7}$. The spectra show that the fluctuations that contain the most energy occur over a broadband of frequencies somewhere between 80 and 5000 Hz. The frequencies below 80 Hz and above 5000 Hz make small contributions to the rms pressure fluctuation.

Figure 10 shows that the grouping of the inner variables collapse the data over a larger range of momentum Reynolds numbers at the higher nondimensional frequencies. In this figure, we see that the spectra collapse for nearly all frequencies shown. Only for the smallest two momentum Reynolds numbers at the middle to higher frequencies do those spectra not collapse well. The region where the spectra vary like n^{-1} can be clearly seen, and exists for the nondimensional frequency $0.1 \leq \omega\nu/U_\tau^2 \leq 0.5$. This nondimensional plot is perhaps the best since it best shows

the dependency of the wall for nearly all frequencies. Only the large-scale lowest frequency contributions that come from the outer region and are not governed by the wall do not collapse.

Figure 11 and Figure 12 show each individual spectrum in offset plots. In these figures the spectra are nondimensionalized by another set of outer variables, U_e, δ_1, and q_e, and were chosen for the offset plots because the spectra do not collapse very well in these coordinates. If the spectra in Figures 10 and 11 were plotted so as to try to collapse the data, we would see that the spectral level at $\omega\delta_1/U_e=1.0$ is at approximately -50±1.5 dB. These two figures best show the spectral content for each x-location measured. This figure also demonstrates that there is very little scatter in each individual spectrum. These plots also show a n^{-1} variation. The spectral content at higher frequencies beyond $\omega\delta_1/U_e=7.0$ varies like $n^{-5.5}$. One important note is that although the spectra are plotted on three different ordinate scales, the shape of the spectra remains the same and only the dB level changes from ordinate to ordinate.

Figure 13 shows the spectra versus the nondimensional wavenumber $k\delta_1$. The measured wave speeds reported below were used to obtain the wavenumber $k=\omega/U_c$. This figure represents the same coordinates used by Panton and Linebarger (1975). Plotted in this figure are the calculated spectra of Panton

and Linebarger and measured results for nearly the same Reynolds number. The Reynolds number is defined as $U_\tau\delta/\nu$ by Panton and Linebarger. Good agreement can be seen with the n^{-1} or k^{-1} (since U_c is nearly constant) region in the middle wavenumbers. However, agreement becomes poor at the highest and the lowest wavenumbers. Panton and Linebarger's spectra do not fall off as rapidly at the high wavenumbers and at the lower wavenumbers. For the measured spectra, the plot does not extend down below $k\delta_1<0.8$ because of the uncertainty in the pressure spectra and convective wave speeds. Panton and Linebarger show more spectral contribution at the highest frequency, and the agreement here is poor.

Figure 14 and Figure 15 show the nondimensional spectra on an offset plot for microphone model BT-1755. There are several similarities and differences in these plots compared with the model BT-1753. The most noticeable difference is a large peak in the spectra. The peak occurs at approximately 5625 Hz for all x-locations, suggesting a microphone dependent effect. The peak first occurs at $\omega\delta_1/U_e=5$ and then increases to $\omega\delta_1/U_e=19.5$ with increasing momentum Reynolds number. Another difference is that at frequencies beyond the peak, the spectra vary like n^{-3}. The best agreement with data from BT-1753 occurs where $\omega\delta_1/U_e=1$, with the spectral level at approximately -50±3 dB. A region of n^{-1} exists for most x-locations, and exists between $2.0\leq\omega\delta_1/U_e\leq10$. The region is very small at low momentum Reynolds number and increases

in range as momentum Reynolds number increases. This effect was also seen in the results from microphone model BT-1753 in Figure 11 and Figure 12.

Figure 2 and Figure 3 show the results of the rms pressure fluctuations nondimensionalized by the wall shear stress and free-stream dynamic pressure. In the first of these figures we see values of $3.258 \leq p'/\tau_w \leq 3.8$ for transducer BT-1753. The transducer BT-1755 gives values of $2.68 \leq p'/\tau_w \leq 3.17$. The differences in levels is seen by the fact that we have two different orifice size transducers. Further examples of this can be seen in Figure 3 where p'/q_e decreases with increasing d^+ This further demonstrates the dependence of rms pressure fluctuation on the sensing diameter. Figure 2 also indicates that p'/τ_w increases with increasing Reynolds number. Furthermore, Figure 3 also shows that p'/q_e increases with the Reynolds number.

The Corcos correction has been applied to the data and was observed to have a 1 dB effect at $\omega\delta_1/U_e=0.83$ for the BT-1753 data at x=1.63 m. The nondimensional rms pressure fluctuation was also affected. The rms pressure fluctuation increased about 30 percent for the BT-1753 and 50 percent for the BT-1755. This is understandable because the larger the orifice, the larger the correction. However, the Corcos correction did not equalize the rms pressure fluctuations from the two model microphones but only brought them closer in magnitude than before the correction was applied.

5.1.2 FAVORABLE PRESSURE GRADIENT RESULTS

The spectral data presented for the favorable pressure gradient is restricted to microphone model BT-1753 but will include some discussion of the results from model BT-1755. The spectral results are presented in the same nondimensionalized plots as for the zero pressure gradient flow. Figure 16 shows a plot of the measured pressure spectra in the first group of the outer boundary layer variables. This plot indicates that the spectra collapse fairly well using this grouping for $0.1 \leq \omega\delta_1/U_e < 3.0$. The agreement in the middle range of frequencies is very good and similar in range to the zero pressure gradient results. These variables collapse the lower frequencies better for the favorable pressure gradient flow than the zero pressure gradient flow. For the higher frequencies, we can also see that this group of variables does not collapse the data. These are similar trends between the zero and favorable pressure gradient flows. There are several trends that do not appear in the accelerating flow results; one of them is the existence of a region that varies like n^{-1}. The spectral data show a region that varies like $n^{-0.7}$ for $0.7 \leq \omega\delta_1/U_e \leq 2.0$. Another trend that is different is the frequency at which the spectra begin to rapidly decrease with frequency. This occurs very near $\omega\delta_1/U_e = 3.0$ while for the zero pressure gradient the fall off occurs at $\omega\delta_1/U_e = 7.0$ for the larger

Reynolds numbers. Another difference is the variation of the spectra at the highest frequencies. For the favorable pressure gradient flow, there was some variation in the slope of the spectra at the higher frequencies between n^{-5} and n^{-6}, and the variation is more negative with increasing Reynolds number. However, for the zero pressure gradient flows the spectral variation remained nearly the same at about $n^{-5.5}$ for all Reynolds numbers.

Figure 17 shows that the spectral data nondimensionalized on the inner boundary layer variables collapse very well. As in the zero pressure gradient case, the inner variables take care of the nondimensionalization for nearly the entire range of frequencies. The lower frequencies do not collapse nearly as well, but this too was observed in the zero pressure gradient case. The only other portion of the data not collapsed is in the middle frequencies for the highest momentum Reynolds number case at x=4.77 m.

Figure 18 and Figure 19 show offset plots of the individual spectra nondimensionalized by U_e, δ_1, and q_e of outer boundary layer variables. These plots again illustrate the fact that there is little scatter in a given spectrum. Another observation made is the failure of these variables to collapse the data as well as the variables in either Figure 16 or Figure 17. The three different groups of variables used to nondimensionalize the spectra only have the

effect of shifting the spectra along the ordinate and abscissa, and not changing the shape of the spectra. This was done to facilitate the comparison procedure between different Reynolds numbers. The spectral plots for microphone Model BT-1755 were obtained but not presented because model BT-1753 gave nearly the same results for the favorable pressure gradient flow. The spectral peak at 5625 Hz observed in the zero pressure gradient flows for model BT-1755 occurred in the accelerating flow but was not nearly as noticeable and in some instances it appeared to be absent. The reason for this was that the spectral contribution at these frequencies was much smaller than in the zero pressure gradient case. Also this spectral peak became more apparent as the momentum Reynolds number increased.

Figure 5 shows p'/τ_w versus Re_{δ_1}. We observe from this plot that the nondimensionalized rms pressure fluctuation has a value between 2.6 and 2.9 for model BT-1753 and 2.3 and 2.9 for model BT-1755. These levels are very nearly the same for both microphone models. There is a slight increase of p'/τ_w with an increase of Re_{δ_1} for BT-1753, but BT-1755 shows a slight decrease with increasing Re_{δ_1}. The plot of p'/q_e versus d^+ is shown in Figure 3. Shown here are similar trends discussed for the zero pressure gradient flows. At smaller d^+, the value of p'/q_e is the largest. However, for the model BT-1755, the value of p'/q_e is rather high but is in better agreement with previous research than the zero

pressure gradient flow data from model BT-1755. There seems to be some obvious differences in the zero and favorable pressure gradient flows between the different model microphones.

Corcos' correction was also applied to the spectral data for the favorable pressure gradient flow. The correction was observed to have a 1 dB effect at $\omega\delta_1/U_1=0.88$ for the BT-1753 data at x=1.63 m. The most noticeable observation was the fact that Corcos' correction brought the rms pressure fluctuation from both model microphones very close in agreement, but the uncorrected data were originally very close in magnitude. This smaller difference in rms pressure fluctuation occurs only for the accelerating flow. This indicates that differences in transducer size is very small in this particular experiment. Application of the Corcos' correction to the two different model microphones did not greatly increase the higher frequency components, thus the rms pressure fluctuation did not increase as much as in the zero pressure gradient case.

5.2 SQUARE ROOT OF THE COHERENCE AND CONVECTIVE WAVE SPEED RESULTS

A pair of model BT-1755 microphones was used to obtain all cross spectral data. The co-spectrum and quadrature were obtained and then the wave speeds and coherence were

extracted from the experimental data. The cross-spectral data were obtained at 10 different microphone spacings in either the lateral, Δz, or longitudinal, Δx, direction. The closest spacing in either direction was 2.413 mm and the largest spacing was 9.172 mm. An attempt was made to obtain data over an even distribution of microphone spacings. The 10 different spacings gave an adequate number of data points to determine both the coherence and the convective wave speeds. Tables 5 and 6 give the values of the microphone spacings for both the zero and favorable pressure gradient flows, respectively.

Figure 20 through Figure 24 show the square root of the coherence obtained in the longitudinal direction in the zero pressure gradient flow. As mentioned in Chapter 2, the square root of the coherence decays approximately like $e^{-K\phi}$, where K is a decay constant. The decay constant, K_1, is 0.2 for the lower Reynolds numbers and increases to 0.3 at the higher Reynolds numbers. Only data between $0.75<\Delta x/\delta_1<2.7$ were obtained at low Reynolds numbers; at high Reynolds numbers $0.20<\Delta x/\delta_1<0.74$. The lateral cross spectra are plotted in Figures 25 through 29. K_3 is approximately 0.7. Values of $\Delta z/\delta_1$ were close to those for $\Delta x/\delta_1$. The parameters that collapse the data for all microphone spacings are $\omega\Delta x/U_c$ and $\omega\Delta z/U_c$. The exponential model does not fit the data as well as these parameters collapse the data,

although at higher ϕ values where the coherence is low it is also uncertain by ±0.1.

The square root of the coherence for the accelerating flow are shown in Figures 30 through 37. The exponential decay constant, K_1 is between 0.1 and 0.2 for the longitudinal direction and decreases with increasing Reynolds number. Values of $\Delta x/\delta_1$ and $\Delta z/\delta_1$ are between 0.75 and 3.35 and increase slightly with Reynolds number. Comparing to the zero pressure gradient flow, the streamwise coherence does not decay as fast. This means that the streamwise extent of the pressure fluctuations remain more coherent in an accelerating flow for larger downstream distances. The decay constant, K_3 is between 0.35 and 0.6 for the lateral coherence. K_3 increases with increasing Reynolds number, which means that the spanwise extent of the pressure fluctuations become less coherent in the spanwise direction as Reynolds number increases.e K_3 is not as large as the decay in the zero pressure gradient flow. This further indicates that the non-dimensional spanwise extent of the pressure fluctuation producing flow structures is greater in the accelerating flow. This means that the large-scale structures are slower to change character or shape in the favorable pressure gradient flow than the zero pressure gradient flow. All cross spectral data showed that the decay in the cross spectra was best defined by the smaller microphone spacings between 2.413 mm and 5.11 mm.

The decay of the square root of the coherence was not as well defined for the larger spacings. The coherence does not go to zero for the largest phase angles mainly because of the experimental uncertainties. This has been observed by all earlier researchers. Both the lateral and longitudinal direction results show this trend but it is much more apparent in the favorable pressure gradient case.

The convective wave speeds are shown in Figures 38 and 39. The wave speed is nondimensionalized by the free-stream velocity and plotted versus $\omega\delta_1/U_e$. In these figures the curve shown is a mean curve for all the results of the present experiment at each x-location for all 10 microphone spacings. The results were not a function of microphone spacing. In both types of flow the wave speed increases with increasing $\omega\delta_1/U_e$ until some maximum is reached and then the wave speed remains nearly constant. In the zero pressure gradient flow at the higher Reynolds numbers, the wave speed reaches a maximum, then decreases slightly where the wave speed then reaches a nearly constant value. This trend also appears to be true for the lower Reynolds numbers in the accelerating flow.

The ratio of U_c/U_e at high values of $\omega\delta_1/U_e$ remains nearly the same for all momentum Reynolds numbers in the zero pressure gradient case. However, for the favorable pressure gradient flow the ratio of U_c/U_e at high values of $\omega\delta_1/U_e$ decreases with increasing Reynolds number.

In the zero pressure gradient flow, the wave speed at higher frequencies remains constant between 56 and 50 percent of the free stream velocity for $\omega\delta_1/U_e \geq 0.5$ with U_c/U_e decreasing with increasing Re. For the favorable pressure gradient case the ratio of U_c/U_e remains nearly constant when $\omega\delta_1/U_e \geq 5$ and ranges in value between 64 and 53 percent of the free stream velocity. The level where U_c/U_e is constant, decreases with increasing Re. The wave speed data presented for each x-location is a mean curve of the data from all ten Δx spacings. The scatter in the data, which is not shown in the figure, is about ± 10 percent for each streamwise location in the mid-frequency range. The most scatter occurs for the smallest and largest values of $\omega\delta_1/U_e$. Therefore, the data were not presented at these values of $\omega\delta_1/U_e$.

6.0 DISCUSSION

In the previous chapter, only a discussion of the present results was given. In the present chapter, the discussion centers on comparisons with previous studies.

6.1 SURFACE PRESSURE SPECTRA COMPARISONS

The Introduction and Tables 1 and 2 give a brief overview of the results from previous experiments. Tables 3 and 4 are results from the present studies. First, in comparing the results of the zero pressure gradient flow with others, we can examine the approximate level of the spectral data. The level of the spectra at $\omega\delta_1/U_e=1.0$ gives the best point of comparison because the low frequency noise and high frequency resolution problems are small. For all studies including the present, the spectral level is very near -50±3 dB, where $dB=10\log_{10}|\phi(\omega)U_e/q_e^2\delta_1|$. As discussed in Chapter 5, this grouping of variables does not collapse the data well, but is used because most of the previous results were nondimensionalized by this group of variables. The agreement is good for a wide range of momentum Reynolds numbers. The shape factor, H is approximately 1.3 and $0.031\leq U_\tau/U_e\leq 0.04$, indicating similar boundary layer characteristics for nearly all other previous research.

Many of the differences among different studies can be attributed to the microphone resolution effect as shown in Figure 3. The present study has the best resolution and the smallest value of d^+. The present data are also plotted here and show excellent agreement with Blake (1970), Dinkelacker et al. (1977) and Emmerling (1972) all of whom used transducers with values of d^+ close in magnitude to the present study. Bull and Thomas (1976) show values of p'/q_e some 30 percent lower in magnitude than the consensus of other experiments. Bull and Thomas claim their data are more correct and that Blake's results were too high. As the present study, Blake used pinhole microphones. However, it is difficult to say the pinhole effect has caused values of p'/q_e to be too high because the data from Dinkelacker and Langeheineken (1982), Emmerling (1973) and Schewe (1982), who used flush mounted surface transducers, are in agreement with Blake (1970) and the present data.

The Bull and Thomas correction was applied to some of the present data and was observed to overcorrect the data. This can be stated because for the present data values of d^+ are smaller than for Bull and Thomas and when the correction was applied the value of p'/q_e was nearly the same when compared to the values given by Bull and Thomas. However, we know that the ratio of p'/q_e increases with decreasing d^+. Thus, it is the opinion of the present researchers that the Bull and Thomas effect may exist, but is not as large as

claimed by Bull and Thomas. For the present data, there are distinct differences between the values of p'/q_e for the two different pinhole sizes. The lower p'/q_e at the larger d^+ for model BT-1755 is seen in Figure 3. The effect of transducer size is clearly shown by the past and present data.

Figure 10 shows the mean spectra line from Bull and Thomas (1976) for the zero pressure gradient flow. Spectral shape and distribution are in fair agreement. The part that least agrees is in the region $0.3 \leq \omega\nu/U_\tau^2 \leq 0.7$. This region is where Bull and Thomas showed the pinhole effect to be most significant. The difference in spectral level is between 2 to 3 dB in the mid to high frequency range.

For the favorable pressure gradient flow, the consensus level of the spectra at $\omega\delta_1/U_e=1$ is at approximately 49±2 dB, where $dB=10\log_{10}|\phi(\omega)U_e/q_e^2\delta_1|$. The spectral level for the favorable pressure gradient appears to be about 1 dB higher than the zero pressure gradient. The favorable pressure gradient flows have been performed over a large range of Re_θ and d^+. U_τ/U_e ranges from 0.04 to 0.05 for all the accelerating flows. The shape factor, H is approximately 1.3 for most of the previous studies as well as the present study.

The data of Burton (1973) and the present data show that there is a small affect on p'/q_e due to the streamwise

pressure gradient at small values of d^+. The trend seems to indicate that p'/q_e is relatively constant for small d^+.

Figure 4 shows several mean spectra for Schloemer (1967), Blake (1970), Burton (1973), and the present study. Spectra from both zero and favorable pressure gradients are shown in this figure. These curves represent mean curves of the results for a particular study. The levels of the spectra are nearly the same at $\omega\delta_1/U_e=1.0$ for different streamwise pressure gradients. Shown best on this plot is the difference in high frequency spectral content. The zero pressure gradient flow spectra show much more spectral content at the higher frequencies than the favorable pressure gradient flow spectra. However, when the spectra are nondimensionalized on ν and U_τ we observe a collapse of the data independent of streamwise pressure gradient, indicating that this grouping of inner variables will collapse the spectral data best. At smaller Reynolds numbers for the favorable pressure gradient flow there is less energy at the higher frequencies when compared to the zero pressure gradient flow.

Another important trend in the data deals with the variation of the spectrum when values of $\omega\delta_1/U_e$ are between 1 and 28. Bradshaw (1967) indicates that spectra should vary like n^{-1} in an overlap region and Panton and Linebarger (1973) use this to predict their spectral data as a function of wavenumber, k. The overlap region exists in the spectra

where the inner wall variables and outer variables both scale flow phenomena and each can be used to nondimensionalize and collaspe the surface pressure spectral data. The present results for the zero pressure gradient flow show the existence of this region between $1 \leq \omega\delta_1/U_e < 6$ for $Re_\theta > 5000$. For $Re_\theta < 5000$ the zero and favorable pressure gradient flow show a variation more like $n^{-0.7}$. The predicted overlap region is quite large and is shown to exist for over a decade by Panton and Linebarger (1973). However, the data presented here along with others show a much shorter region. Spectra presented by Schloemer (1967) and Burton (1973) do not show the existence of the overlap region for either the zero or favorable pressure gradient flows, but their $Re_\theta < 5000$. Other researchers show a n^{-1} region ranging from $1 \leq \omega\delta_1/U_e \leq 20$. Bull (1967) shows the largest region. Bull (1967), Schewe (1982) and Dinkelacker et.al. (1977) also show the existence of the n^{-1} in duct flows. The frequency range of the overlap region increases in with Re_θ. Further comparison can be seen in Figure 13, in the coordinates $10\log_{10}|\phi(k)/\tau_w^2\delta_1|$ versus $k\delta_1$. Panton and Linebarger's calculation is plotted along with the present results and we can see the overlap region. The present data only have the k^{-1} region between $4.0 \leq k\delta_1 \leq 10$ but Panton and Linebarger show the region between $2.5 \leq k\delta_1 \leq 30$. The spectra are not plotted below $k\delta_1 < 0.8$ because of large uncertainties in the frequency content and convective wave speeds in the present data. Also, the higher wave numbers

show a faster drop off than do Panton and Linebarger. Panton and Linebarger also observed this when comparing their calculations to the experimental results of Willmarth and Roos (1965) and suggested that the transducer resolution is the reason for this faster drop off.

At the higher frequencies the present results show that the spectrum varies like $n^{-5.5}$. This fall off in spectral content is due to either a real effect of the flow or by the resolution of the transducer. Previous Corcos corrected results with various d^+ diameter transducers show a variation like n^{-3} to n^{-4}, which is not as steep as for the present results but indicates that the surface pressure spectra may drop off fast. This means that the drop off in the spectral content may be a real occurrence and not due to resolution of the transducers. The present favorable pressure gradient flow also shows a rapid drop off of n^{-5} to n^{-6} in spectral content for the higher frequencies while previous studies show a spectral variation like $n^{-3.3}$ to n^{-4}. However, there is some indication that the spectral drop off is real and not just due to the resolution problems.

Figure 2 and Figure 5 show p'/τ_w versus Re_{δ_1}. These figures contain the results of several studies, including the present one. Both figures show the slight Reynolds number dependence on p'/τ_w. All studies shown in Figure 2 indicate that there is a slight increase of p'/τ_w with an increase in Re_{δ_1}. Figure 5 shows the dependence of p'/τ_w on

transducer size. For the zero pressure gradient flow, Blake (1970) and the present study agree best. However, both use pinhole type microphones which Bull and Thomas (1976) claim make the results too large. However, in support of the results of this present study, Lim (1971) states that Hodgson had indicated that $p'/\tau_w > 4$ is more correct for a zero pressure gradient flow. The present pinhole data is closest in agreement to Hodgson's value.

p'/τ_w in the favorable pressure gradient is lower in value than the zero pressure gradient. The data plotted in Figure 5 show fairly good agreement between Schewe (1982), Burton (1973) and the present data. In this figure the data by Schewe (1982) show the affect of d^+, but indicate that the smallest value of d^+ gives the highest and most reasonable value of p'/τ_w. It is difficult to say what the value of p'/τ_w should be for the favorable pressure gradient case. The slight Re dependence for the zero pressure gradient flow shows that if you extend a line following the trend down to the lower values of Re, p'/τ_w should be somewhere between 3 and 3.2. This is reasonable since the law-of-the-wall velocity and turbulence structure describes both zero and favorable pressure gradient flows at low Reynolds numbers. Using this as a reference for the level in the favorable pressure gradient flow, the data presented agrees well for similar d^+ for this level of p'/τ_w. The good agreement for the different microphone models used in the present

experiments in the favorable pressure gradient is observed in Figure 5 because the high frequency content in the surface pressure spectra is not as large in the favorable pressure gradient flow as compared to the zero pressure gradient flow. Therefore, the resolution problems are not nearly as large, at least not for the lower Re in the favorable pressure gradient flow. The larger values of Re_{δ_1} show that there is less agreement between the two different size microphones, indicating that the resolution has an affect at these Reynolds numbers. The resolution issue seems to be the best explanation for the agreement between results for different pinhole sizes in the favorable pressure gradient flow and the reason for the large differences in the zero pressure gradient flows.

6.2 SQUARE ROOT OF THE COHERENCE AND CONVECTIVE WAVE SPEED COMPARISONS

Shown previously in Chapter 2 was the exponential decay model equation (13), used by Corcos (1963) and Brooks and Hodgson (1981) to fit their coherence data. Observing the data of Schloemer (1967), Blake (1970), Burton (1973), Bull (1967) and others, we see that their coherence data also decay almost exponentially. In general, the present results seem to follow an exponential decay for $\phi<5$. Tables 1 through 4 show the values of the decay constants K_1 and K_3

for past experiments for $\Delta x/\delta_1>3$ and present experiments. In general, the exponential decay model does not fit the data very well.

Schloemer (1967) first examined the differences in the coherence due to the streamwise pressure gradient. Using the zero pressure gradient case as a basis for comparison, Schloemer indicated that for favorable pressure gradients, the streamwise decay of coherence is slower than for the zero pressure gradient case. However, in an adverse pressure gradient flow, the decay is more rapid. Schloemer also suggested that there is little difference in the lateral decay due to the streamwise pressure gradient. Examining the results of the exponential decay constant, one observes that in most cases this statement is true. In the zero pressure gradient flow the present results gave $0.2\leq K_1\leq 0.3$ and $K_3=0.715$, which shows good agreement with earlier results for $\Delta x/\delta_1<2$. Here, as in earlier experiments the values of K_1 increase with decreasing $\Delta x/\delta_1$ and increasing Reynolds number while K_3 remains constant with decreasing $\Delta x/\delta_1$ and increasing Reynolds number. In the favorable pressure gradient flow the present results gave $0.1\leq K_1\leq 0.2$ and $0.35\leq K_3\leq 0.6$, which shows good agreement with previous research for small $\Delta x/\delta_1$ values. Here values of K_1 increase slightly with decreasing $\Delta x/\delta_1$ and increasing Reynolds number while K_3 increases with decreasing $\Delta z/\delta_1$ and increasing Reynolds number.

It is difficult to determine trends in the previous data for both streamwise pressure gradients because there was little work done over the range of variables. Considering Schloemer's data and his statement above, we can observe that there is little effect due to the pressure gradient. The values of K_1 are nearly the same for both streamwise pressure gradient flows. However, the values of K_3 seem to decrease for the favorable pressure gradient flows. This means that the spanwise extent of the pressure fluctuations in the favorable gradients remains larger as the pressure fluctuations move downstream when compared to the zero pressure gradient flow. Brooks and Hodgson (1981) had a weak adverse pressure gradient and their value of K_3 is in agreement with the favorable pressure gradient flows. The value of K_1 for Brooks and Hodgson show good agreement with both the present zero and favorable pressure gradient flows for some values of $\Delta x/\delta_1$ and $\Delta z/\delta_1$. This seems to indicate that whether the flow is accelerating or decelerating, the longitudinal cross spectra and coherence decay about the same as the zero pressure gradient flow. Also, the lateral cross spectra and coherence do not seem to decay as fast for an accelerating or decelerating flow when compared to the zero pressure gradient flow.

The statement made by Schloemer and discussed above is supported by a paper by White (1964). The paper states that theoretically the longitudinal cross spectral level is

higher, or the decay in the favorable pressure gradient flow is slower than for an adverse or zero gradient pressure gradient flow. White's theory shows little difference in the lateral cross spectral level or decay as a result of the streamwise pressure gradient.

The exponential decay model fits the cross spectral data at the lower values of the phase angle, ϕ, as discussed earlier in this section. The exponential decay model goes to zero quite fast for the values of $\phi>5$, but the square root of the coherence for the present data does not decay to zero for $\phi>5$ for either the spanwise or streamwise direction. The coherence only decays to some level where it then remains nearly constant for increasing phase angle, ϕ. Coherence results for all previous researchers show that when $\phi\geq5$ the coherence also does not go exactly to zero. This occurs at the larger values of the phase angle because the large scale structures in the boundary layer add to the apparent coherence raising the level of the cross spectra, and do not show a decay in the coherence to zero. This occurs in both the streamwise and spanwise directions.

The convective wave speeds are plotted in Figures 38 and 39 for the zero and favorable gradients flows respectively. U_c/U_e increases with increasing $\omega\delta_1/U_e$ up to $\omega\delta_1/U_e\geq0.5$ where U_c/U_e then becomes constant in the zero pressure gradient flow; in the favorable pressure gradient flow U_c/U_e is constant near 0.6 for $\omega\delta_1/U_e\geq5.0$. Blake (1970) and Burton

(1973) show similar results. However, for Blake's zero pressure gradient flow and Burton's accelerating flow, U_c/U_e is constant when $\omega\delta_1/U_e \geq 2.0$. These three studies also show that U_c/U_e reaches a maximum or peak near $\omega\delta_1/U_e=0.5$, then deceases slightly before reaching a constant value of U_c/U_e. Schloemer (1967) and Bull (1967) show different results of U_c/U_e for small values of $\omega\delta_1/U_e$. Their data indicate that U_c/U_e decreases with increasing $\omega\delta_1/U_e$ and then becomes constant for $\omega\delta_1/U_e>2$; values of $U_c/U_e=0.6$ and 0.8 were observed for zero and favorable pressure gradients. Schloemer (1967) also shows a dependence on microphone spacing while Burton (1973) does not. Brooks and Hodgson also show U_c/U_e as a function of spacing. The wave speeds of individual motion are not a function of sensor spacing. Because as the pressure fluctuation producing motions move downstream the slower near-wall small-scale effects die out rather quickly but the faster large-scale motions remain more coherent, whereby indicating a false impression that the convection velocity for a given frequency increases with microphone spatial separation. This effect is also a possible reason why the coherence does not completely decay to zero for large values of ϕ.

Although there is some large degree of uncertainty in the present results of the convective wave speeds, the agreement with previous research is good for both streamwise pressure gradient flows.

7.0 CONCLUSIONS

Here it has been demonstrated that a new experimental technique using two microphones spaced far apart in the spanwise direction was successful in obtaining reasonable and consistent surface pressure fluctuation results for zero and favorable pressure gradient flows.

This investigation provides extensive documentation of the spectral trends and levels for both streamwise pressure gradients. Good agreement was obtained with previous results. p'/τ_w and p'/q_e are functions of Re_θ and d^+.

For the zero pressure gradient flow the spectra at low Re_θ collaspe on the plot of $10\log_{10}|\phi(\omega)U_e/\tau_w^2\delta_1|$ versus $\omega\delta_1/U_e$ for $0.1\leq\omega\delta_1/U_e\leq1.0$ with $n^{-0.7}$. For $Re_\theta>5000$ the spectra collapse on the plot of $10\log_{10}|\phi(\omega)U_e/\tau_w^2\delta_1|$ versus $\omega\delta_1/U_e$ for $1.28\leq\omega\delta_1/U_e\leq6.0$ with $n^{-1.0}$. Also for the zero pressure gradient flow the spectra collapse on the plot of $10\log_{10}|\phi(\omega)/\rho^2U_\tau^2\nu|$ versus $\omega\nu/U_\tau^2$ for $\omega\nu/U_\tau^2\geq0.1$. For $0.05\leq\omega\nu/U_\tau^2<0.1$, the overlap region varies like $n^{-1.0}$ and at the higher frequencies the spectra varies like $n^{-5.5}$

For the favorable pressure gradient flow, which occurs at low Re_θ, the spectra collapse on the plot of $10\log_{10}|\phi(\omega)U_e/\tau_w^2\delta_1|$ versus $\omega\delta_1/U_e$ for $0.1\leq\omega\delta_1/U_e\leq3.0$ and this region varies like $n^{-0.7}$. Also for the favorable pressure gradient flow the spectra collapse on the plot of

$10\log_{10}|\phi(\omega)/\rho^2 U_\tau^2 \nu|$ versus $\omega\nu/U_\tau^2$ for $\omega\nu/U_\tau^2 \geq 0.3$. For $0.01 \leq \omega\nu/U_\tau^2 < 0.3$, the region varies like $n^{-0.7}$ and for the higher frequencies the spectra varies like n^{-5} to n^{-6}.

The spectral data agree well with the calculation method of Panton and Linebarger for the zero pressure gradient flows. Their calculation method does not include accelerating flows, therefore, no comparisons were made. The Bull and Thomas pinhole effect seems to overcorrect when applied to the present data. The Corcos correction seems to correct most of the resolution problems at the higher frequencies where the wavelengths of pressure fluctuation are on the order of the sensing diameter. The best results for the surface pressure fluctuation spectra were obtained using the smaller oriface diameter microphone model BT-1753.

The square root of the coherence demonstrates an approximate exponential decay for small values of the phase angle, ϕ as seen in previous studies. Good agreement with earlier values of the exponential decay constants K_1 and K_3 were observed for $\Delta x/\delta_1 < 3$. The decay of the coherence is defined best by the smaller spatial separations for both streamwise pressure gradient flows. The longitudinal and lateral coherence do not decay to zero because of experimental uncertainties and because the large-scale low frequency structures may make the coherence remain at some finite level for large values of ϕ. The longitudinal coherence decays at about the same rate for both streamwise

pressure gradients. The lateral coherence decays faster in a zero pressure gradient flow than a favorable pressure gradient flow because for the accelerating flow the large scale structures tend to scale on the upstream boundary layer thickness, so the spanwise extent of the correlation remains larger in terms of $\omega\Delta z/U_c$. The longitudinal and lateral coherence tend to collapse for all 10 microphone spacings for all cases in the present study.

Good agreement with previous research for the convective wave speeds was shown. For the zero pressure gradient flow, the ratio of U_c/U_e is near 0.5 for large values of $\omega\delta_1/U_e$ for values of Re_θ>5000. For the favorable pressure gradient flow, the ratio of U_c/U_e is near 0.6 for large values of $\omega\delta_1/U_e$ for values of Re_θ>2440.

REFERENCES

Ahn, S., Master of Science Thesis, Aerospace Engineering Department, Virginia Polytechnic Institute and State University, Blacksburg, VA 1986.

Bendat, J.S. and Piersol, A.G., Random Data: Analysis and Measurement Proceedures, Wiley-Interscience, New York, 1971.

Beranek, L.L., Acoustic Measurements, John Wiley and Sons, Inc., New York, 1949.

Blake, W.K., "Turbulent Boundary-Layer Wall-Pressure Fluctuations on Smooth and Rough Walls," Journal of Fluid Mechanics, Vol. 44, No. 4, pp. 639-660, 1970.

Bradshaw, P., "'Inactive' Motion and Pressure Fluctuations in Turbulent Boundary Layers," Journal of Fluid Mechanics, Vol. 30, No. 2, pp. 241-258, 1967.

Brooks, T.F. and Hodgson, T.H., "Trailing Edge Noise Prediction From Measured Surface Pressures," Journal of Sound and Vibration, Vol. 78, No. 1, pp. 69-117, 1981.

Brooks, T.F. and Schlinker, R.H., "Progress in Rotor Broad Band Noise Research," Vertica, Vol. 7, No. 4, pp. 287-307, 1983.

Bull, M.K., "Wall-Pressure Fluctuations Associated with Subsonic Turbulent Boundary Layer Flow," Journal Fluid of Mechanics, Vol. 28, No. 4, pp. 719-754, 1967.

Bull, M.K., and Thomas, A.S.W., "High Frequency Wall Pressure Fluctuations in Turbulent Boundary Layers," The Physics of Fluids, Vol. 19, No. 4, pp. 5976-599, 1976.

Burton, T.E., "Wall Pressure Fluctuations at Smooth and Rough Surfaces Under Turbulent Boundary Layers with Favorable and Adverse Pressure Gradients," MIT Technical Report No. 70208-9, Department of Mechanical Engineering, Cambridge, MA., June 1973; AD772548.

Corcos, G.M., "Resolution of Pressure in Turbulence," The Journal of the Acoustical Society of America, Vol. 35, No. 2, pp. 192-199, 1963.

Corcos, G.M., "The Structure of the Turbulent Pressure Field in Boundary-Layer Flows," Journal of Fluid Mechanics, pp. 353-378, 1963.

Corcos, G.M., "The Resolution of Turbulent Pressure At the Wall Of a Boundary Layer," Journal of Sound and Vibration, Vol, 6, pp. 59-70, 1966.

Dinkelacker, A., Hessel, M., Meier, G.E.A., and Schewe, G., "Investigation of Pressure Fluctuations Beneath a Turbulent Boundary Layer by Means of an Optical Method," The Physics of Fluids , Vol. 20, No. 10, pp. 216-224, 1977.

Dinkelacker, A., and Langeheineken,T.H., "Relations Between Wall Pressure Fluctuations and Velocity Fluctuations in Turbulent Flow," Max-Planck-Institut für Strömungsfurschong, Göttingen, 1982.

Emmerling, R., "The Instantaneous Structure of the Wall Pressure Under a Turbulent Boundary Layer Flow," Max-Planck-Institut für Strömungsforschung, Nr. 56/1973, Göttingen, July 1973.

Hahn, M., "Turbulent Boundary-Layer Surface-Pressure Fluctuation Near an Airfoil Trailing Edge," AIAA Paper No. 76-336, July 1976.

Hill, R., "Reciprocity and Other Acoustic Emission Transducer Calibration Techniques," Journal of Acoustic Emission, Vol. 1, No. 2, pp. 73-80, 1982.

Kays, W.M., and Crawford, M.E., Convective Heat and Mass Transfer, Second Edition, McGraw-Hill, New York, pp. 174-176, 1980.

Kinsler, L.E., and Frey, A.R., Fundamentals of Acoustics, John Wiley and Sons, Inc., New York, 1962.

Lim, K.B., "A Study of Pressure Fluctuations in Turbulent Shear Flows Under the Effects of Mean Pressure Gradients," Ph.D. Thesis, University of Adelaide, Department of Mechanical Engineering, 1971.

Panton, R.L., and Linebarger, J.H., "Wall Pressure Spectra Calculations for Equilibrium Boundary Layers," Journal of Fluid Mechanics, Vol. 65, No. 2, pp. 261-287, 1974.

Peterson, A.P.G., and Gross, E.E. Handbook of Noise Measurement, Seventh Edition, General Radio Company, Concord, MA., 1972.

Schetz, J.A., Foundations of Boundary Layer Theory, Prentice-Hall, Inc., Englewood Cliffs, N.J., 1984.

Schewe, G., "On the Structure and Resolution of Wall Pressure Fluctuations Associated with Turbulent Boundary Layer Flow," Publication submitted to Journal of Fluid Mechanics,Max-Planck-Institut für Strömungsforschung, Göttingen, August 1982.

Schlichting, H. Boundary Layer Theory, Seventh Edition, McGraw-Hill, New York, 1979.

Schloemer, H.H., "Effects of Pressure Gradients on Turbulent-Boundary-Layer Wall-Pressure Fluctuations," The Journal of the Acoustical Society of America, Vol. 42, No. 1, pp. 93-113, 1967.

Shiloh, K., Shivaprasad, B.G., and Simpson, R.L., "The Structure of a Separating Turbulent Boundary Layer. Part 3. Transverse Velocity Measurements," Journal of Fluid Mechanics, Vol. 113, pp. 75-90, 1981.

Simpson, R.L., Ghodbane, M., and McGrath, B.E., "An Experimental Study of Surface Pressure Fluctuations in a Separating Turbulent Boundary Layer." NASA CR-175410, Mar. 1984.

Simpson, R.L., Chew, Y.T., and Shivaprasad, B.G., "The Structure of a Separating Turbulent Boundary Layer. Part 1. Mean Flow and Reynolds Stresses," Journal of Fluid Mechanics, Vol. 113,pp. 23-51, 1981.

Simpson, R.L., Chew, Y.T., and Shivaprasad, B.G., "The Structure of a Separating Turbulent Boundary Layer. Part 2. Higher-Order Turbulence Results," Journal of Fluid Mechanics, Vol. 113,pp. 53-73, 1981.

Thomas, A.S.W., and Bull, M.K., "On the Rule of Wall-Pressure Fluctuations in Deterministic Motions in the Turbulent Boundary Layer," Journal of Fluid Mechanics, Vol. 128, pp. 283- 322, 1983.

White, F.M., "A Unified Theory of Turbulent Wall Pressure Fluctuations," USN Underwater Sound Lab, Rept. 629, pp. 1-27, 1964.

White, F.M.,Fluid Mechanics, McGraw-Hill, New York, 1979.

Willmarth, W.W., "Pressure Fluctuations Beneath Turbulent Boundary Layers," Annual Reviews of Fluid Mechanics, pp. 13-38, 1975.

Willmarth, W.W., and Roos, F.W., "Resolution and Structure of the Wall Pressure Field Beneath a Turbulent Boundary Layer," Journal of Fluid Mechanics, Vol. 22, p. 81, 1965.

FIGURES

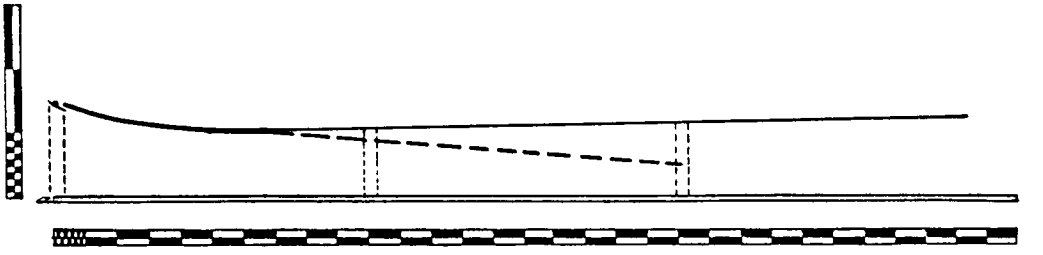

Figure 1. Side View of the Wind Tunnel Test Section: Solid line is the contour for dP/dx=0 flow and dashed line is the contour for dP/dx<0 flow. Major divisions shown by rule are 10 inches.

PRECEDING PAGE BLANK NOT FILMED

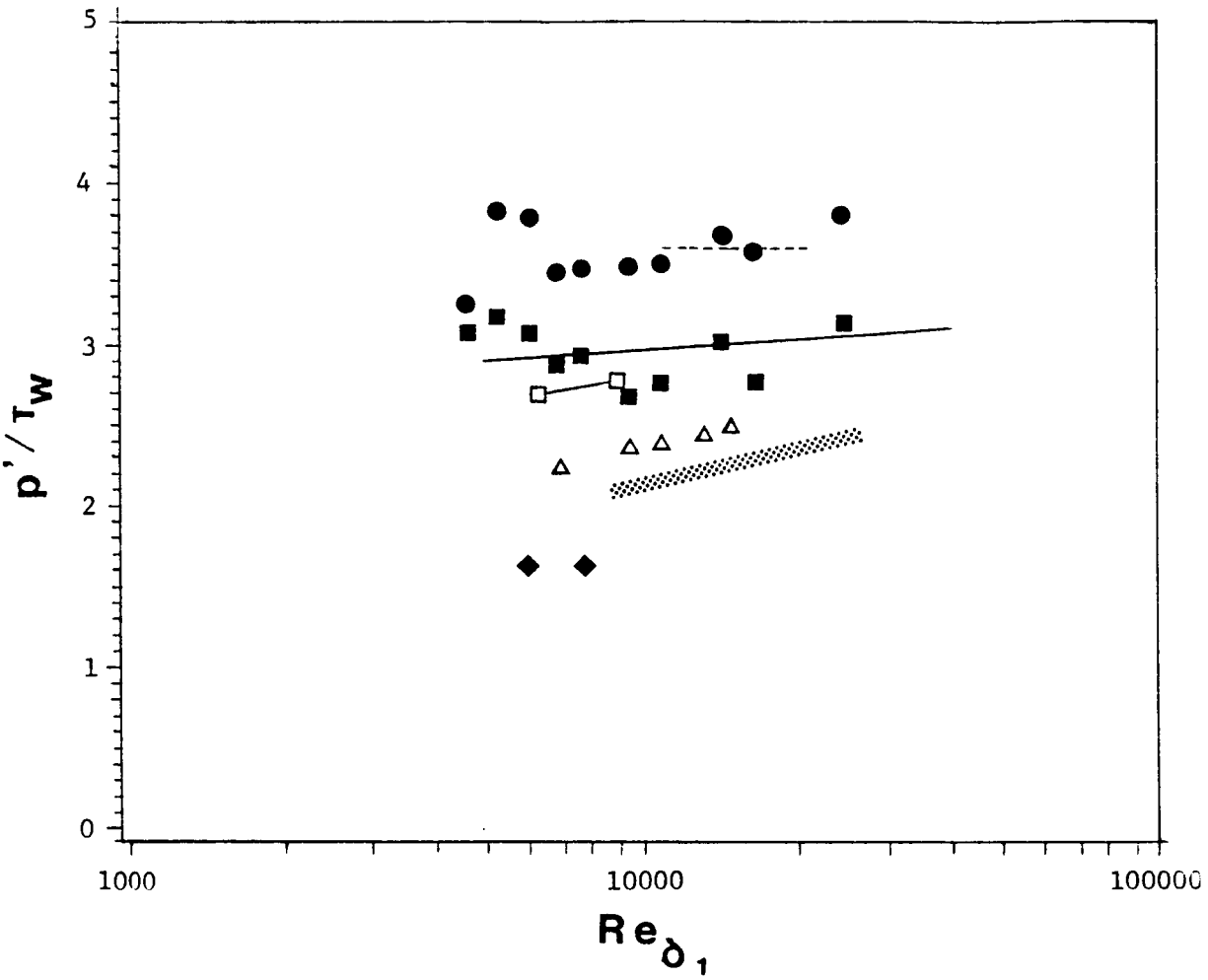

Figure 2. Zero Pressure Gradient Flow Results for p'/τ_w versus Re_{δ_1}: Solid line, Panton and Linebarger (1974) from equations (11) and (12); ● Schloemer (1967); ● Present Data model BT-1753; ■ Present Data model BT-1755; Dashed line, Blake (1970); Line with symbols, Bull and Thomas (1976); Lim (1971); Shaded region, Bull (1967) and Willmarth (1958).

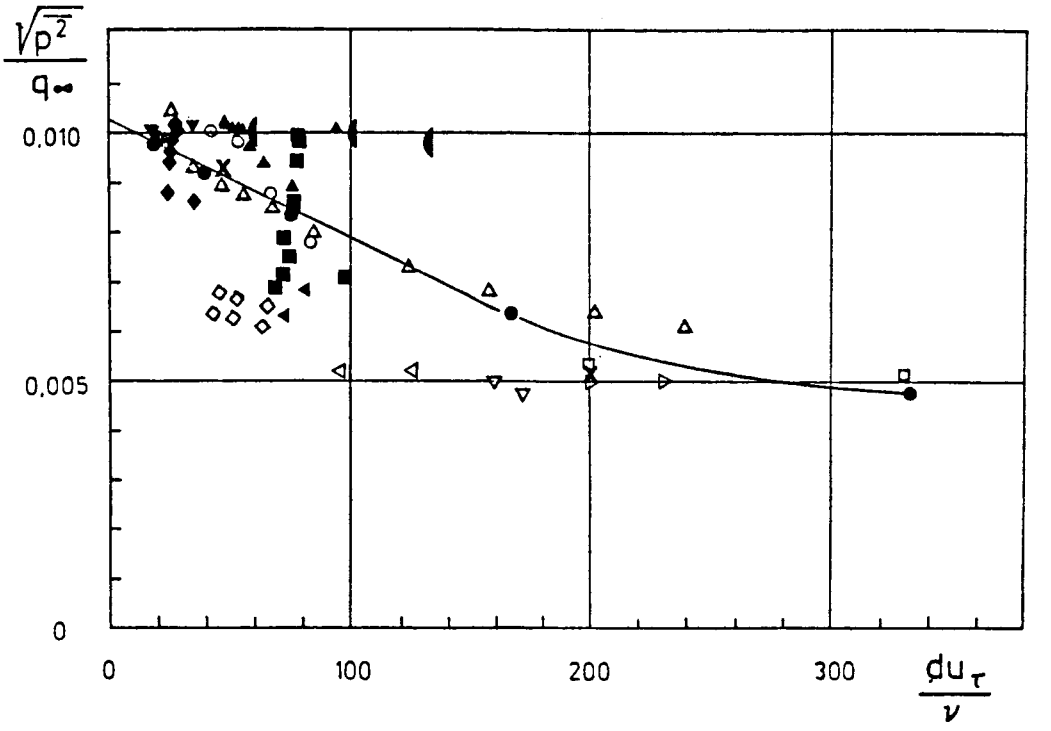

Figure 3. p'/q_∞ versus dU_τ/ν for the Zero and Favorable Pressure Gradient Flows: □ Willmarth and Roos (1965) dP/dx=0; ▽ Bull (1967) dP/dx<0; × Emmerling (1972) dP/dx<0; ◇ Bull and Thomas (1976) dP/dx=0; △ Langeheineken and Dinklelacker (1982) dP/dx<0; ● Schewe (1982) dP/dx<0; ▷ Schloemer (1967) dP/dx<0; ◁ Schloemer (1967) dP/dx=0; ○ Blake (1970) dP/dx=0; ◀ Lim (1971) dP/dx=0; ◖ Burton (1973) dP/dx<0; ◆ Present Data model BT-1753 dP/dx=0; ■ Present Data model BT-1755 dP/dx=0; ▼ Present Data model BT-1753 dP/dx<0; ▲ Present Data model BT-1755 dP/dx<0.

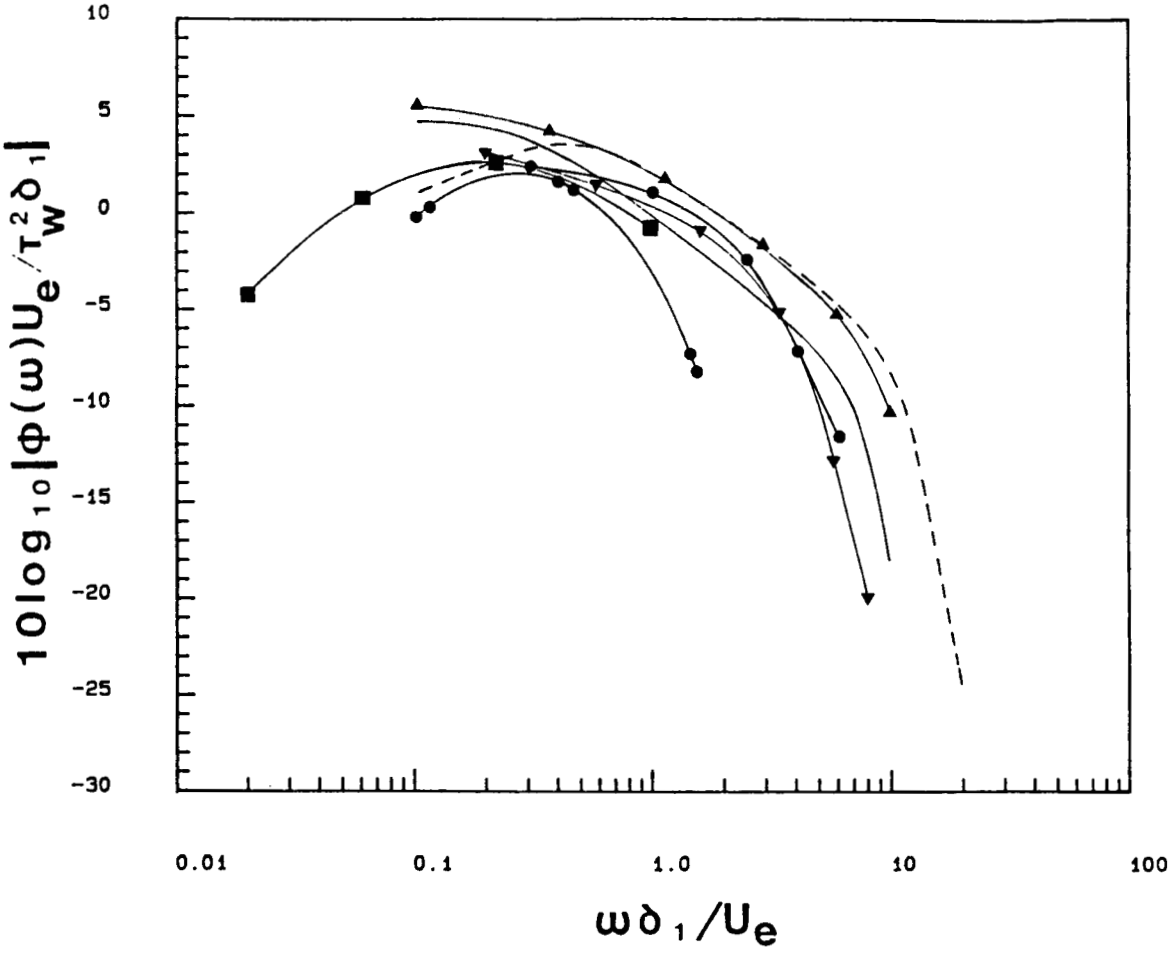

Figure 4. Mean Curves of the Nondimensional Pressure Spectra for Several Researchers in Both Zero and Favorable Pressure Gradients: Solid line, Burton (1973) dP/dx=0; Dashed line, Blake (1970) dP/dx=0; —●— Schloemer (1967) dP/dx=0; —▲— Present Data, model BT-1753 dP/dx=0; —●●— Schloemer (1967) dP/dx<0; —■— Burton (1973) dP/dx<0; —▼— Present Data, model BT-1753 dP/dx<0.

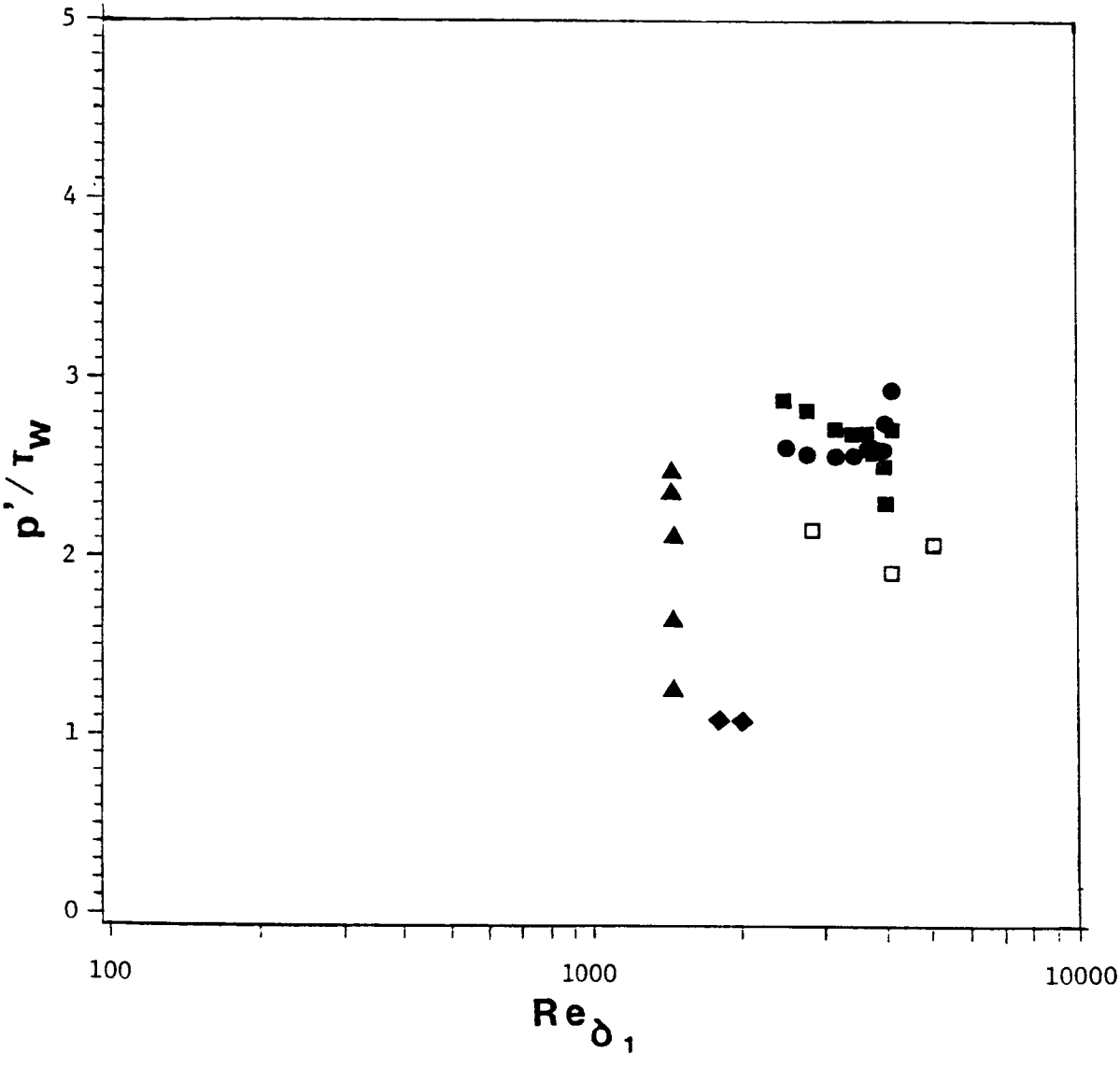

Figure 5. Favorable Pressure Gradient Flow Results for p'/τ_w versus Re_{δ_1}: ● Schloemer (1967); □ Burton (1973); ▲ Schewe (1982), for five different values of d^+; ● Present Data model BT-1753; ■ Present Data model BT-1755.

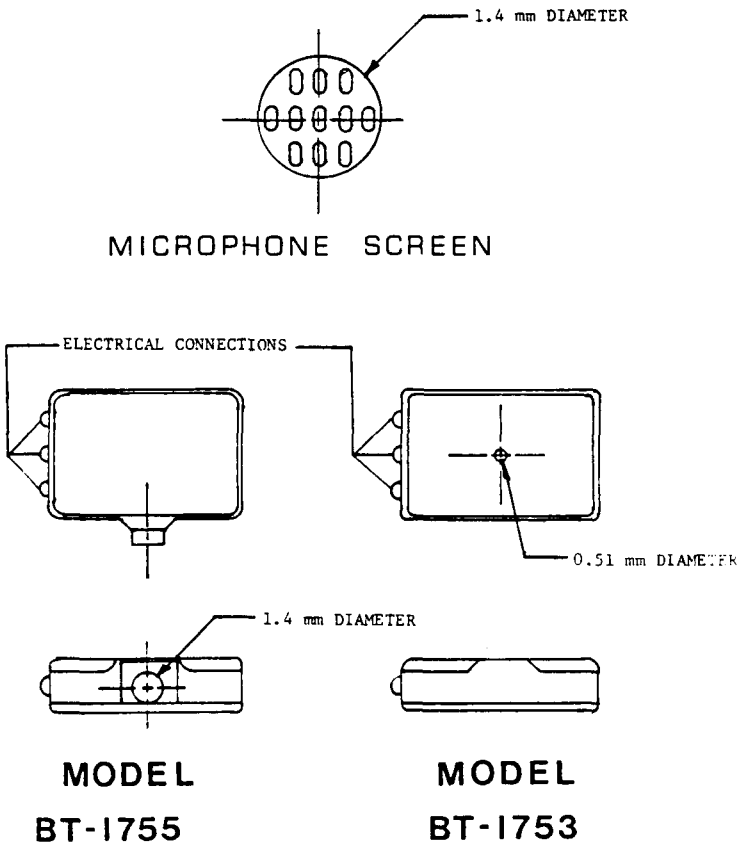

Figure 6. Schematic of the Endevco Microphone Screen and Knowles Electronics Microphones.

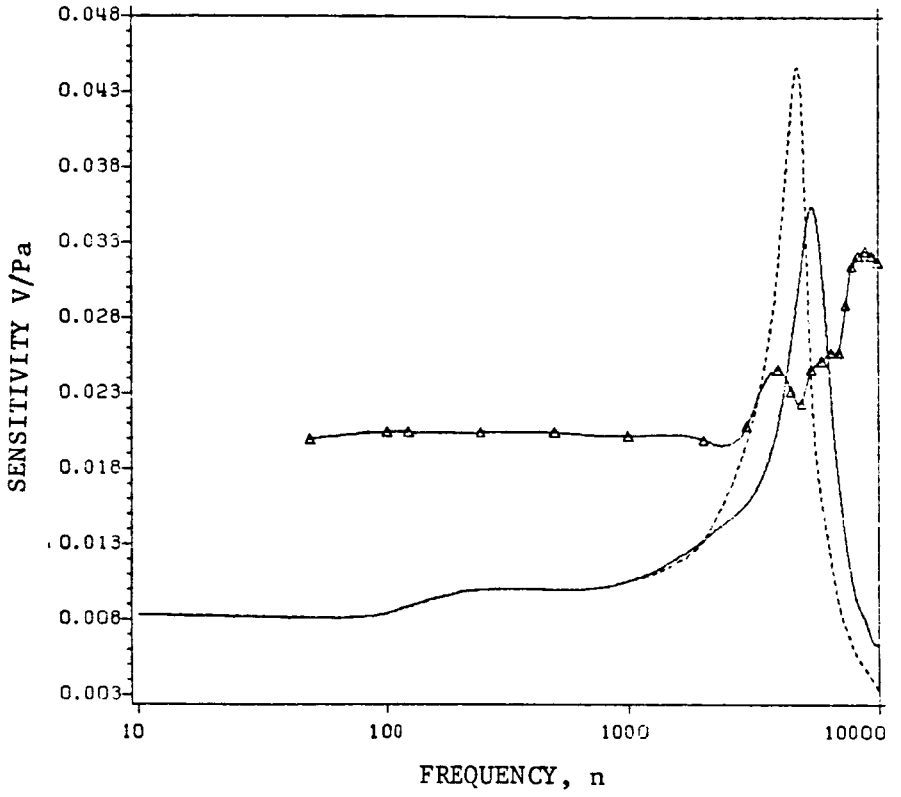

Figure 7. Microphone Sensitivity (V/Pa) versus Frequency (n): The solid line is for microphone model BT-1753, the dashed line is for microphone model BT-1755 and the solid line with symbols is for the Sennheiser model microphone supplied by the manufacturer.

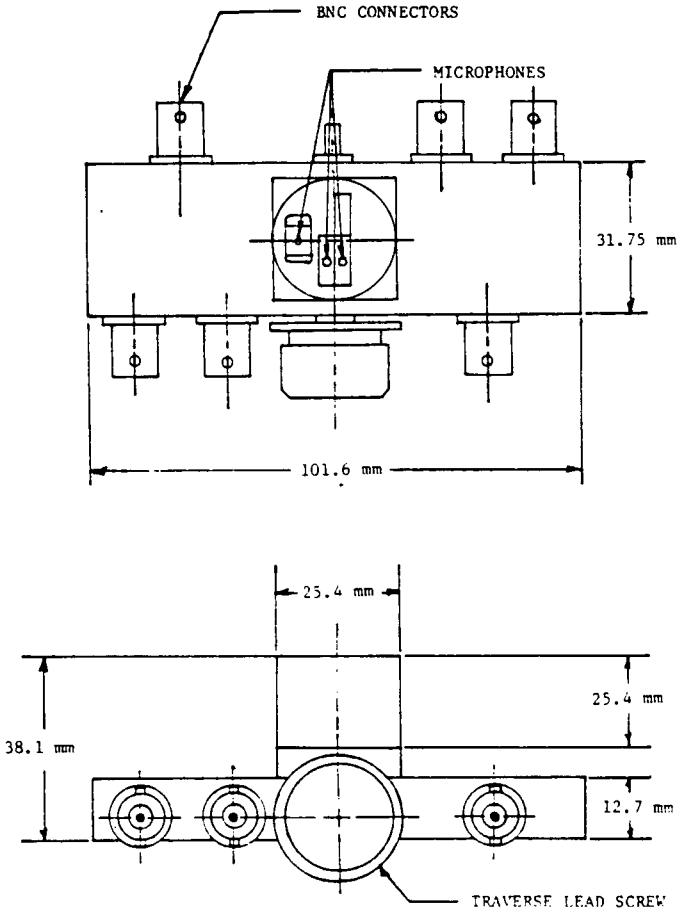

Figure 8. Schematic of the Microphone Housing Unit: Note that two BT-1755 and one BT-1753 microphones are in each unit.

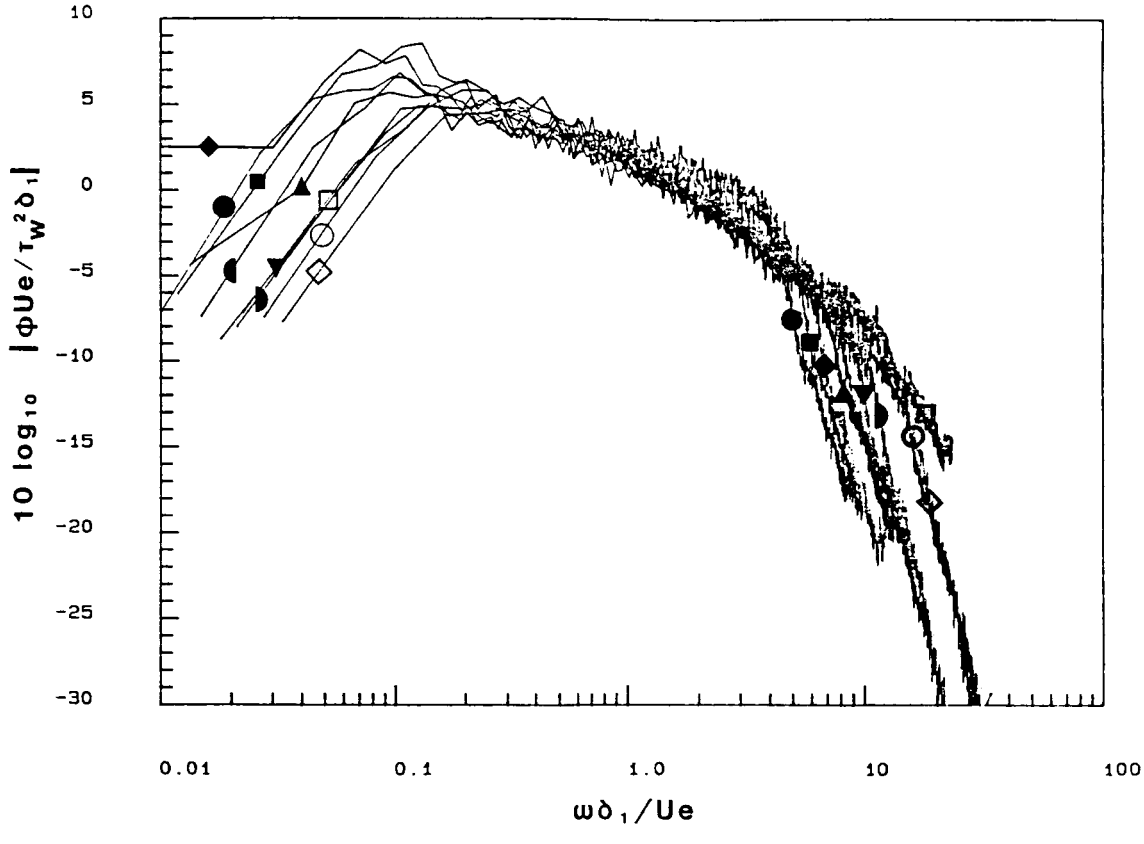

Figure 9. Nondimensional Pressure Spectra Normalized on δ_1, U_e and the wall shear stress, τ_w, the Outer Variables for the Zero Pressure Gradient Flow: Results for BT-1753 at the following x-locations, ● 1.63 m; ◆ 1.88 m; ■ 2.22 m; ▲ 2.54 m; ◖ 2.86 m; ▼ 3.52 m; ◗ 4.14 m; ○ 5.48 m; ◇ 6.51 m; □ 6.51 m (q=2.4"H_2O).

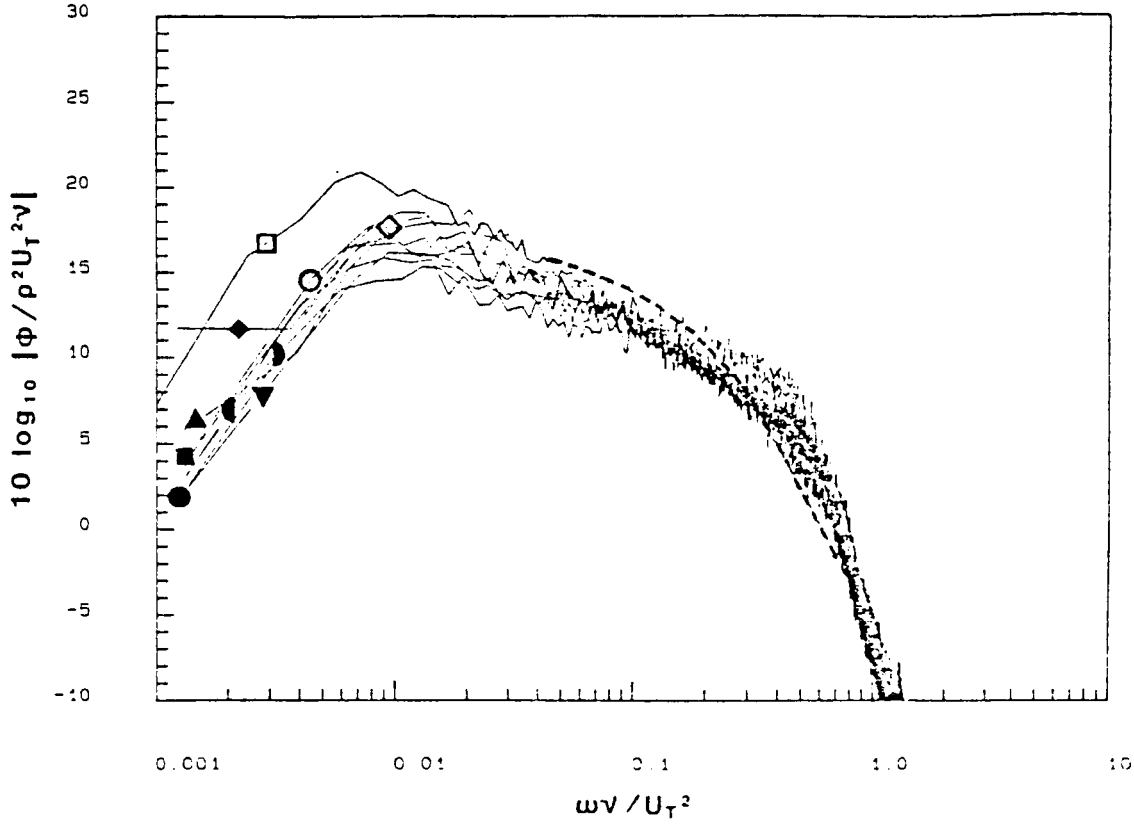

Figure 10. Nondimensional Pressure Spectra Normalized on ν and U_τ, the Inner Variables for the Zero Pressure Gradient Flow: Results for BT-1753 at the following x-locations, ● 1.63 m; ⬢ 1.88 m; ■ 2.22 m; ▲ 2.54 m; ◖ 2.86 m; ▼ 3.52 m; ◗ 4.14 m; ○ 5.48 m; ◇ 6.51 m; □ 6.51 m(q=2.4"H_2O); Dashed line, Bull and Thomas (1976).

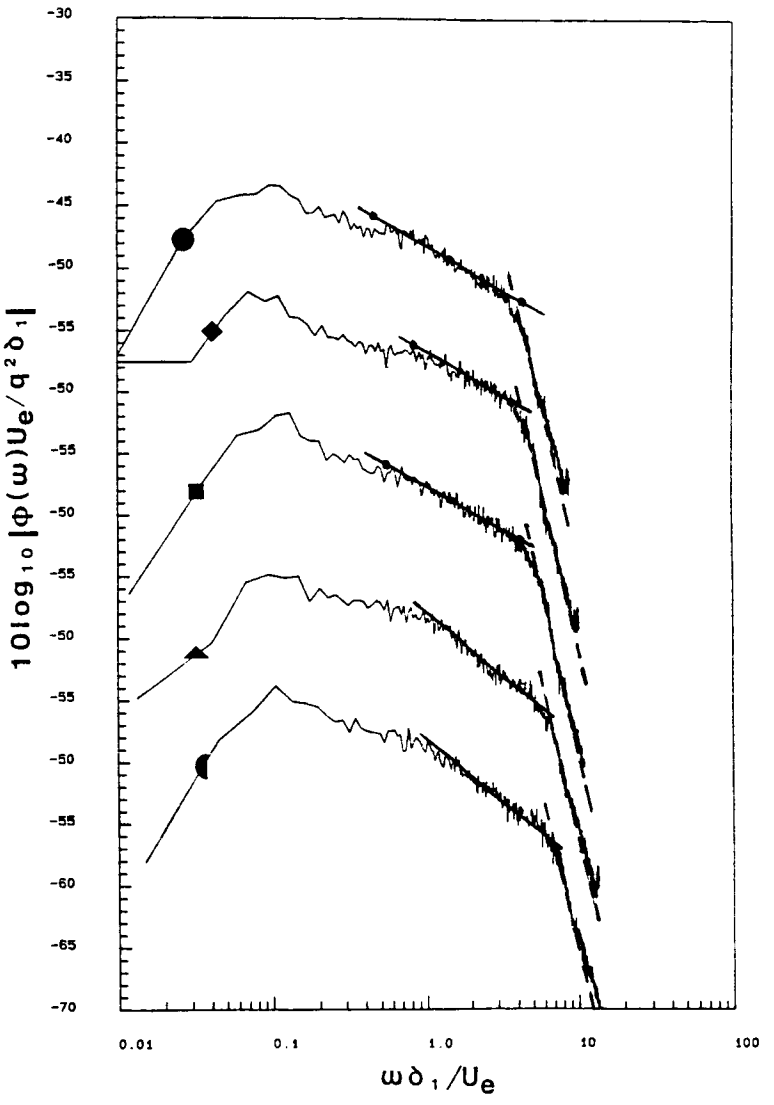

Figure 11. Nondimensional Pressure Spectra Normalized on δ_1, U_e and q_e, the Outer Variables for the Zero Pressure Gradient Flow: Results for BT-1753 at the following x-locations, ● 1.63 m; ◆ 1.88 m; ■ 2.22 m; ▲ 2.54 m; ◖ 2.86 m. The solid line is where the spectra varies like n^{-1}, the dashed line is a $n^{-5.5}$ variation, and the solid line with symbols is a $n^{-0.7}$ variation. Note the offset of each curve from top to bottom of 10 dB.

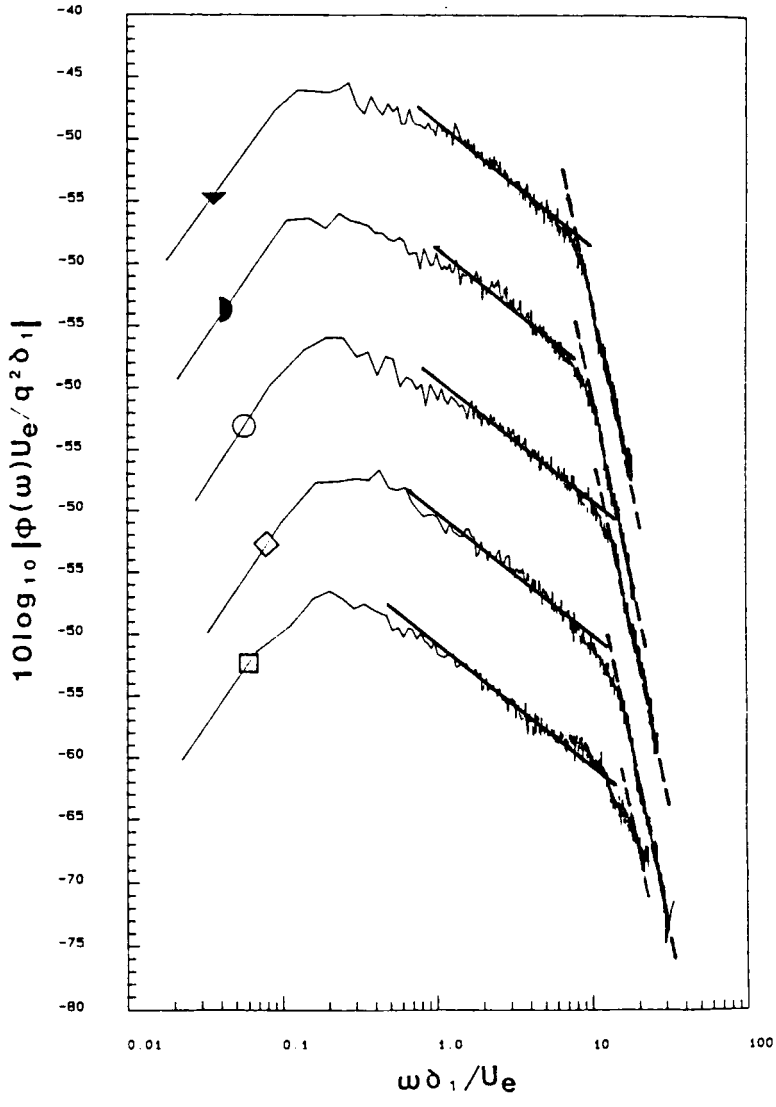

Figure 12. Nondimensional Pressure Spectra Normalized on δ_1, U_e and q_e, the Outer Variables for the Zero Pressure Gradient Flow: Results for BT-1753 at the following x-locations, ▼ 3.52 m; ◗ 4.14 m; ○ 5.48 m; ◇ 6.51 m; □ 6.51 m ($q=2.4"H_2O$). The solid line is where the spectra varies like n^{-1}, and the dashed line is a $n^{-5.5}$ variation. Note the offset of each curve from top to bottom of 10 dB.

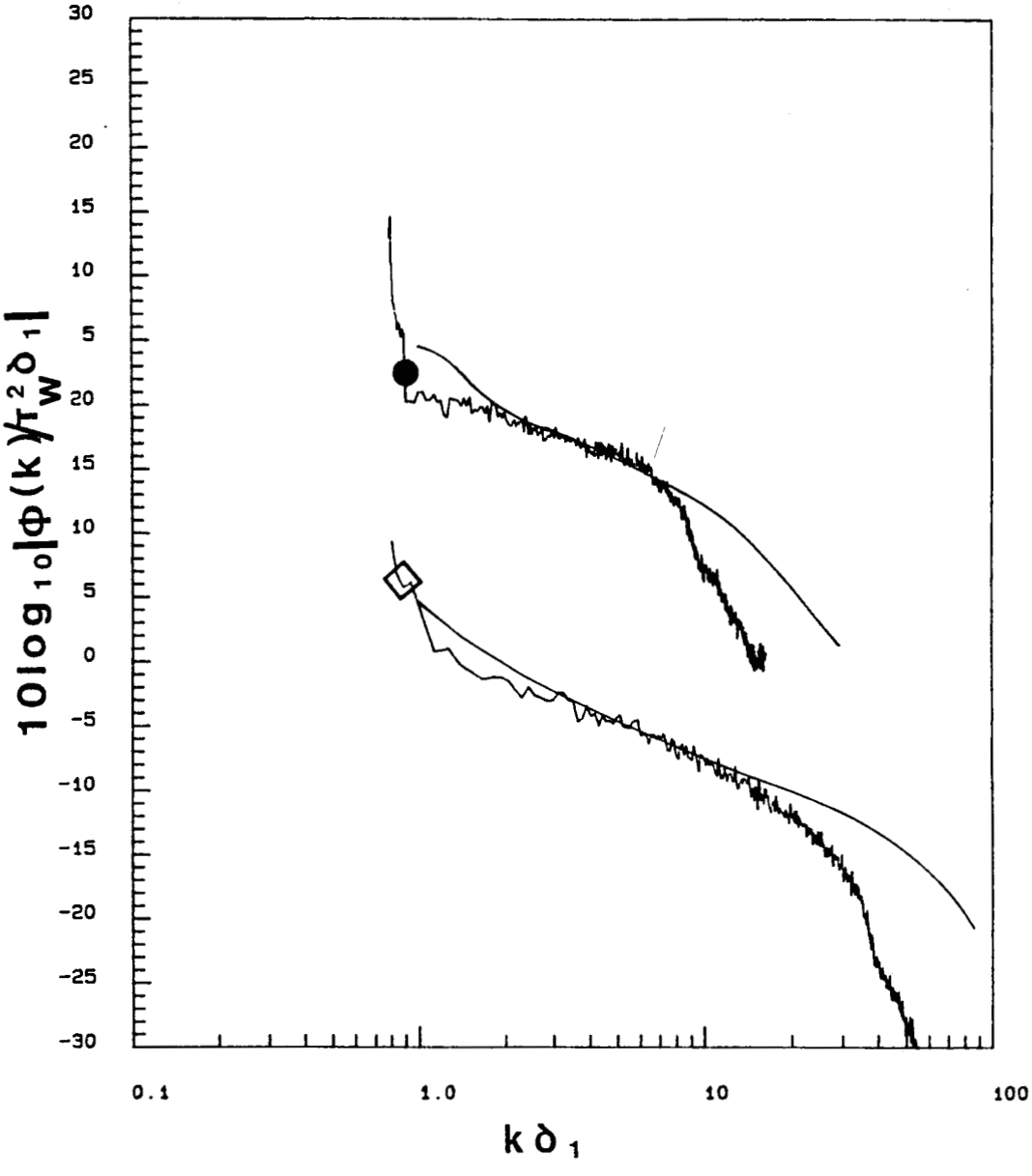

Figure 13. Nondimensional Pressure Spectra as a function of Wavenumber for the Zero Pressure Gradient Flow: Results for BT-1753, ● 1.63 m, $U_\tau\delta/\nu$=1350 and for Panton and Linebarger $U_\tau\delta/\nu$=1000;
◇ 6.51 m, $U_\tau\delta/\nu$=3876 and for Panton and Linebarger $U_\tau\delta/\nu$=4000.

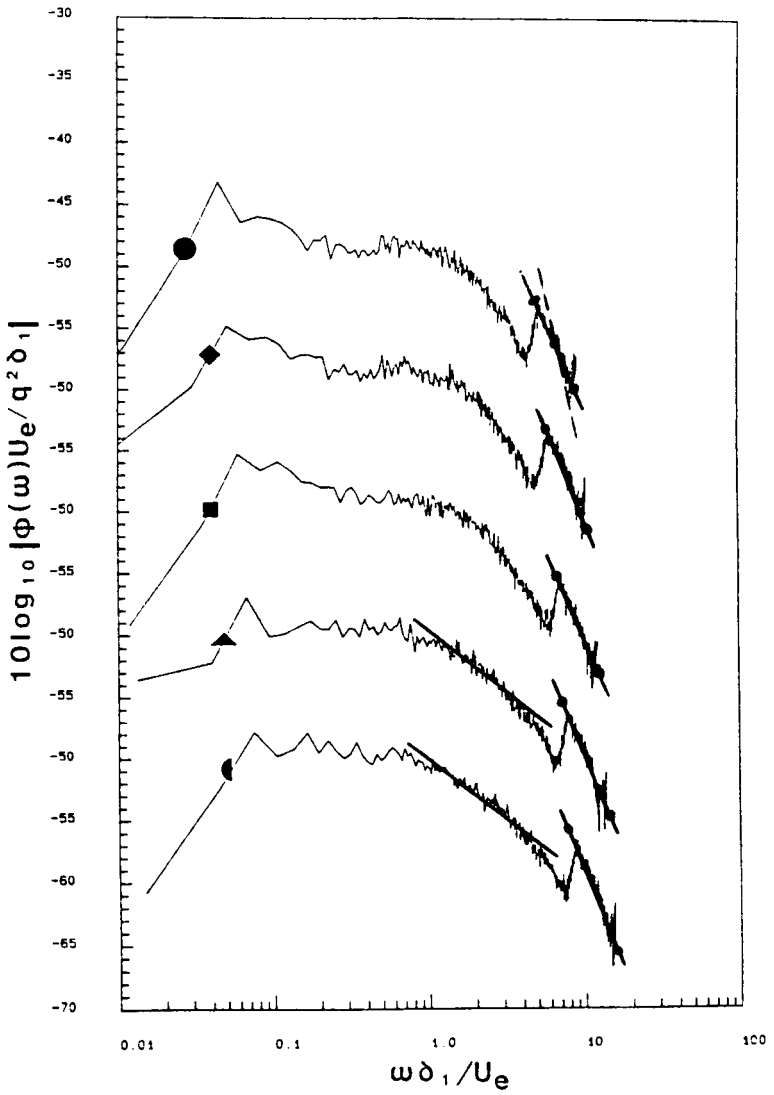

Figure 14. Nondimensional Pressure Spectra Normalized on δ_1, U_e and q_e, the Outer Variables for the Zero Pressure Gradient Flow: Results for BT-1755 at the following x-locations, ● 1.63 m; ◆ 1.88 m; ■ 2.22 m; ▲ 2.54 m; ◖ 2.86 m. The solid line is where the spectra varies like n^{-1}, the dashed line is a $n^{-5.5}$ variation, and the solid line with symbols is a n^{-3} variation. Note the offset of each curve from top to bottom of 10 dB.

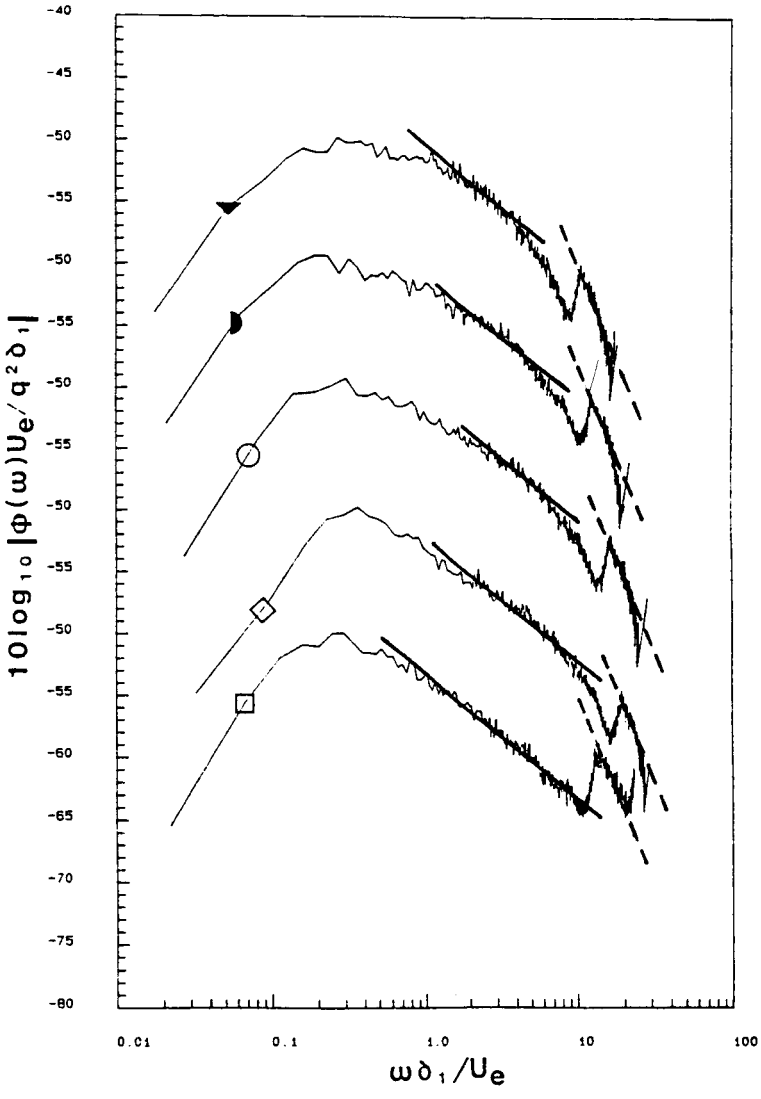

Figure 15. Nondimensional Pressure Spectra Normalized on δ_1, U_e and q_e, the Outer Variables for the Zero Pressure Gradient Flow: Results for BT-1755 at the following x-locations, ▼ 3.52 m; ◗ 4.14 m; O 5.48 m; ◇ 6.51 m; □ 6.51 m ($q=2.4"H_2O$). The solid line is where the spectra varies like n^{-1} and the dashed line is a n^{-3} variation. Note the offset of each curve from top to bottom of 10 dB.

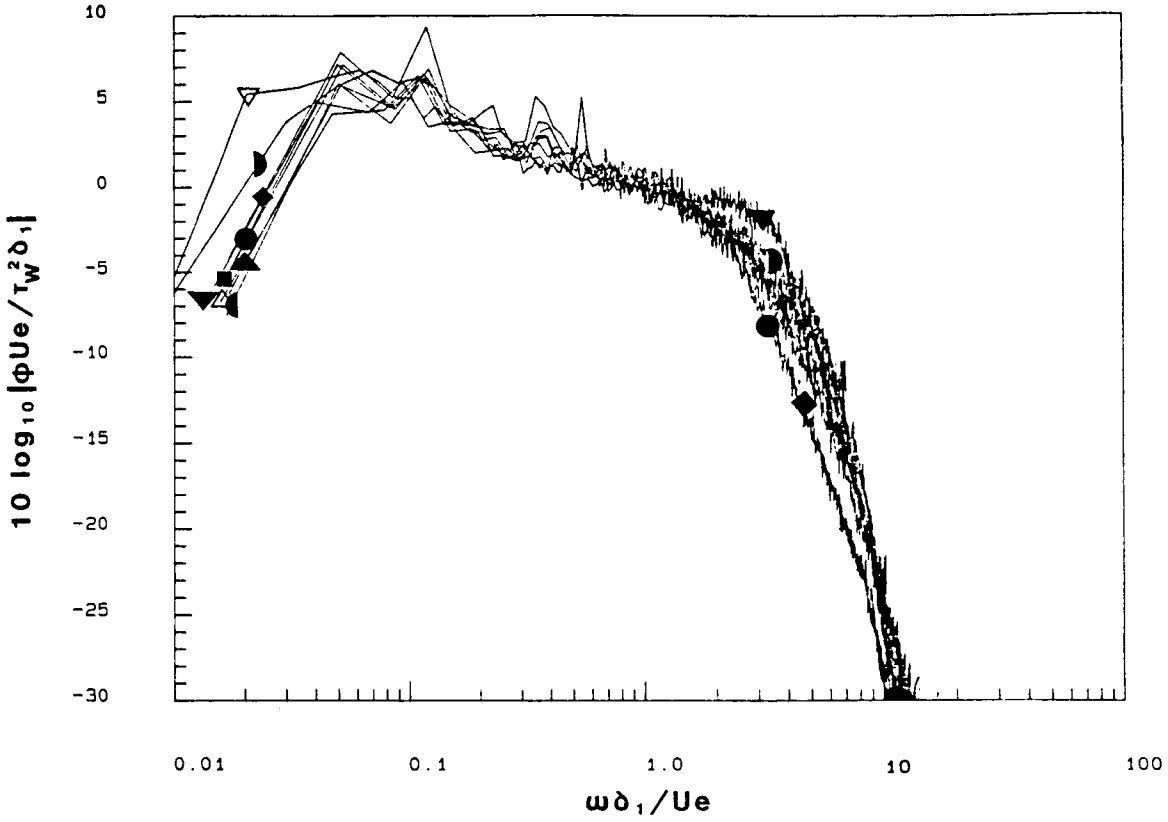

Figure 16. Nondimensional Pressure Spectra Normalized on δ_1, U_e and the wall shear stress, τ_w, the Outer Variables for the Favorable Pressure Gradient Flow: Results for BT-1753 at the following x-locations, ● 1.63 m; ◆ 1.88 m; ■ 2.22 m; ▲ 2.54 m; ◖ 2.86 m; △ 3.12 m; ▼ 3.52 m; ◗ 4.14 m; ▽ 4.77 m.

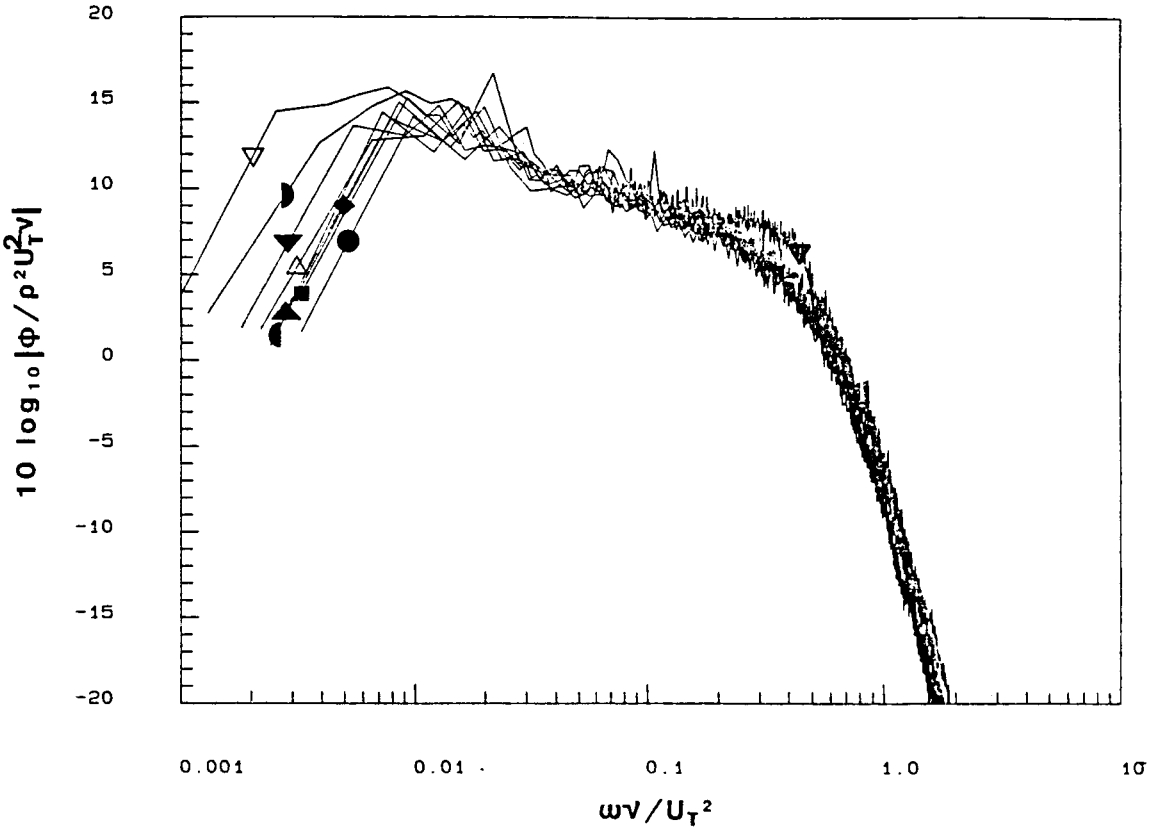

Figure 17. Nondimensional Pressure Spectra Normalized on ν and U_τ, the Inner Variables for the Favorable Pressure Gradient Flow: Results for BT-1753 at the following x-locations, ● 1.63 m; ● 1.88 m; ■ 2.22 m; ▲ 2.54 m; ◖ 2.86 m; △ 3.12 m; ▼ 3.52 m; ◗ 4.14 m; ▽ 4.77 m.

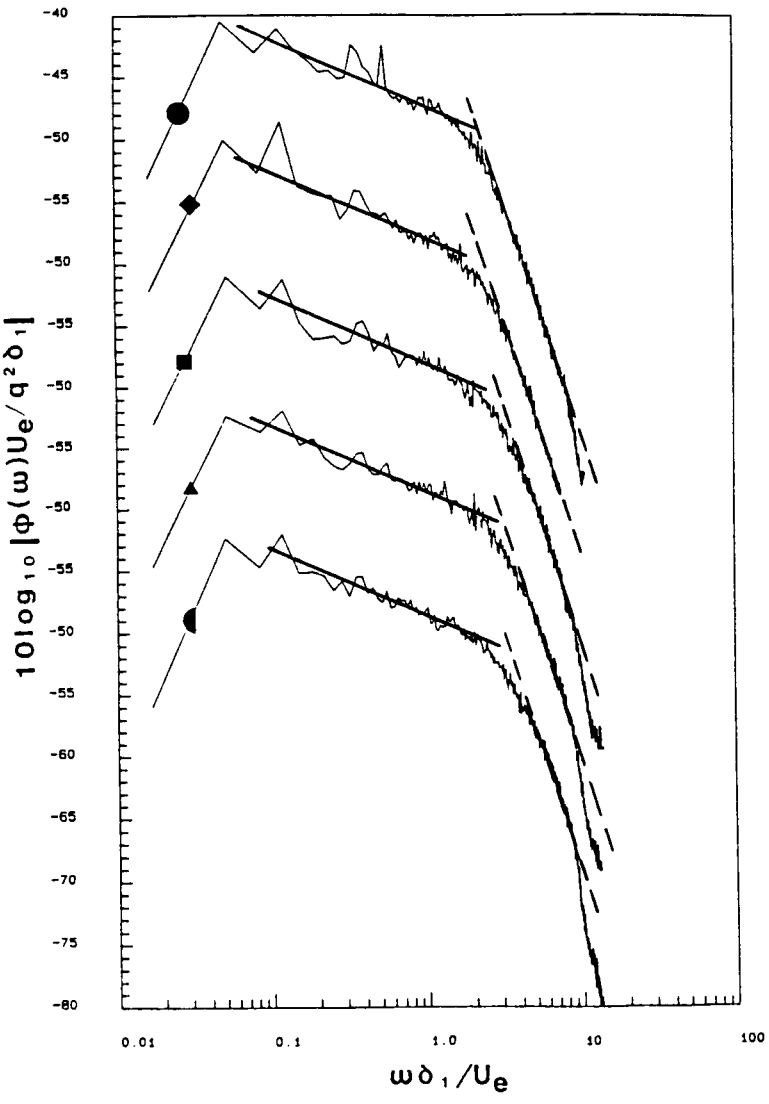

Figure 18. Nondimensional Pressure Spectra Normalized on δ_1, U_e and q_e, the Outer Variables for the Favorable Pressure Gradient Flow: Results for BT-1753 at the following x-locations, ● 1.63 m; ◆ 1.88 m; ■ 2.22 m; ▲ 2.54 m; ◖ 2.86 m. The solid line is where the spectra varies like $n^{-0.7}$, and the dashed line is a n^{-5} variation. Note the offset on each curve from top to bottom of 10 dB.

C-2

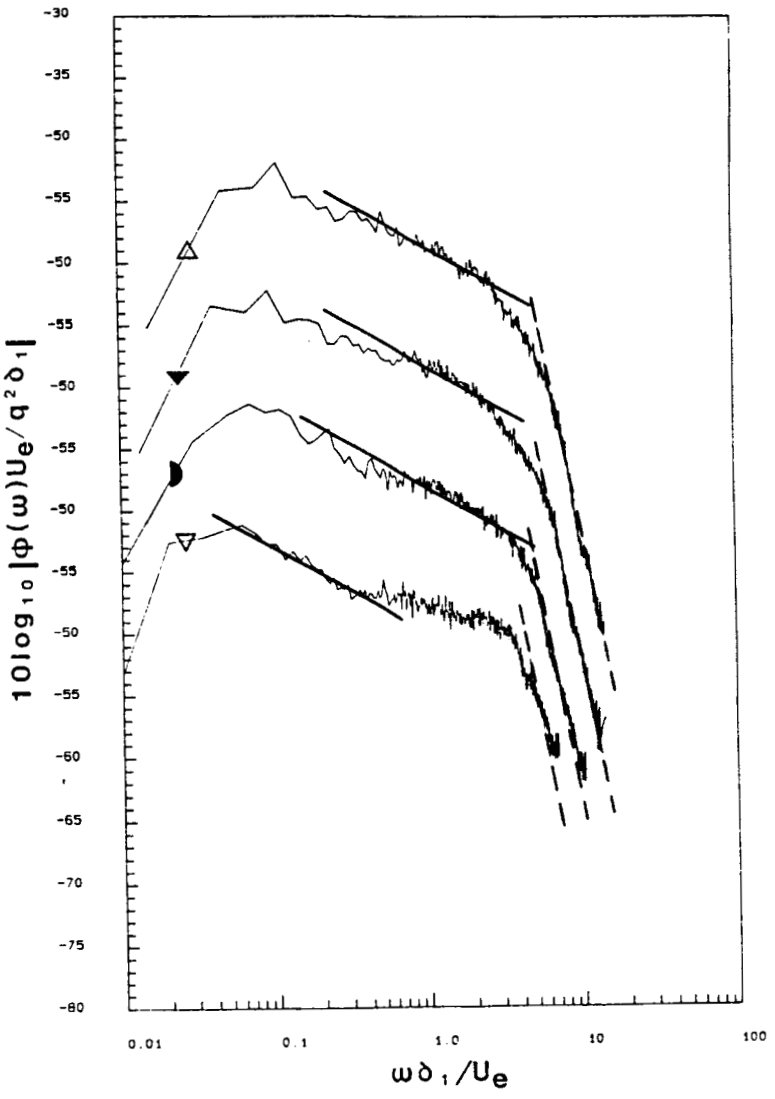

Figure 19. Nondimensional Pressure Spectra Normalized on δ_1, U_e and q_e, the Outer Variables for the Favorable Pressure Gradient Flow: Results for BT-1753 at the following x-locations, △ 3.12 m; ▼ 3.52 m; ◗ 4.14 m; ▽ 4.77 m. The solid line is where the spectra varies like $n^{-0.7}$, and the dashed line is a n^{-6} variation. Note the offset on each curve from top to bottom of 10 dB.

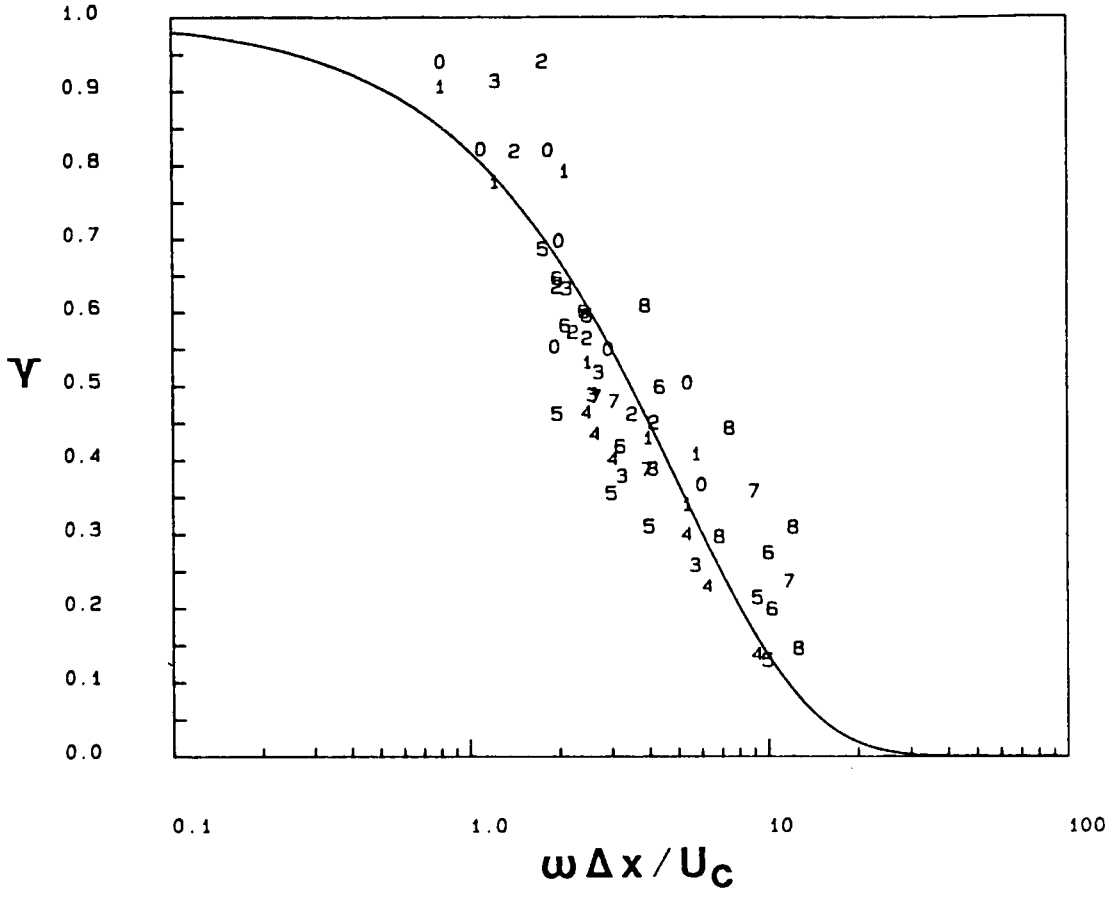

Figure 20. Longitudinal γ for the Zero Pressure Gradient Flow, x=1.63 m: Solid line is the exponential decay with K_1=0.2.

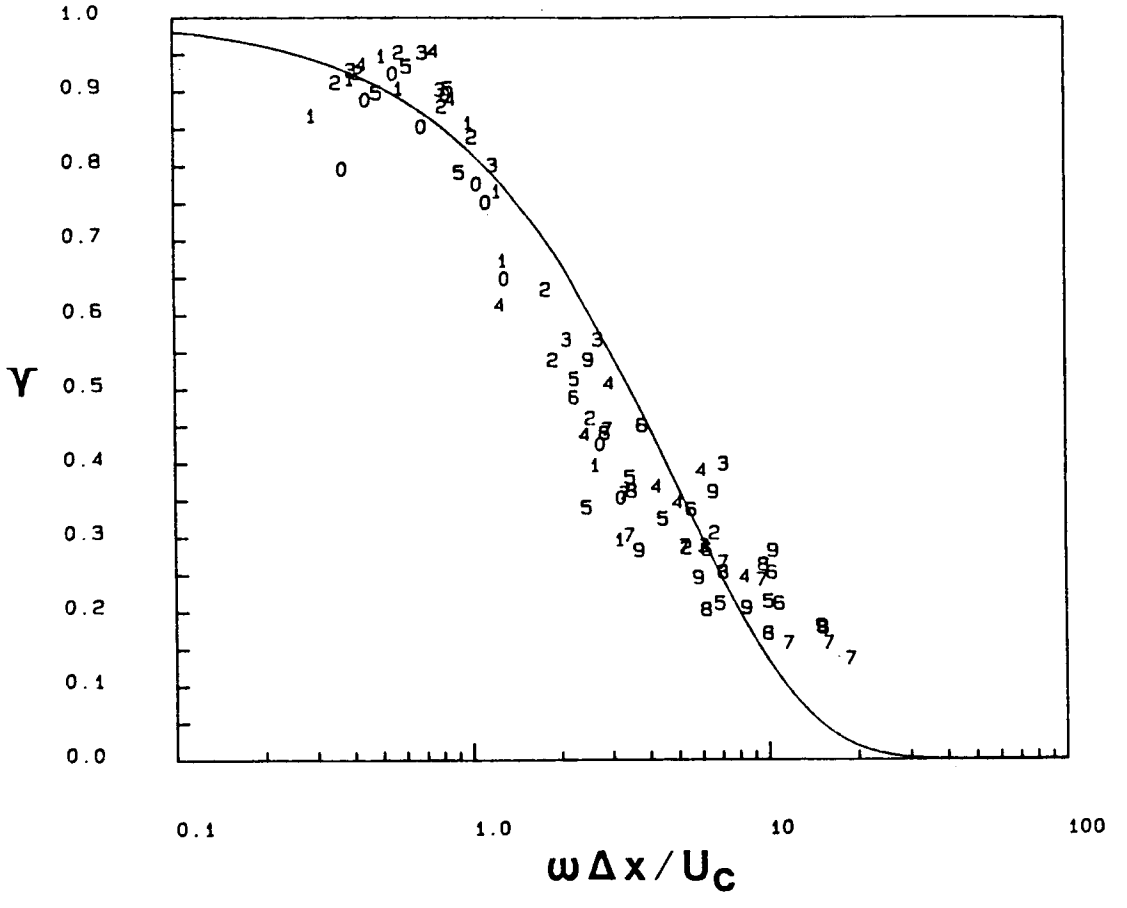

Figure 21. Longitudinal γ for the Zero Pressure Gradient Flow, x=3.52 m: Solid line is the exponential decay with K_1=0.2.

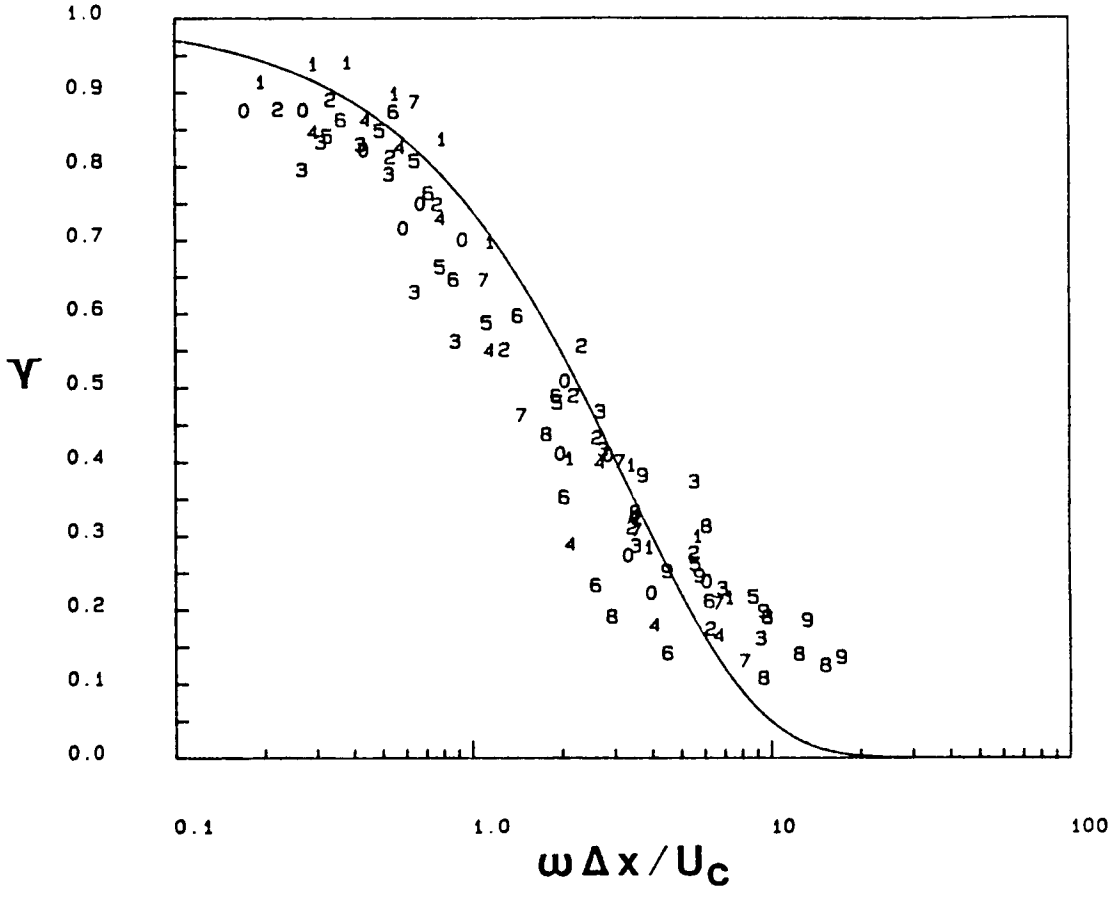

Figure 22. Longitudinal γ for the Zero Pressure Gradient Flow, x=4.14 m: Solid line is the exponential decay with K_1=0.3.

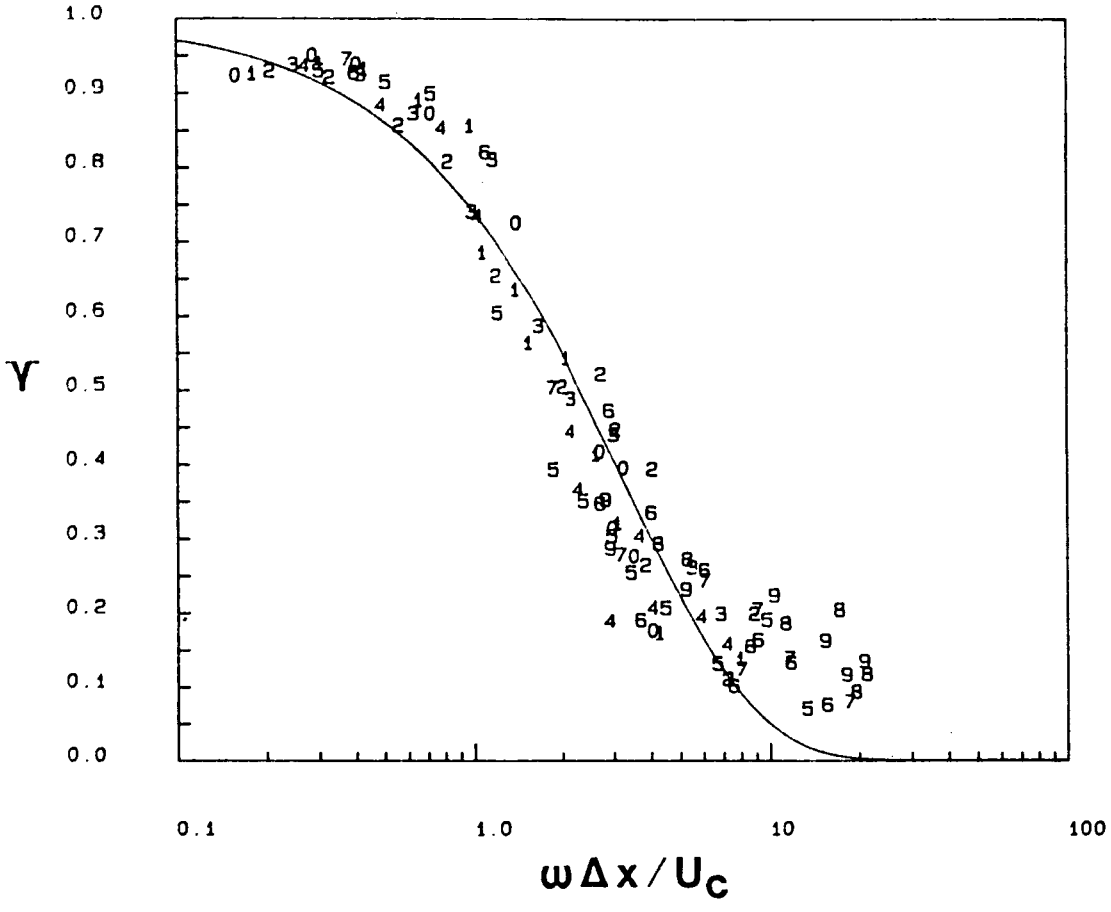

Figure 23. Longitudinal γ for the Zero Pressure Gradient Flow, x=6.51 m: Solid line is the exponential with K_1=0.3.

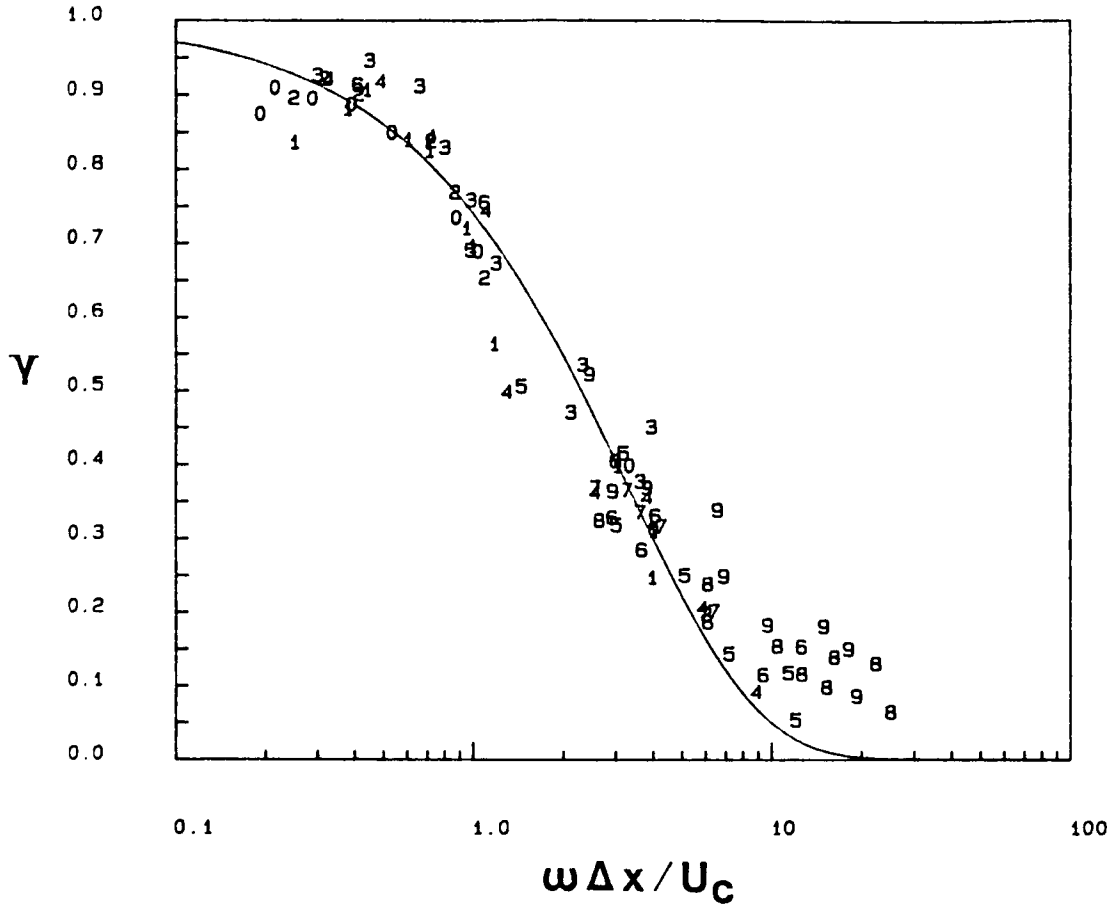

Figure 24. Longitudinal γ for the Zero Pressure Gradient Flow, x=6.51 m (q=2.4"H_2O): Solid line is the exponential with K_1=0.3.

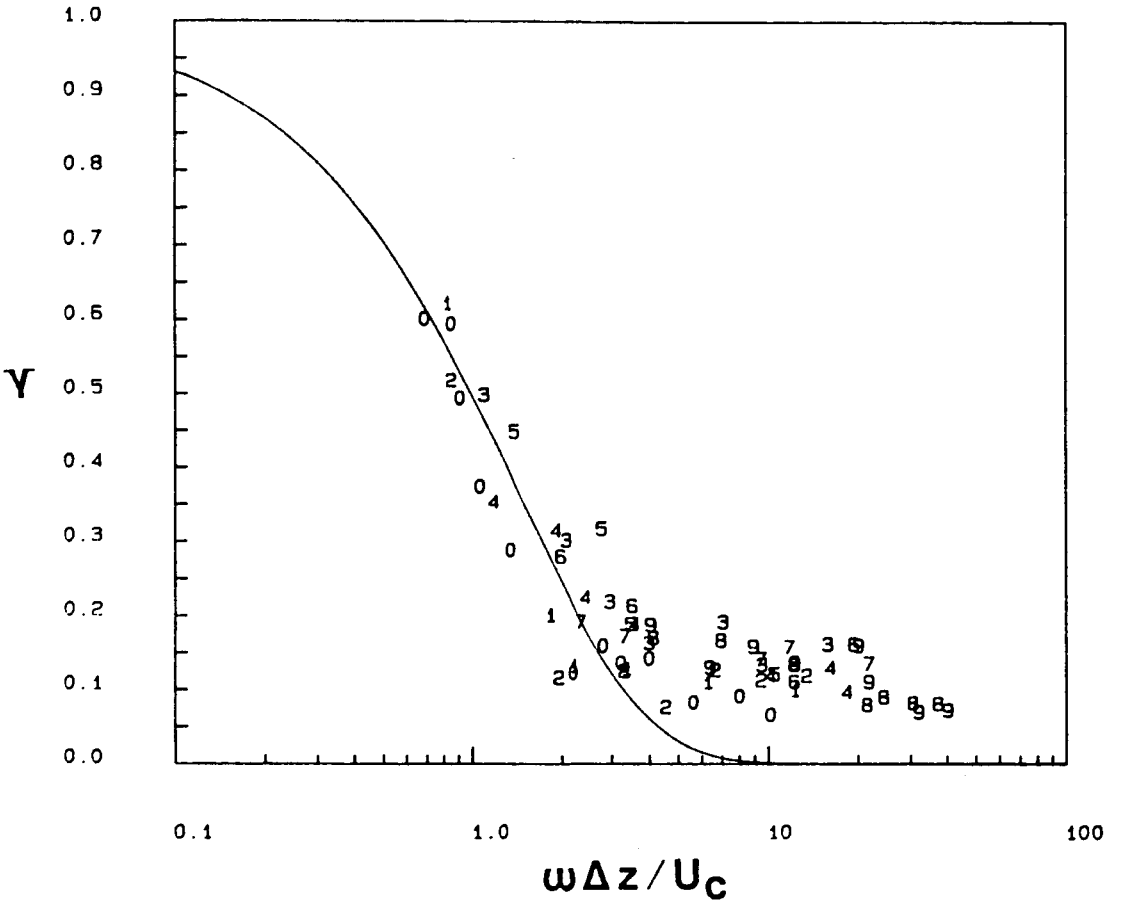

Figure 25. Lateral γ for the Zero Pressure Gradient Flow, x=1.63 m: Solid line is the exponential decay with K_3=0.7.

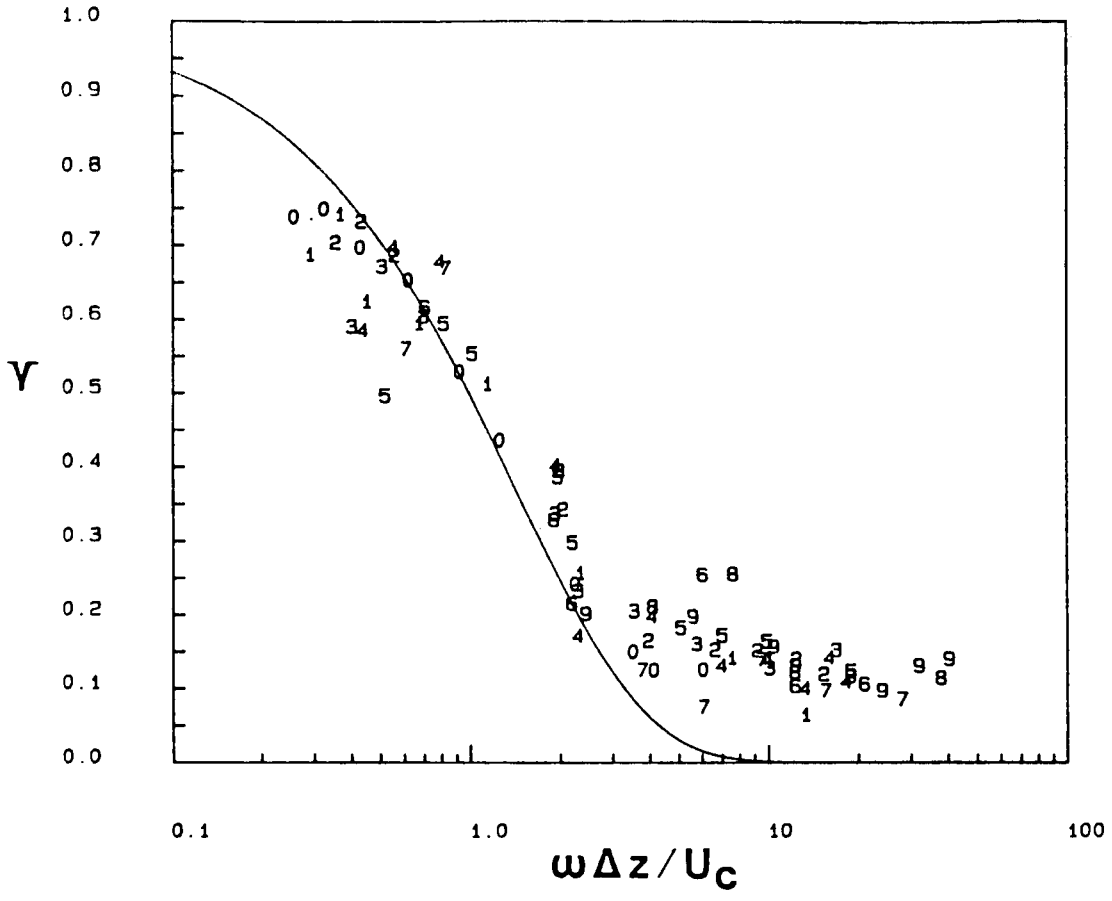

Figure 26. Lateral γ for the Zero Pressure Gradient Flow, x=3.52 m: Solid line is the exponential decay with K_3=0.7.

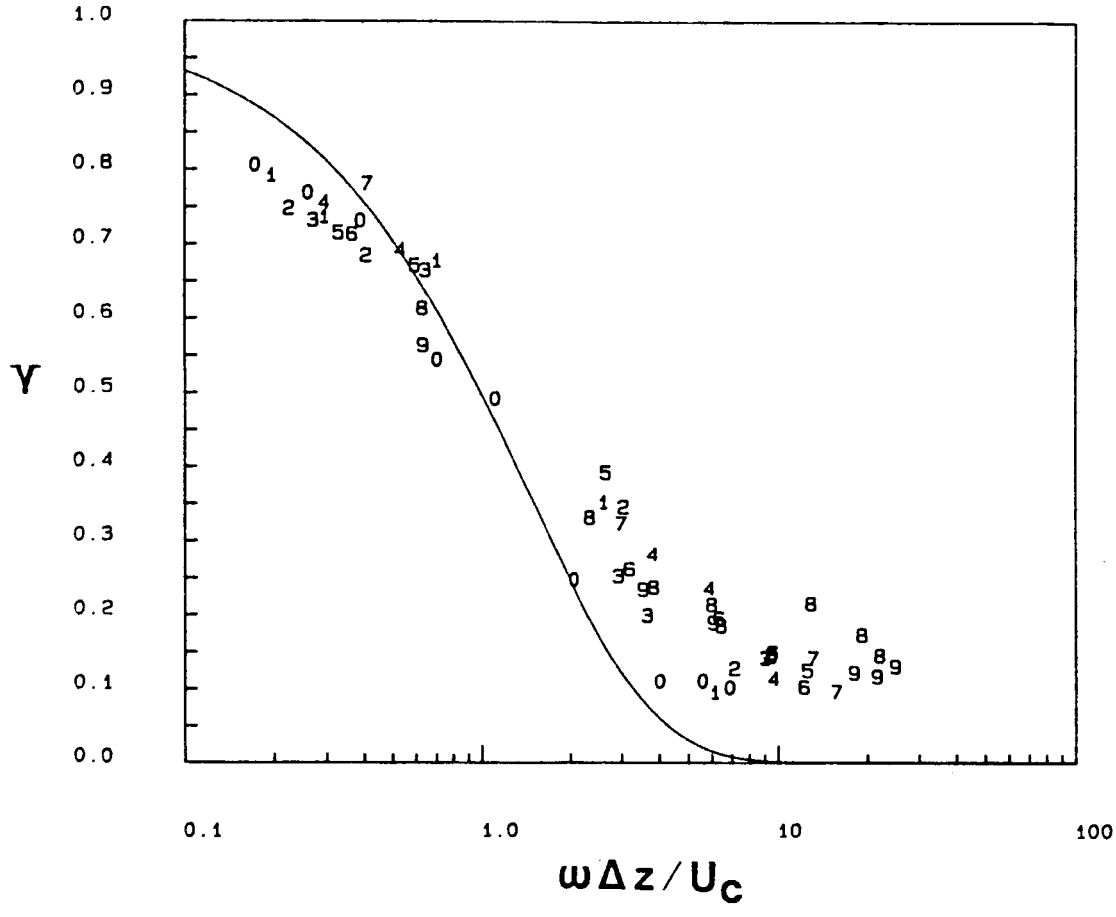

Figure 27. Lateral γ for the Zero Pressure Gradient Flow, x=4.14 m: Solid line is the exponential decay with K_3=0.7.

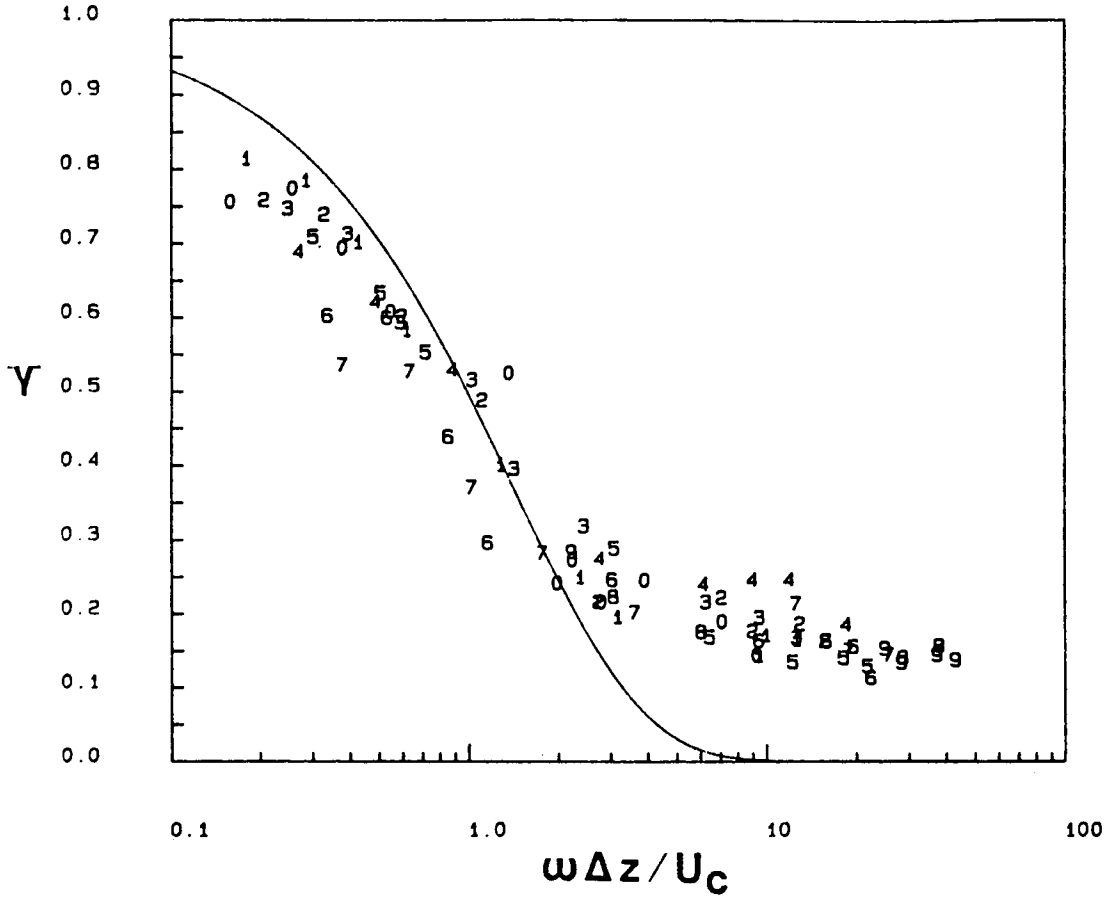

Figure 28. Lateral γ for the Zero Pressure Gradient Flow, x=6.51 m: Solid line is the exponential decay with K_3=0.7.

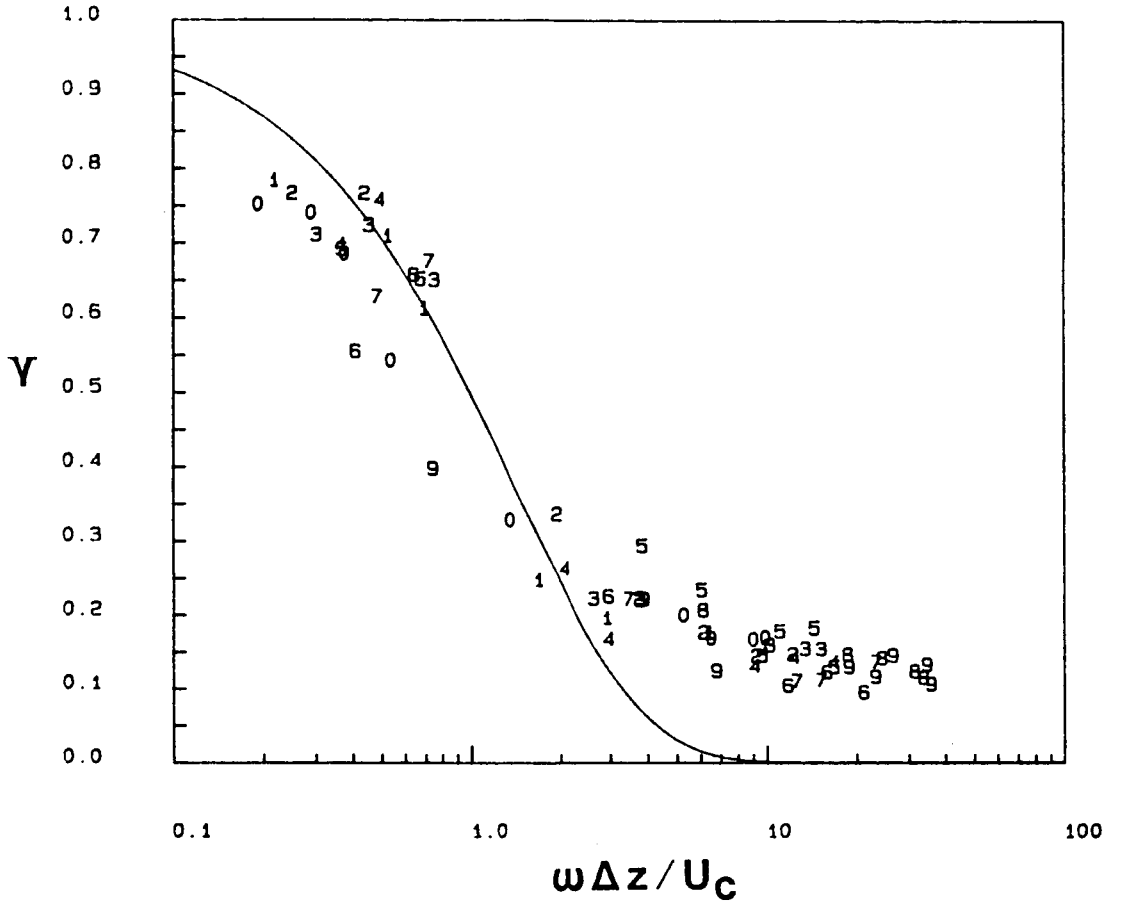

Figure 29. Lateral γ for the Zero Pressure Gradient Flow, x=6.51 m (q=2.4"H_2O), x=6.51: solid line is the exponential decay with K_3=0.7.

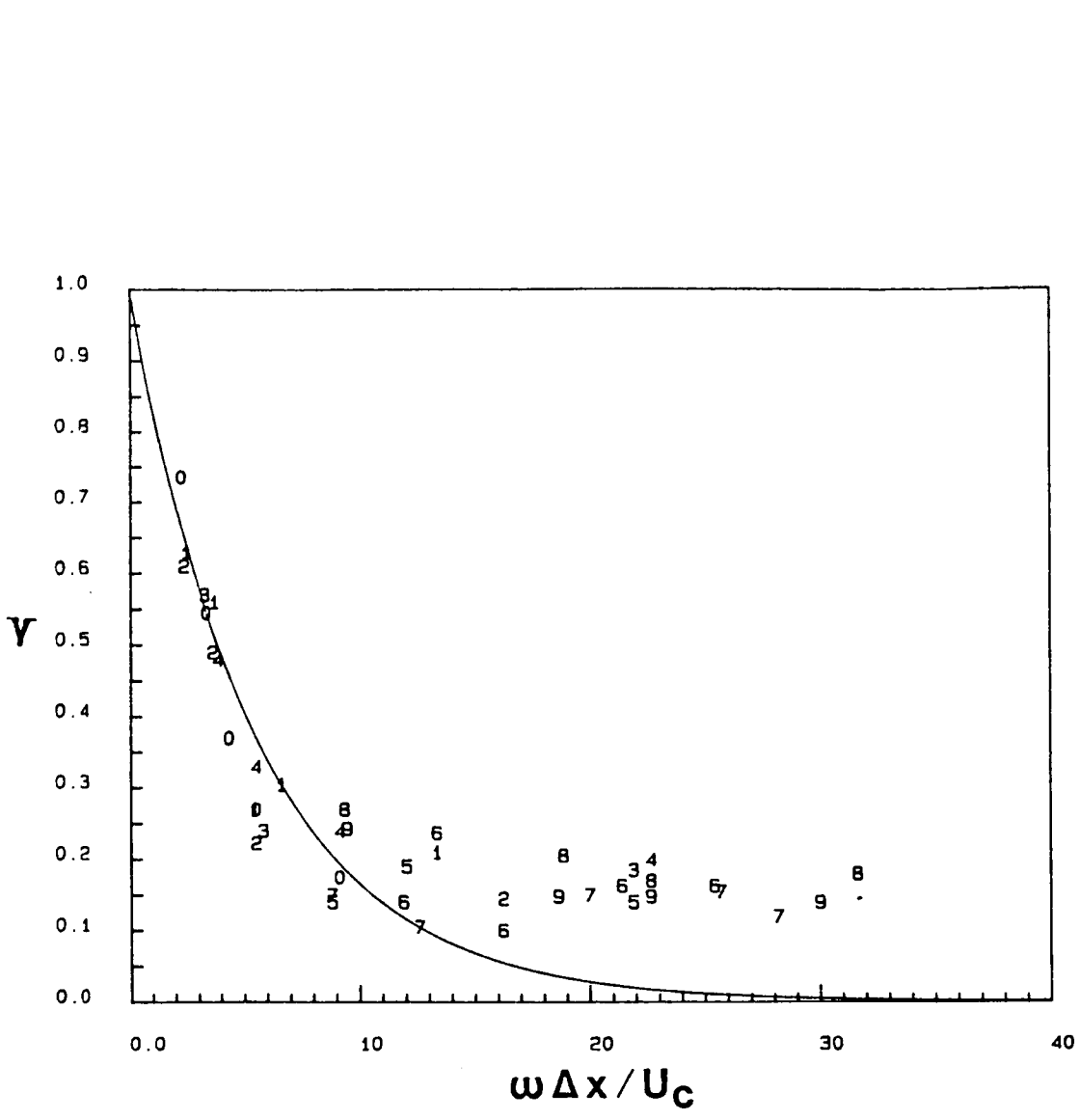

Figure 30. Longitudinal γ for the Favorable Pressure Gradient Flow, x=1.63 m: Solid line is the exponential decay with K_1=0.18.

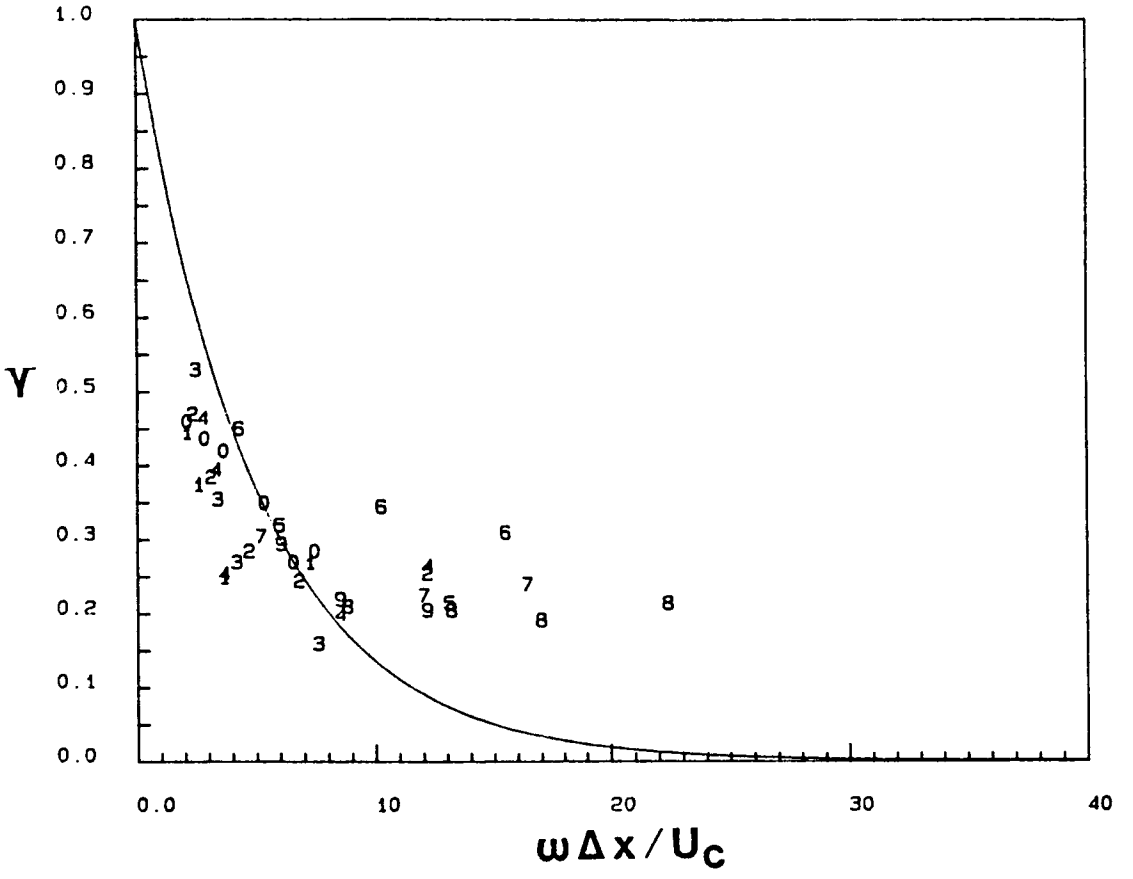

Figure 31. Longitudinal γ for the Favorable Pressure Gradient Flow, x=3.52 m: Solid line is the exponential decay with K_1=0.2.

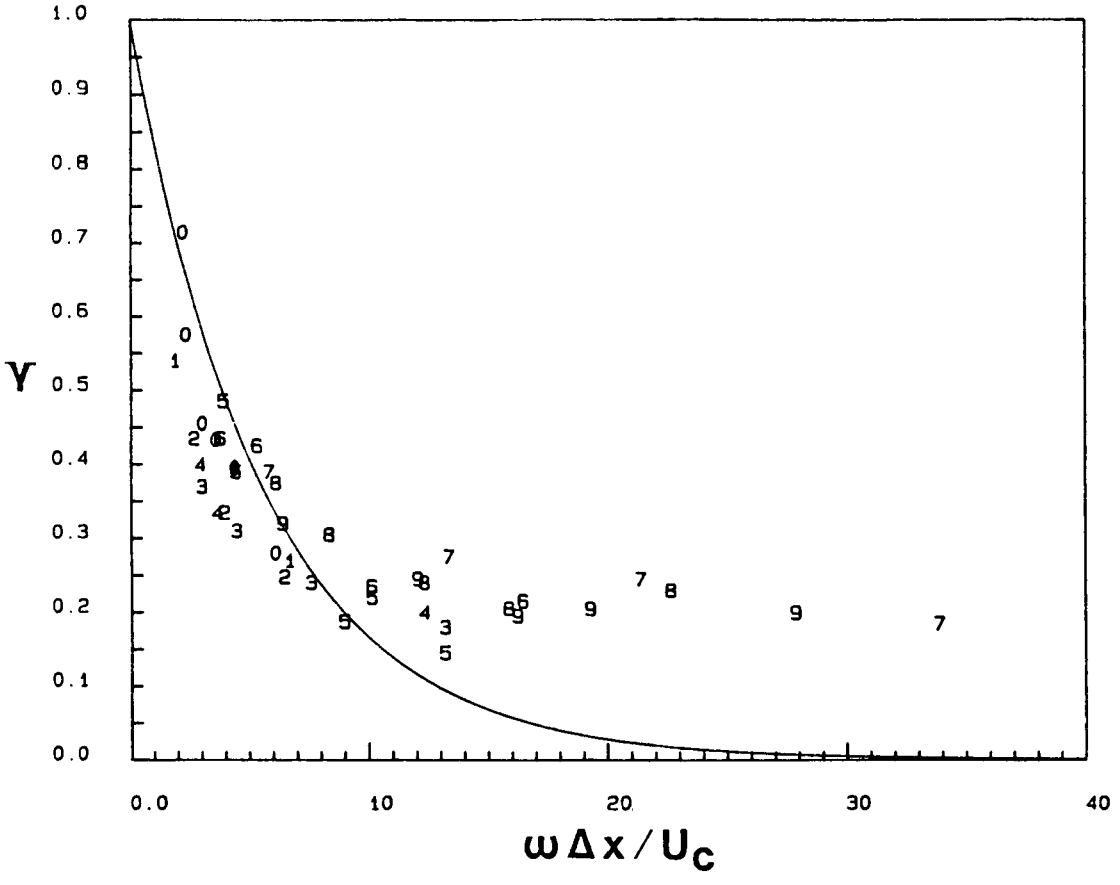

Figure 32. Longitudinal γ for the Favorable Pressure Gradient Flow, x=4.14 m: Solid line is the exponential decay with K_1=0.18.

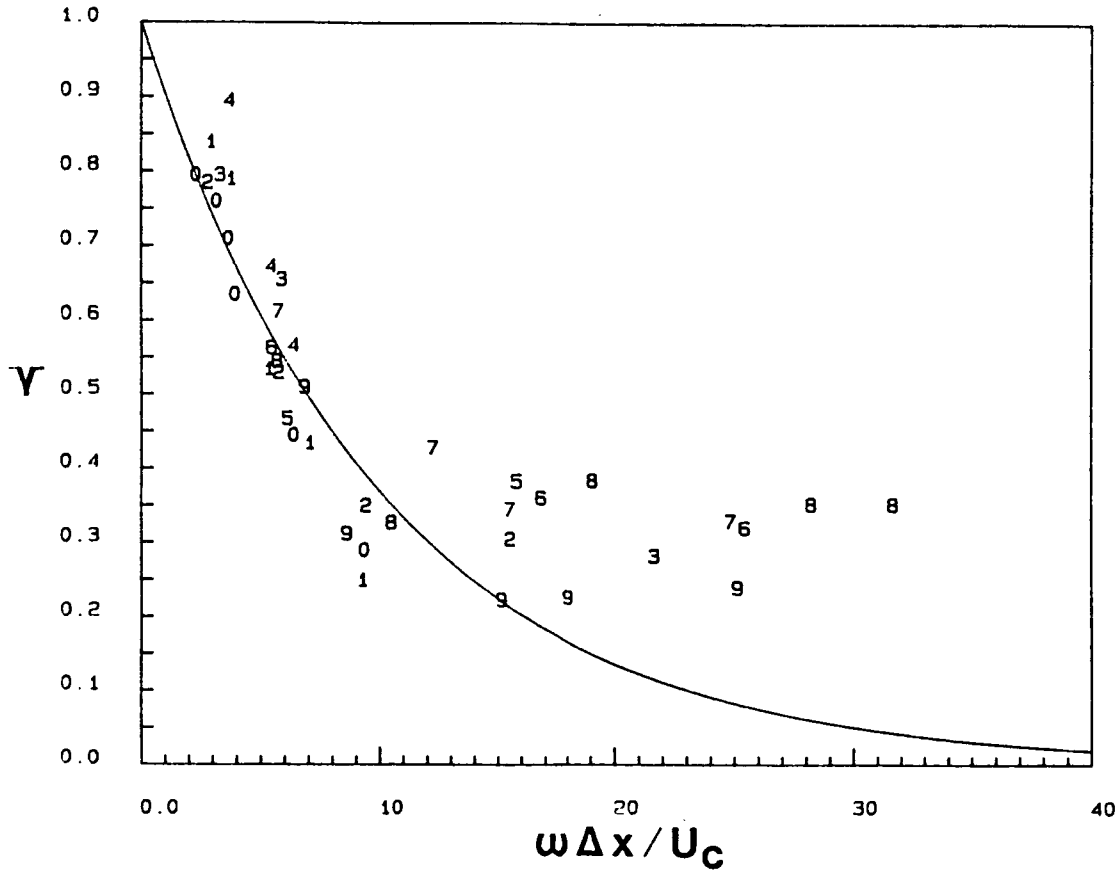

Figure 33. Longitudinal γ for the Favorable Pressure Gradient Flow, x=4.77 m: Solid line is the exponential decay with K_1=0.1.

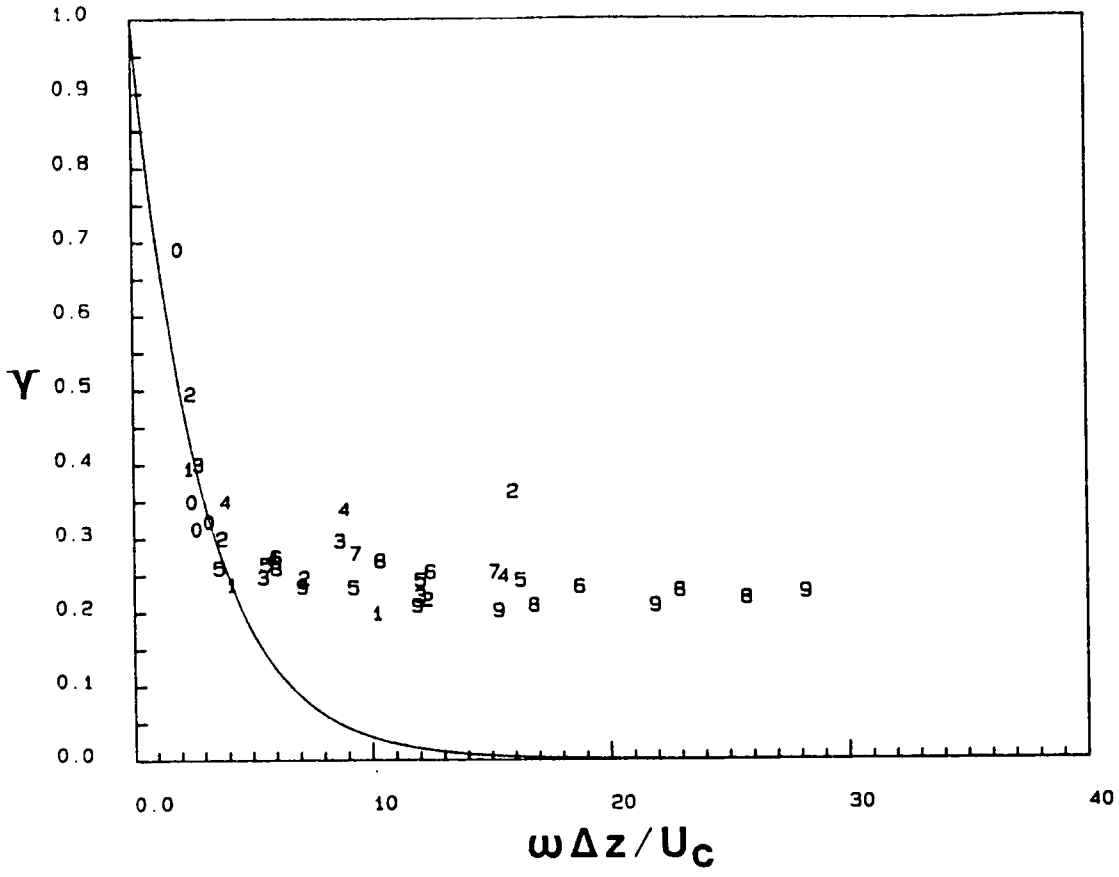

Figure 34. Lateral γ for the Favorable Pressure Gradient Flow, x=1.63 m: Solid line is the exponential decay with K_3=0.35.

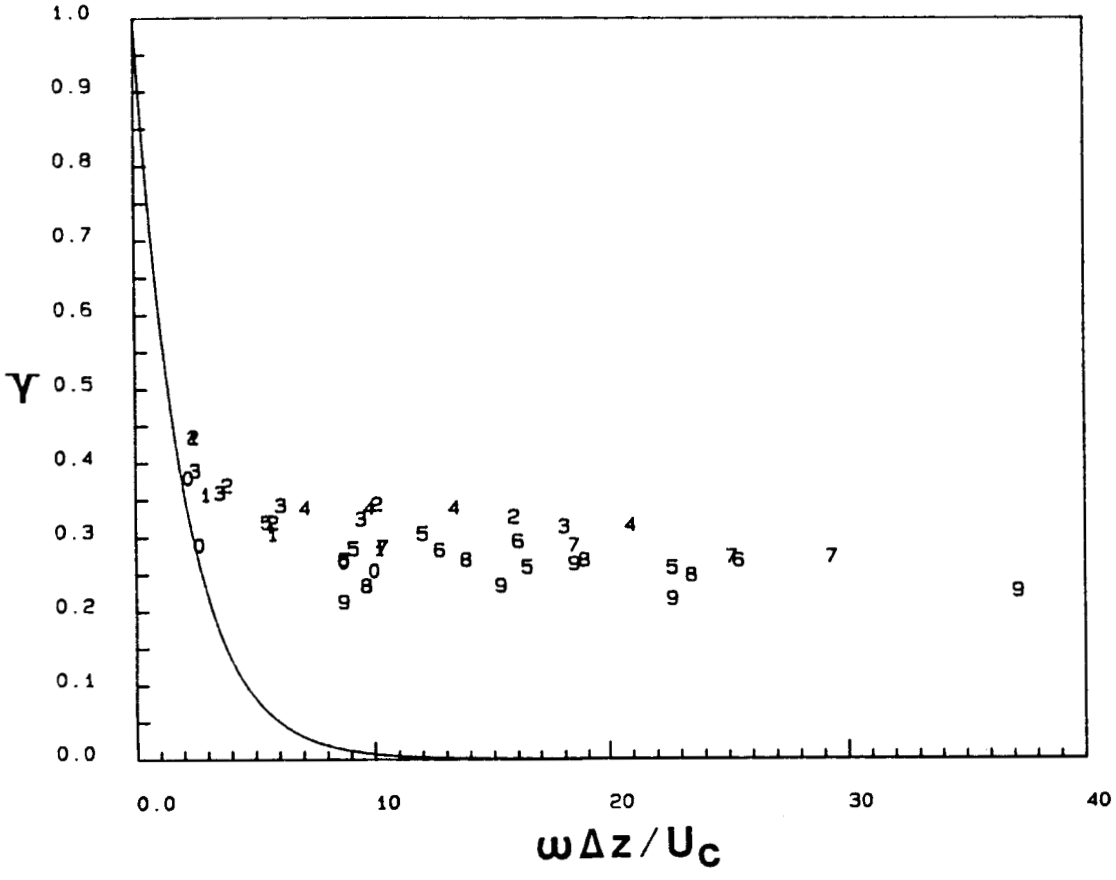

Figure 35. Lateral γ for the Favorable Pressure Gradient Flow, x=3.52 m: Solid line is the exponential decay with K_3=0.5.

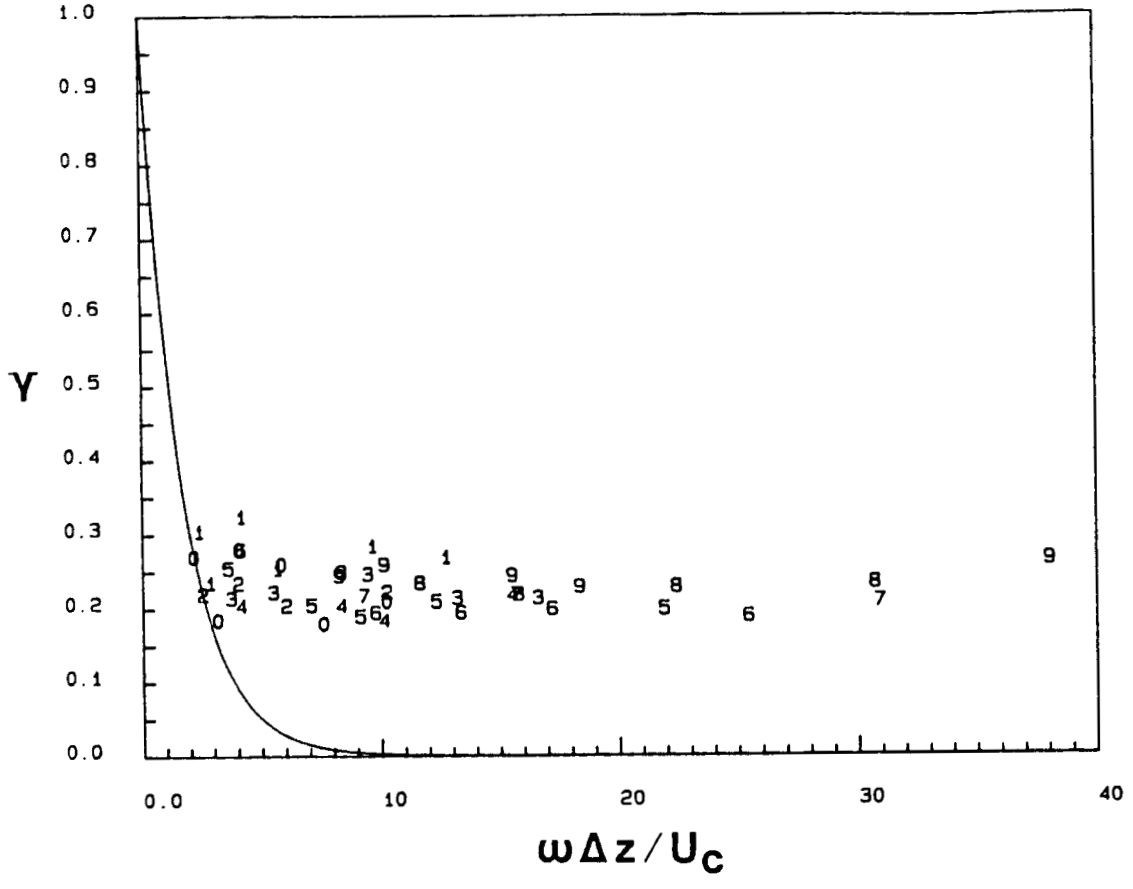

Figure 36. Lateral γ for the Favorable Pressure Gradient Flow, x=4.14 m: Solid line is the exponential decay with K_3=0.6.

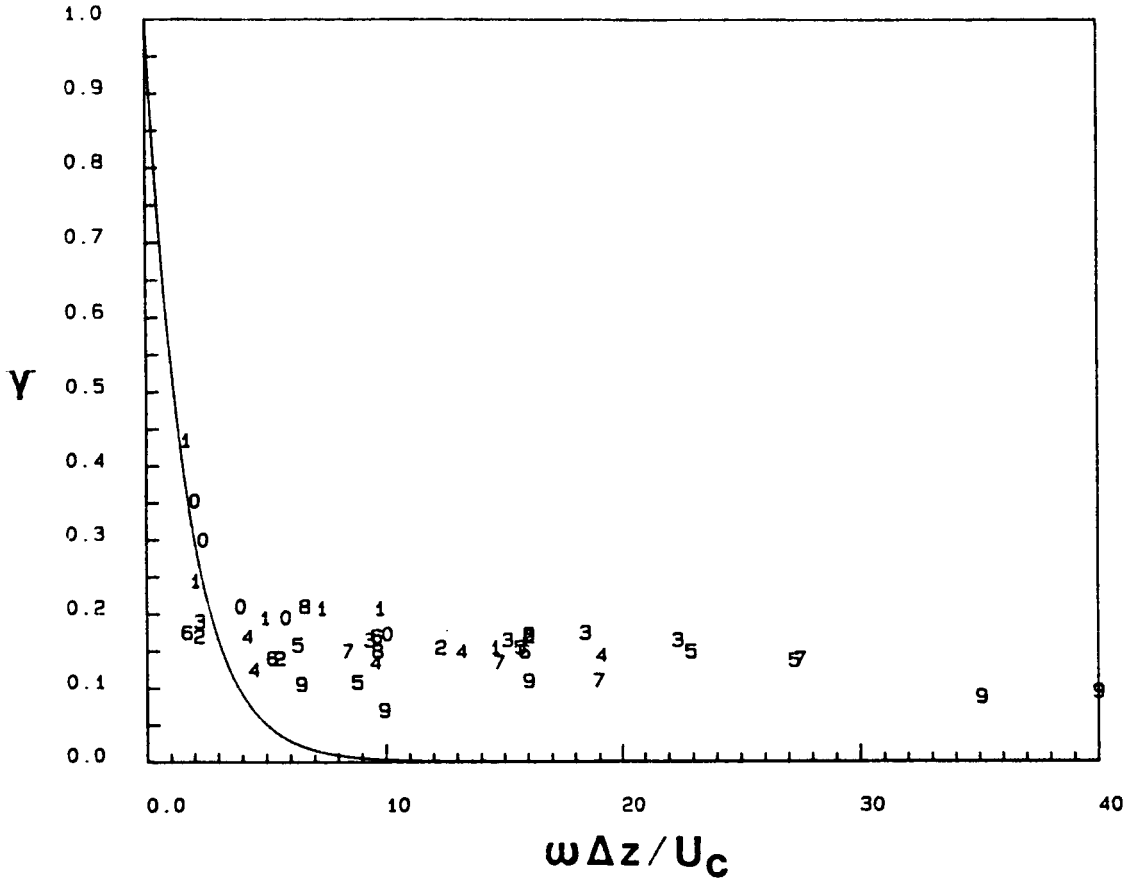

Figure 37. Lateral γ for the Favorable Pressure Gradient Flow, x=4.77 m: Solid line is the exponential decay with K_3=0.6.

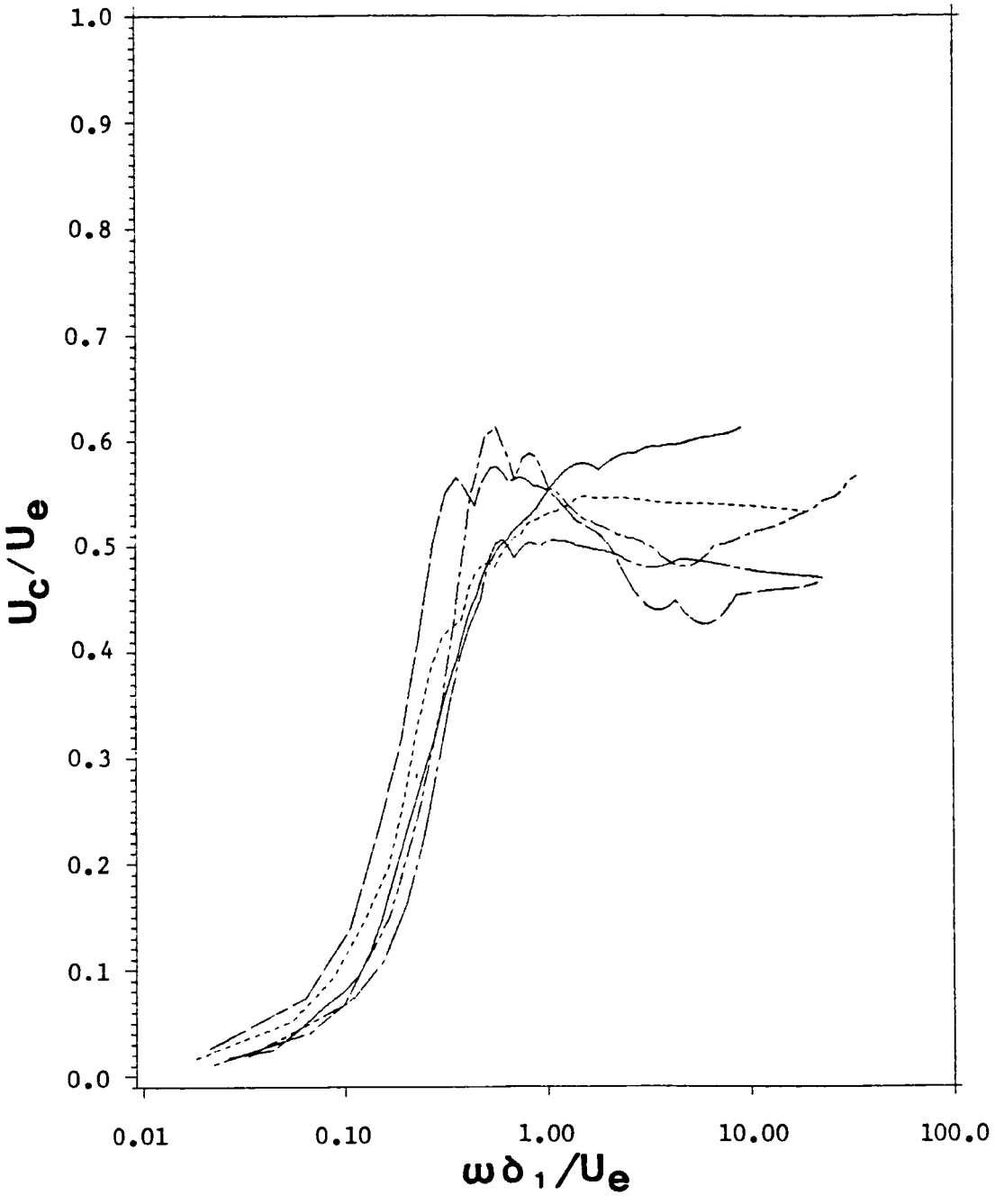

Figure 38. U_c/U_e versus $\omega\delta_1/U_e$ for the Zero Pressure Gradient Flow: ——— 1.63 m; - - - 3.52 m; ——— 4.14 m; - ——— 6.51 m; - ——— 6.51 m ($q=2.4"H_2O$). These are mean curves for all 10 microphone spacings at each x-location.

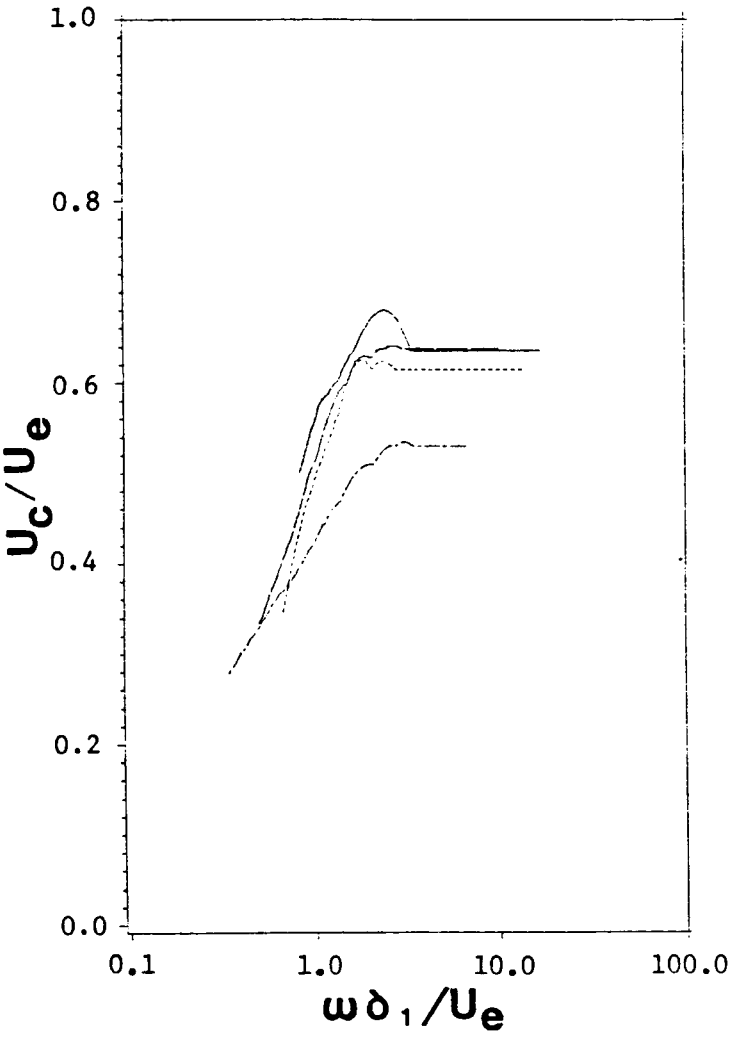

Figure 39. U_c/U_e versus $\omega\delta_1/U_e$ for the Favorable Pressure Gradient Flow: ——— 1.63 m;--- 3.52 m;——4.14 m;-——4.77 m. These are mean curves for all 10 microphone spacings at each x-location.

TABLES

ORIGINAL PAGE IS
OF POOR QUALITY

Authors	U_e m/s	$Re_\theta \times 10^{-3}$	U_τ/U_e	H	d^+	p'/τ_w	$\phi(\omega)^{-1}$ Region	Spectrum level at $\omega\delta_1/U_e = 1.0$ *	K_1	K_3	Comments
BLAKE (1970)	22.25 28.75 37.94 49.98	8.21 10.2 13.2 17.0	0.0383 0.037 0.035 0.033	1.35 1.25 1.25 1.25	43.3 54.1 67.5 83.9	3.6 3.6 3.6 3.6	$1.0<\frac{\omega\delta_1}{U_e}<10$	-51 dB	0.128 0.128 0.128 0.128	0.715 0.715 0.715 0.715	Condenser Microphone With Pinhole
BULL & THOMAS (1976)	24.0 30.6 36.3	4.92 6.283 10.2	0.0352 0.0369 0.0371	1.32 1.3 1.31	45 57 65	2.47 2.46 2.55	$0.09<\frac{\omega\nu}{U_\tau^2}<0.23$	-50.27±3dB	NA NA NA	NA NA NA	Piezo Electric Microphone, Flush Mounted
WILLMARTH & WOOLRIDGE (1962)	NA NA NA	29.0 to 36.0	NA NA NA	NA NA NA	NA NA NA	2.15 to 2.18	No Apparent Region	-51.5 dB	NA NA NA	NA NA NA	Flush Mounted Transducer
PANTON AND LINEBARGER (1973)	NA NA NA	$U_*\delta/\nu \times 10^{-3}$ 1.0 4.0 10.0	NA NA NA	NA NA NA	NA NA NA	2.9 3.02 3.1	$1.445<\frac{\omega\delta_1}{U_e}<2$	-50.96 dB	NA NA NA	NA NA NA	Calculation Method
SCHLOEMER (1966)	24.1 32.0	4.5 5.8	0.0394 0.0387	1.345 1.34	96.06 126.38	1.63 1.63	No Apparent Region	-49.8 dB	0.115 0.115	0.9 0.9	Flush Mounted Piezoelectric
LIM (1971)	41.2	5.4 to 11.54	0.04 to 0.035	1.3	81 to 73.5	2.1 to 2.4	$1<\frac{\omega\delta_1}{U_e}<2.4$	-48.5 dB	NA NA	NA NA	Flush Mounted Piezo Electric

*Spectra nondimensionalized by $10 \log_{10} \left| \frac{\phi(\omega) U_e}{q^2 \delta_1} \right|$

NA denotes not available

Table 1. Results of Previous Studies for a Zero Pressure Gradient Flow.

ORIGINAL PAGE IS
OF POOR QUALITY

Authors	U_e m/s	$Re_\theta \times 10^{-3}$	U_τ/U_e	H	d^+	p'/τ_w	$\Phi(\omega)\varepsilon n^{-1}$ Region	Spectrum level at $\omega\delta_1/U_e=1.0$*	K_1	K_3	Comments
BULL (1967) slight $\frac{dP}{dx}<0$	104 to 173	8.0 to 33.0	0.032 to 0.037	1.4 to 1.31	173 to 246	2.1 to 2.8	$0.4<\omega\delta_1/U_e<1$	-50 dB	0.1 0.1	0.715 0.715	Piezoelectric Membrane (Continuous Surface)
BURTON (1973)	24.38 36.58 49.98	2.15 3.09 3.88	0.0488 0.0516 0.0488	1.3 1.31 1.28	60 102 134	2.15 1.92 2.08	No Apparent Region	-46.98 dB	0.1 0.101	0.416 0.416	Condenser Microphone With Pinhole
DINKELACKER et. al. (1977)	8.5	2.0	0.04	1.314	57	NA	$0.026<\omega\nu/U_\tau^2<0.09$	NA	NA	NA	Optical Device Thin Flexible Membrane
DINKELACKER et. al. (1982)	2.9	0.346	0.0517	NA	500	NA	$0.162<\omega\nu/U_\tau^2<0.569$	NA	NA	NA	Condenser Microphone With Pinhole
EMMERLING (1973)	8.5	2.0	0.04	1.314	47 202	2.9 1.66	No Apparent Region	NA	NA	NA	Optical Device Thin Flexible Membrane
SCHEWE (1982)	6.3	1.4	0.0444	1.394	19	2.48	$0.242<\omega\nu/U_\tau^2<0.969$	NA	NA	NA	Thin Flexible Membrane Type
SCHLOEMER (1966)	40.84 47.85	1.34 1.47	0.0484 0.0474	1.35, 1.37	202 231	1.09 1.09	No Apparent Region	-50.17 dB	0.0916 0.0916	0.925 0.925	Flush Mounted Piezoelectric

*Spectra nondimensionalized by $10 \log_{10}\left|\frac{\Phi(\omega)U_e}{q^2\delta_1}\right|$

NA denotes not available

Table 2. Results of Previous Studies for a Favorable Pressure Gradient Flow.

ORIGINAL PAGE IS
OF POOR QUALITY

X,m	U_e m/s	H	δ_1,mm	$\frac{U_\tau}{U_e}$	$Re_\theta \times 10^{-3}$	d^+ BT-1753	d^+ BT-1755	$\frac{p'}{\tau_w}$ BT-1753	$\frac{p'}{\tau_w}$ BT-1755	K_1	K_3	$\phi(\omega)^\infty_{n-1}$ Region	Spectrum Level at $\omega\delta_1/U_e=1.0$*
1.632	22.36	1.39	3.236	0.0399	3.329	29.04	79.88	3.26	3.07	0.2	0.7	$1.28<\omega\delta_1/U_e<6$*	-50±1.5 dB
1.882	22.36	1.38	3.68	0.0395	3.818	28.78	79.14	3.82	3.17	---	---		
2.226	22.18	1.36	4.288	0.039	4.451	28.21	77.58	3.78	3.07	---	---		
2.546	22.17	1.36	4.854	0.0386	5.069	27.91	76.74	3.44	2.87	---	---		
2.858	22.18	1.35	5.405	0.0382	5.674	27.62	75.98	3.47	2.92	---	---		
3.524	22.34	1.34	6.584	0.0374	7.01	27.26	74.97	3.48	2.68	0.2	0.7		
4.146	22.26	1.34	7.686	0.0368	8.196	26.72	73.49	3.51	2.76	0.3	0.7		
5.48	22.23	1.32	10.04	0.0358	10.76	25.93	71.31	3.68	3.02	---	---		
6.508	21.98	1.32	11.86	0.0352	12.62	25.18	69.24	3.57	2.77	0.3	0.7		
6.508 (α=2.4" H_2O)	32.48	1.32	11.88	0.0336	18.82	35.48	97.58	3.79	3.14	0.3	0.7		

*Spectra nondimensionalized by $10\log_{10}\left|\frac{\phi(\omega)U_e}{q^2\delta_1}\right|$

Comment: Condenser Microphone with Pinhole

Table 3. Results of the Present Study for a Zero Pressure Gradient Flows.

X,m	U_e m/s	H	δ_1,mm	$\frac{U_\tau}{U_e}$	$Re_\theta \times 10^{-3}$	d^+ BT-1753	d^+ BT-1755	$\frac{p'_w}{\tau_w}$ BT-1753	$\frac{p'_w}{\tau_w}$ BT-1755	K_1	K_3	$\frac{\nu}{U_e^2}\frac{dU_e}{dX} \times 10^7$	$\phi(\omega)^a$ n^{-1} Region	Spectrum Level at $\omega\delta_1/U_e=1.0$*
1.632	11.95	1.33	3.196	0.0454	2.447	17.64	48.52	2.618	2.873	0.18	0.35	1.31	$1.0<\omega\delta_1/U_e<3.0$*	-48 dB
1.882	12.43	1.32	3.419	0.0448	2.723	18.13	49.86	2.587	2.83	--	--	1.97		
2.226	13.17	1.32	3.718	0.0441	3.138	18.91	52.0	2.573	2.72	--	--	1.79		
2.546	13.83	1.32	3.818	0.0438	3.384	19.71	54.19	2.574	2.69	--	--	1.84		
2.858	14.52	1.31	3.914	0.0434	3.64	20.54	57.49	2.615	2.7	--	--	1.82		
3.118	15.29	1.31	3.865	0.0433	3.756	21.58	59.34	2.626	2.596	--	--	2.04		
3.524	16.76	1.3	3.643	0.0434	3.912	23.69	65.16	2.611	2.516	0.2	0.5	2.11		
4.146	19.54	1.28	3.141	0.0439	3.932	27.96	76.90	2.768	2.301	0.18	0.6	2.27		
4.772	23.94	1.26	2.639	0.0444	4.045	34.59	95.12	2.939	2.716	0.1	0.6	2.33		

*Spectra nondimensionalized by $10 \log_{10}\left|\frac{\phi(\omega)U_e}{q^2\delta_1}\right|$

Comment: Condenser Microphone with Pinhole

Table 4. Results of the Present Study for a Favorable Pressure Gradient Flow.

SYMBOLS	STREAMWISE AND SPANWISE SPACINGS ΔX, ΔZ (mm)
0	2.413
1	2.741
2	3.134
3	3.772
4	4.086
5	4.587
6	5.112
7	5.730
8	8.354
9	8.834

Table 5. Microphone spacings and symbols for plots of longitudinal and lateral cross spectra for the zero pressure gradient flow.

SYMBOL	STREAMWISE SPACING ΔX (mm)	SPANWISE SPACING ΔZ (mm)
0	2.413	2.413
1	2.999	3.104
2	3.680	3.772
3	4.458	4.544
4	5.108	5.062
5	6.004	5.778
6	6.701	6.701
7	7.404	7.404
8	8.214	8.115
9	9.172	8.788

Table 6. Microphone spacings and symbols for plots of longitudinal and lateral cross spectra for the favorable pressure gradient flow.

Standard Bibliographic Page

1. Report No.	2. Government Accession No.	3. Recipient's Catalog No.
NASA CR-4051		

4. Title and Subtitle	5. Report Date
Some Features of Surface Pressure Fluctuations in Turbulent Boundary Layers With Zero and Favorable Pressure Gradients	MARCH 1987
	6. Performing Organization Code
7. Author(s)	8. Performing Organization Report No.
B.E. McGrath and R.L. Simpson	
9. Performing Organization Name and Address	10. Work Unit No.
Aerospace and Ocean Engineering Department Virginia Polytechnic Institute and State University Blacksburg, VA 24061	11. Contract or Grant No. NAG1-446
12. Sponsoring Agency Name and Address	13. Type of Report and Period Covered
National Aeronautics and Space Administration Washington, DC 20546-5225	Contractor Report
	14. Sponsoring Agency Code 505-61-51-06

15. Supplementary Notes
Langley Technical Monitor: Thomas F. Brooks

16. Abstract

Measurements of surface pressure fluctuation spectra, coherence and convective wave speeds from zero and favorable pressure gradient turbulent boundary layers are reported for momentum Reynolds numbers from 3000 to 18,800. The acceleration parameter, K is near 2×10^{-7} for the favorable pressure gradient flow.

The outer variables, U_e, τ_w and δ_1 non-dimensionalize and collapse the spectra for the low to middle range of frequencies for most test cases. The grouping using the inner variables, U_τ and ν, collapse the spectra for the middle to high range of frequencies for all test cases. The value of p'/τ_w was near 3.8 and 2.8 for the smallest values of d^+ in the zero and favorable pressure gradient flows, respectively.

The coherence exhibits a decay that is not exponential in some cases, but the Corcos similarity parameters $\omega\Delta x/U_c$ and $\omega\Delta z/U_c$ collapse the data for all test cases. The ratio of U_c/U_e increases with $\omega\delta_1/U_e$ up to $\omega\delta_1/U_e$ on the order of unity, where U_c/U_e becomes nearly constant. This was observed in the present results for both streamwise pressure gradient flows.

The experimental results presented show good agreement with previous research.

17. Key Words (Suggested by Authors(s))	18. Distribution Statement
Turbulence Boundary layers Pressure fluctuations Acoustics	Unclassified - Unlimited Subject Category 71

19. Security Classif.(of this report)	20. Security Classif.(of this page)	21. No. of Pages	22. Price
Unclassified	Unclassified	128	A07

For sale by the National Technical Information Service, Springfield, Virginia 22161

NASA-Langley, 1987